Universität Zürich[UZH]

Geographisches Institut

Englacial Debris Concentrations on Zmuttgletscher A Combined Field Study and Modelling Approach Using debrisIGM

GEO 511 Master's Thesis

Author: Leano Mauro Meier, 19-936-939

Supervised by: Prof. Dr. Andreas Vieli, Dr. Evan Miles, Florian Hardmeier

Faculty representative: Prof. Dr. Andreas Vieli

24.04.2026

Englacial Debris Concentrations on Zmuttgletscher

A Combined Field Study and Modelling Approach Using debrisIGM

submitted by

Leano Meier

leanomauro.meier@geo.uzh.ch

19-936-939

Supervisor and Faculty Member:

Prof. Dr. Andreas Vieli

andreas.vieli@geo.uzh.ch

Supervisor:

Florian Hardmeier

florian.hardmeier@geo.uzh.ch

Supervisor:

Dr. Evan Miles

evan.miles@geo.uzh.ch

April 24, 2026

GEO 511 Master's Thesis

Department of Geography, University of Zurich

Acknowledgements

I would like to express my gratitude to all the people who in some way helped to realize this thesis.

I would like to thank my thesis supervisor, Prof. Dr. Andreas Vieli, for giving me the opportunity to work on this project and to be part of an amazing field campaign on Zmuttgletscher. I am thankful for the organization of the campaign, the support during the field work, and the many stimulating and encouraging discussions during the field work and the countless meetings throughout the project. I would also like to thank Florian Hardmeier for introducing me to the debrisIGM module, which he is currently co-developing at UZH, as well as for the support during the second field visit, the many meetings and modelling problems. I would also like to thank thank Dr. Evan Miles for the support and stimulating exchanges during the field work. I would like to thank all the people who were part of the field campaign on Zmuttglestcher: Boris, Diego, Antoine, Julie, Marin, and Armin. I would like to thank Nico, Jan, and Johanna for proofreading. I would like to thank them, as well as my flatmates Nina and Michelle for their support during the stressful final phase of the thesis. Finally, I would like to thank my parents for always supporting me along the way.

Thank you!

Abstract

Debris-covered glaciers represent a growing fraction of Earth's mountain cryosphere, yet the englacial debris concentrations that ultimately govern supraglacial debris cover evolution remain poorly constrained due to the logistical challenges of in-situ measurement. This thesis combines a field campaign on Zmuttgletscher (Valais, Swiss Alps) with numerical modelling using the debrisIGM module, an extension of the Instructed Glacier Model (IGM), to quantify englacial debris concentrations and evaluate the model's ability to reproduce observed spatial patterns.

During the 2025 field campaign, two novel sampling methodologies were applied across fourteen sites in the upper ablation area: Block Sampling (BS, ~ 30 kg ice samples) and Core Sampling (CS, ~ 0.8 kg samples). Measured englacial debris concentrations ranged from 0 to 0.0414 vol.%, placing Zmuttgletscher at the lower end of values reported in the literature and consistent with other temperate Alpine glaciers. Concentrations varied systematically between flow units, covarying with supraglacial debris thickness and ablation rates, confirming that distinct sub-accumulation catchments produce identifiable flow units down-glacier. The BS method proved more robust at low concentrations, while CS enabled broader spatial coverage but suffered from a detection-limit issue at sparse debris concentrations.

The debrisIGM module, forced by a simplified ELA evolution, successfully reproduced the Little Ice Age maximum extent of Zmuttgletscher and, at the reference time steps representing the present-day geometry, produced englacial debris concentrations within the same order of magnitude as the in-situ measurements. Modelled spatial patterns broadly matched the mapped flow units, with elevated concentrations coinciding with substantial debris cover. Tracking particles by source area revealed coherent, clearly distinguishable debris units preserved from headwall to ablation zone, and demonstrated a strong correlation between source-area mean elevation and englacial transport time. These results highlight the value of nummerical modelling for studying debris-covered glacier systems.

Contents

List of Figures

List of Tables

List of Abbreviations

Abbreviations

BS	Block sampling
CS	Core sampling
ELA	Equilibrium Line Altitude
GLAMOS	Glacier Monitoring Switzerland
IGM	Instructed Glacier Model
IPCC	International Panel on Climate Change
LIA	Little Ice Age
m a.s.l.	Meters above sea level
OPTV	Optical televiewer
SBG	Schönbielgletscher
SSP	Shared Socioeconomic Pathway
STG	Stockjigletscher
TMG	Tiefmattengletscher
UZH	University of Zurich

1. Introduction

1.1 Motivation and Relevance

When most people think about a glacier, they probably picture majestically towering masses of ice and snow that gently creep their way down the topography. However, this mighty image of glaciers, characterized by their distinctive blue and white appearances, is likely to change in the near future, as reality often presents itself differently.

In 2025, the UN's 'International Year of Glacier Preservation' and the start of the 'Decade of Action for Cryospheric Sciences (2025–2034)', Switzerland lost 3 % of its glacier volume (Huss et al., 2025a). This decline represents the fourth largest loss in ice volume in a single hydrological year since the beginning of the measurements. Over the past decade, this adds up to a loss of a quarter of Switzerland's ice volume (Huss et al., 2025a). Similar trends can be observed in glaciers around the world (IPCC, 2023; Dussaillant et al., 2025). Their rapid decline is one of the most prominent and visible consequences of the impact of anthropogenic climate change.

Many glaciers are projected to disappear by the end of this century, regardless of which Shared Socioeconomic Pathway (SSP) the world can pursue (Zekollari et al., 2024; Van Tricht et al., 2026). Van Tricht et al. (2026) predict that in glaciated mountain ranges such as the European Alps, where we predominantly find small and rapidly responding glaciers, up to 50 % of all glaciers will vanish in the next two decades.

In addition to this astonishing loss rate of individual glaciers, the appearance of the glaciers that do survive will change. Current warming trends, which cause glacier retreat, have been associated with an increase in the number of debris-covered glaciers, as well as the area and thickness of the debris cover (e.g. Anderson, 2000; Deline, 2005; Kirkbride and Deline, 2013; Rowan et al., 2015; Mölg et al., 2019; Anderson et al., 2021). This extension is mainly linked to the enhanced melt out of englacial debris, a metric that to date has rarely been reported due to labour-intensive and logistically challenging measurement methods (Kirkbride and Deline, 2013; Anderson and Anderson, 2016; Gibson et al., 2017). In addition to these increasing melt out rates (Benn et al., 2012; Kirkbride and Deline, 2013), debris supply due to destabilized lateral moraines and surrounding slopes (Woerkom et al., 2019), as well as permafrost degradation (Gruber et al., 2017) drive the expansion of supraglacial debris. This trend is reflected in the eastern European Alps, where the debris-covered area expanded approximately 11 % (Fleischer et al., 2021). Today, around 20 % of Earth's glaciers ($> 2\,km^2$) exhibit a 'substantial' debris cover ($> 7\,\%$ debris-covered and/or $> 10\,km^2$ of debris) (Herreid and Pellicciotti, 2020), many of which can be found in glaciated (high relief) mountain ranges across the world (Scherler et al., 2018; Herreid and Pellicciotti, 2020).

Supraglacial debris significantly influences the surface energy balance, with its impact being strongly modulated by the thickness of the debris cover (Östrem, 1959; Mattson et al., 1993; Nicholson and Benn, 2006; Evatt et al., 2015). By reducing the surface albedo compared to debris-free glaciers, thin layers enhance surface ablation, while debris covers exceeding the critical thickness of a few centimeters provide thermal insulation to the underlying ice, leading to reduced ablation. Therefore, supraglacial debris has a significant impact on glacier evolution and long-term mass balance (Benn et al., 2012; Scherler et al., 2018; Mölg et al., 2020; Hardmeier et al., 2026).

With millions of people around the world relying on glacial meltwater during the summer and autumn months, a robust understanding of debris-covered glacier sensitivity and response to variable climate becomes vital for accurately predicting future glacier evolution and associated hydrological impacts. Projecting glacier change over the 21st century is a pressing challenge in the context of climate change, with major implications for regional water availability (Huss and Hock, 2018; Zanoni et al., 2023), socioeconomic systems (Rowan et al., 2015; Howe and Boyer, 2024; Howe and Boyer, 2025; Huss et al., 2025b), global sea-level rise (Zemp et al., 2020; Edwards et al., 2021; Slangen et al., 2023), and paraglacial hazards, such as glacial lake outburst flood hazards (Compagno et al., 2022b; Racoviteanu et al., 2022).

Given the scarcity of long-term observational data, numerical modelling becomes an essential methodological tool to reliably project the evolution of debris-covered glaciers. To achieve this, numerical flow models capable of tracking both englacial and supraglacial debris transport are needed (Ferguson and Vieli, 2021). In recent decades, many such models have emerged that simulate ice flow, debris supply and transport, debris cover evolution, and its effect on surface mass balance and hence glacier evolution with varying focus (e.g. Egholm et al., 2011; Anderson and Anderson, 2016; Jouvet et al., 2022). Constraining and verifying such models requires robust data of key input metrics such as englacial debris concentrations. However, data on the concentration of englacial debris remain exceptionally sparse due to the considerable logistical and methodological challenges of their acquisition (Miles et al., 2021).

1.2 Scope and Research Questions

The aim of this thesis is to get a better understanding of the magnitude and spatial distribution of the englacial debris concentration on Zmuttglacier, a debris rich glacier in the Swiss Alps. To achieve this, the study focuses on the integration of in-situ measurements collected on Zmuttgletscher, to validate the results of a numerical modelling approach using the Integrated Glacier Model (IGM) (Jouvet et al., 2022; Jouvet et al., 2024). Further, it aims to provide a methodological approach for future in-situ measurement campaigns of englacial debris concentrations on debris-covered glaciers.

> **Research Question 1 – Englacial Debris Concentration:** What are the englacial debris concentrations across the upper ablation zone of a debris-covered glacier, and how do these concentrations differ between flow units?

Motivated by the lack of data and research on englacial debris concentrations (Miles et al., 2021), this study aims to provide additional data on englacial debris concentration collected on Zmuttgletscher. This data is then used to verify the modelling approaches conducted in this thesis.

> **Research question 2 - Methodological approach:** What are the strengths, limitations, and uncertainties of the applied field measurement methodology and the incorporation of its results as a validation for numerical modelling of debris-covered glaciers?

With studies on debris-covered glacier still being limited by a lack of data on englacial debris concentrations (Miles et al., 2021), a key factor in the evolution of debris-covered glaciers (Kirkbride and Deline, 2013; Anderson and Anderson, 2016; Gibson et al., 2017), this study aims to explore new measurement methods and give an overview of their capabilities.

> **Research question 3 - Modelling a Debris-Covered Glacier:** To what extent does the Instructed Glacier Model (IGM) capture the spatial variability of the englacial debris concentration and debris cover patterns in comparison to real-world observations?

This thesis also aims to explore the capabilities of IGM for modelling debris-covered glaciers (Jouvet et al., 2022; Jouvet et al., 2024), that uses Lagrangian particle tracking in a new approach to model englacial debris (Hardmeier et al., 2025). After Defining seeding areas, flow units and climate forcing, IGM is used to study spatial patterns in the debris evolution on Zmuttgletscher.

1.3 Thesis Structure

This thesis is structured into six chapters. The first chapter introduces the broader scientific context, the challenges and the gaps that motivate this work, and presents the research questions. After that, the theoretical background provides insights into the processes that govern debris-covered glacier systems. This chapter also introduces the study site, Zmuttgletscher and its regional context. In the methods chapter, the field work, mapping and modelling techniques are presented in detail. The results chapter presents the findings of this study. The fifth chapter, discussion, integrates the field and modelling results, comparing measured and modelled values, and evaluates the performance and limitations of both the field and modelling methodologies. The final chapter, concludes the thesis by answering the research questions and offering perspectives for future research.

2. Background

2.1 Debris-covered Glaciers

Debris-covered glaciers are commonly defined as glaciers that exhibit a continuous supraglacial debris layer that spans the full width of the ablation area over some portion of its extent (Kirkbride, 2011). The supraglacial debris cover fundamentally alters the surface mass balance (Östrem, 1959; Mattson et al., 1993; Nicholson and Benn, 2006; Evatt et al., 2015), significantly influencing glacier response to climate forcing compared to clean-ice glaciers (Benn et al., 2012; Scherler et al., 2018; Mölg et al., 2020; Hardmeier et al., 2026). This supraglacial debris cover is the result of complex interactions between debris supply, debris transport mechanisms, ice flow and ablation processes (Kirkbride and Deline, 2013). Figure 2.1 shows a schematic view of a debris-covered glacier system.

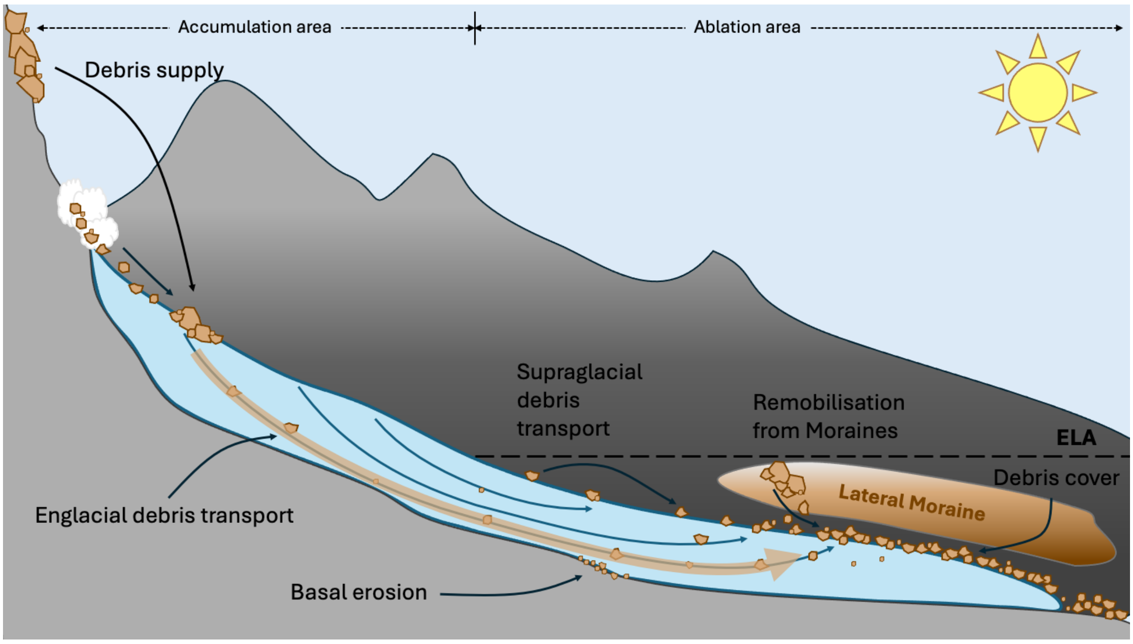

Figure 2.1: Schematic view of the main processes governing the debris-covered glacier dynamic (inspired by Ferguson, 2022). ELA stands for Equilibrium Line Altitude.

2.1.1 Debris Supply

The debris supplied to the glacier system originates from three main sources: basal erosion, gravitational mass-wasting processes from the surrounding rock walls, or remobilization of debris from moraines (Woerkom et al., 2019). As a result, the debris is heterogeneous in nature, encompassing a broad spectrum of particle sizes, from fine-grained sand and small pebbles to large boulders. In glaciers situated in high-relief mountain ranges, subglacial abrasion is generally considered to have a very limited contribution to the total debris supply. This is because the basal debris supply rates are orders of magnitude lower than those of gravitational processes, and the resulting debris remains largely close to the glacier bed (Benn and Owen, 2002; Hambrey et al., 2008; Woerkom et al., 2019). Therefore, debris is mainly deposited onto the glacier through gravitational processes, such as rockfall and avalanches from surrounding head walls, influenced by local conditions such as topography, geological conditions, and climate (Benn and Owen, 2002; Hambrey et al., 2008; Scherler et al., 2011). Consequently, there are spatial differences in the distribution of the debris input, depending on the characteristics of the local source areas.

Accurately quantifying the debris input rates based on these processes poses significant challenges. Due to the irregular nature of these events and poor accessibility, measurements of the debris input volume are scarce (Heimsath and McGlynn, 2008; Scherler and Egholm, 2020). Thus, debris supply rates are often estimates based on assumed head wall erosion rates or rely on simplified debris flux assumptions on the glacier tongue (Heimsath and McGlynn, 2008; Banerjee and Wani, 2018; McCarthy et al., 2022).

2.1.2 Debris Transport Path and Distribution

Once deposited onto the glacier, debris is transported down-glacier to the glacier margins, driven by the ice flow dynamics. Debris deposited in the ablation area is transported supraglacially, whereas debris deposited in the accumulation area is entrained into the ice, where it is transported englacially following the ice flow trajectory (Kirkbride and Deline, 2013). As the glacier experiences a negative surface mass balance in the ablation area, the melting of the surrounding ice eventually exposes the entrained material at the surface. This emergence of englacial debris is a critical contributor to the development of extensive supraglacial debris covers (Kirkbride and Deline, 2013; Anderson and Anderson, 2016; Anderson and Anderson, 2018; Gibson et al., 2017).

Glacier flow is not uniform across the glacier width, but organised into discrete flow units that originate from individual sub-accumulation basins (Hambrey et al., 2008; Kirkbride and Deline, 2013; Jennings et al., 2014). The unique characteristics of each basin are reflected in its corresponding flow unit. As a result, debris is not distributed evenly across the glacier surface but instead exhibits spatial patterns that broadly reflect the structure of the underlying flow units (Kirkbride and Deline, 2013; Jennings et al., 2014; Mölg et al., 2020).

The resulting supraglacial debris cover is the product of both the emergence of englacial debris and the redistribution of existing surface debris, typically increasing in thickness towards the terminus (Anderson and Anderson, 2018; Mölg et al., 2019). However, due to the complex interplay of local catchment characteristics and glacier dynamics, understanding, measuring, and quantifying these englacial debris emergence patterns is difficult (Kirkbride and Deline, 2013; Scherler and Egholm, 2020).

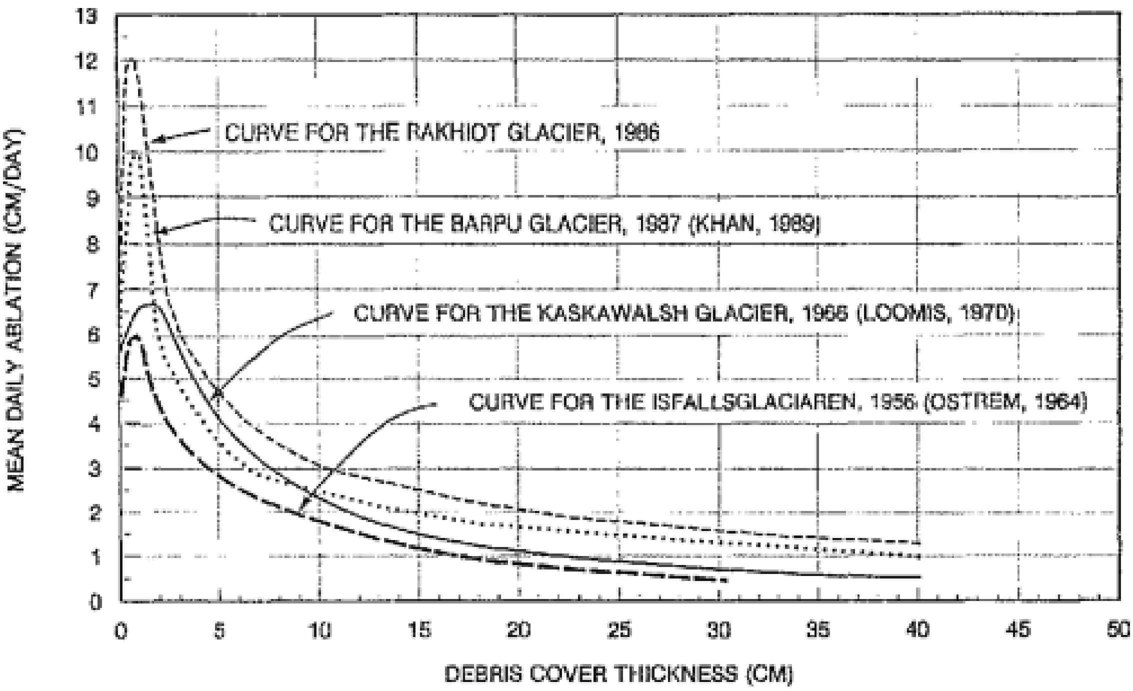

Figure 2.2: Empirically measured Østrem curves showing the relationship between supraglacial debris thickness and daily ablation on selected glaciers (Mattson et al., 1993). Thin debris covers (up to $\sim 3\,\mathrm{cm}$) enhance the mean daily ablation, while thicker covers lead to a reduction in mean daily ablation.

2.1.3 Effects of Supraglacial Debris

Östrem (1959) and many more (e.g. Mattson et al., 1993; Nicholson and Benn, 2006; Evatt et al., 2015) have shown that the presence of supraglacial debris significantly alters the surface mass balance of a glacier. Thick debris cover reduces the surface ablation compared to debris-free clean-ice glaciers, due to insulation effects, while thin or discontinuous debris layers enhance the surface ablation (Figure 2.2). These insulation effects potentially allow a debris-covered glacier to advance beyond the extent reached by a clean-ice glacier under the same climatic conditions (Anderson and Anderson, 2018).

In contrast, studies have shown that debris-covered glaciers can also exhibit thinning and mass loss rates comparable to those of clean-ice glaciers, which can be explained by the effects of dynamic stagnation and cryokarst features such as ice cliffs and supraglacial ponds (Pellicciotti et al., 2015; Kneib et al., 2023; Anderson et al., 2021). In contrast to debris-free glaciers, debris-covered glacier tongues tend to lose mass through thinning rather than retreat (Pellicciotti et al., 2015; Rowan et al., 2015; Mölg et al., 2019).

2.2 Englacial Debris Concentrations

The link between the expansion of supraglacial debris cover and enhanced melt out of englacial debris, due to rising temperatures is well documented (e.g. Kirkbride and Deline, 2013; Anderson and Anderson, 2016; Gibson et al., 2017). Despite this, few studies have reported comprehensive englacial debris concentrations (Gibson et al., 2017; Miles et al., 2021) due to logistical challenges, high operational costs, and labor intensive methods for data acquisition (Kirkbride and Deline, 2013; Gibson et al., 2017; Miles et al., 2021).

In general, previously measured englacial debris concentrations are low but span several orders of magnitude, reflecting glaciological variability, differences in measurement methodology, and spatial context. Across the studies summarized in Table 2.1, concentrations range from 0.00034 vol.% at ice cliffs of Watts Outlet Glacier (Dowdeswell, 1986) up to 11.708 vol.% within debris bands near terminus at Glacier d'Estelette (Kirkbride and Deline, 2013). The values retrieved from Djankuat Glacier (0.0406 vol.%; Bozhinskiy et al., 1986), a partially debris-covered temperate valley glacier in the North Caucasus, fall within the lower end of the range.

Substantial spatial variabilities can be observed within individual glaciers. At Khumbu Glacier, the concentrations derived from OPTV in the mid-to upper ablation area remain modest (0.1–0.7 vol.%), whereas the single near-terminus borehole returned a significantly higher value of 6.4 vol.% (Miles et al., 2021). Similar spatial variabilities can be observed at Glacier d'Estelette, where measurements within debris bands yield concentrations several orders of magnitude higher than the surrounding dispersed ice facies (0.113–11.078 vol.% versus 0.003–0.005 vol.%; Kirkbride and Deline, 2013).

These observations suggest that away from structural features, such as debris bands, englacial debris concentrations are generally found to be low. Overall, they indicate that englacial debris concentration is not a single characteristic value for a given glacier, but rather a highly variable quantity governed by the history of debris entrainment and transport through the ice.

Table 2.1: Englacial debris concentration measurements on debris-covered glaciers

Glacier	Location / Region	Concentration [vol.%]	Measurement Method	Spatial Context	Reference
Khumbu Glacier	Nepal, Himalaya	0.1 – 0.7	Borehole optical televiewer (OPTV) logging; three boreholes up to 150 m deep, drilled by hot-water drill; continuous depth profile of debris clasts imaged on borehole wall	Mid- to upper ablation area	Miles et al. (2021)
Khumbu Glacier	Nepal, Himalaya	6.4	Borehole optical televiewer (OPTV) logging; one borehole 30 m deep, drilled by hot-water drill; continuous depth profile of debris clasts imaged on borehole wall	Near-terminus	Miles et al. (2021)
Glacier d'Estelette	European Alps, Italy	0.113 – 11.078	Melt out experiment; englacial debris concentration determined by weighing debris that emerged from cleared ice surface compared to ice ablation; assuming debris density of 2700 kg/m^3	Within debris bands, near-terminus	Kirkbride and Deline (2013)
Glacier d'Estelette	European Alps, Italy	0.003 – 0.005	Melt out experiment; englacial debris concentration determined by weighing debris that emerged from cleared ice surface compared to ice ablation; assuming debris density of 2700 kg/m^3	Clean ice (dispersed facies, near-terminus	Kirkbride and Deline (2013)
Djankuat Glacier	Caucasus, Russia	0.0406	Melt-out calculation; Debris volume of a previously debris-free surface was combined with total surface ablation over 14 year time period	Lower ablation area	Bozhinskiy et al. (1986)
Watts Outlet Glacier	Baffin Island, Canada	0.00034 – 0.329	Ice cliff surface sampling; debris concentration determined by volume fraction of debris particles from melted ice samples	Terminal ice cliffs, clean ice surface	Dowdeswell (1986)

2.3 Modelling

The lack of long-term glacial measurements restricts the analysis of glacier systems to relatively narrow temporal intervals. Using numerical modelling, this small window can be enlarged to better understand past and present glacier dynamics. But especially when predicting the future evolution of glaciers, numerical modelling becomes essential (e.g. Anderson and Anderson, 2016; Zekollari et al., 2019; Ferguson and Vieli, 2021). This is why, at the end of the last millennia, the first glacier models started to emerge. Based on Glen's flow law (Glen, 1955), treating ice as a non-Newtonian fluid, these models solved Stokes equations (e.g. Gudmundsson, 1999).

Although many glacier models have been designed for clean-ice glaciers and are therefore not suitable for debris-covered systems (Rowan et al., 2015), recent years have seen significant advances in the modelling of debris-covered glaciers. Progress has been driven by the scarcity of (en)glacial debris data, improved knowledge of the debris-covered glacier system, the availability of high-resolution satellite images, and computational capacity. Building on this, many different modelling approaches have been used to study the effects of debris on glacier behavior, varying in complexity depending on the research question (e.g. Anderson and Anderson, 2018; Ferguson and Vieli, 2021; Compagno et al., 2022a). Hardmeier et al. (2026) distinguish between three different debris modelling approaches:

The first category prescribes debris thickness patterns directly, without representing debris transport processes. Fixed or simplified spatio-temporal debris distributions are imposed in the ablation area to modulate the surface mass balance, allowing the effects of debris cover on glacier extent, stagnation, and thinning to be studied in isolation (Banerjee and Shankar, 2013; Compagno et al., 2022a).

A second category couples supraglacial debris flux and surface velocity with debris-cover effects on ablation. In simpler variants, debris is deposited directly on the glacier surface in the ablation area (Verhaegen et al., 2020). More elaborate variants include debris originating in the accumulation area, assuming uniform englacial debris concentrations that contribute to the supraglacial cover through melt-out processes (Ferguson and Vieli, 2021). Because these models do not resolve englacial transport explicitly, they do not reproduce transport delays or debris-band thickening and thinning due to ice flow, but rather respond instantaneously and uniformly to prescribed concentration changes. This category has mainly been applied to idealized glacier geometries to explore simple climate change scenarios, delayed length response, thinning patterns, and the influence of debris-free ice cliffs or other features (e.g. Ferguson and Vieli, 2021; Mayer and Licciulli, 2021).

A third category explicitly represents englacial debris transport through the ice. Two sub-approaches are used within this category. Eulerian schemes advect debris concentrations on a fixed grid (Rowan et al., 2015; Wirbel et al., 2018; Ferguson, 2022). In their benchmark study, Anderson and Anderson (2016) applied this approach to explore the influence of debris input location and rates on glacier extent, as well as patterns of glacial thinning (Anderson et al., 2021). Their model integrates a debris-coupled mass balance and debris input areas with a complete englacial and supraglacial advection framework. Lagrangian schemes, by contrast, track debris as discrete particles, as implemented in iSOSIA (Egholm et al., 2011) and IGM (Jouvet et al., 2022; Jouvet et al., 2024), and are particularly suited to studying the three-dimensional particle pathways (Egholm et al., 2011; Bernard et al., 2020; Scherler and Egholm, 2020; Margirier et al., 2025).

This study uses a Lagrangian particle-tracking approach , which is well-suited to the research questions addressed here: reconstructing debris origin, tracking transport pathways from source to surface, and quantifying englacial transport times by source area.

2.4 Study Area

This study focuses on the Zmuttgletscher ($45°59'N$, $7°37'E$), a debris-covered glacier in the Western Alps (Figure 2.3). The valley glacier is located at the end of the Matter Valley in the Canton of Valais (CH), close to Zermatt. It is surrounded by some of the most prominent peaks of the Alps, such as the Matterhorn (4478 m a.s.l.), Dent Blanche (4358 m a.s.l.) and Dent d'Hérens (4173 m a.s.l.) and high ridges ($>$ 3400 m a.s.l.) that connect them. Over a length of $\sim$ 5.93 km (2023) the glacier itself ranges from $\sim$ 2240 m a.s.l. at the glacier tongue, all the way up to $\sim$ 4150 m a.s.l., the highest parts of the accumulation area (Bauder et al., 2024). In 2016, the Zmuttgletscher, together with its tributaries, covered a total surface area of 15.74 km^2, with debris covering large parts of the ablation area (Mölg et al., 2019). This debris originates in steep head walls, such as the Dent d'Hérens north face ($>$ 1000 m) or the Matterhorn west face ($\sim$ 1500 m), surrounding the accumulation area (Mölg et al., 2019).

During the Little Ice Age (LIA, $\sim 1300-1850$), there were three important tributaries that fed the main tongue of the Zmuttgletscher. Today, Tiefmattengletscher (TMG) is the primary contributor, while the Stockjigletscher (STG) plays a lesser role. As a result of its ongoing retreat, the third tributary, Schönbielgletscher (SBG), is close to detaching from the main tongue of the Zmuttgletscher.

The biggest tributary is the Tiefmattengletscher in the south, where the Study site is located (Figure 2.3). Its accumulation areas are surrounded by steep head walls such as the Dent d'Hérens north face (> 1000 m) or the Matterhorn west face (∼ 1500 m). Avalanching and rockfall of these faces cause high debris input rates, which are reflected in the continuous debris cover extending up to the former accumulation area close to the foot of the rock walls.

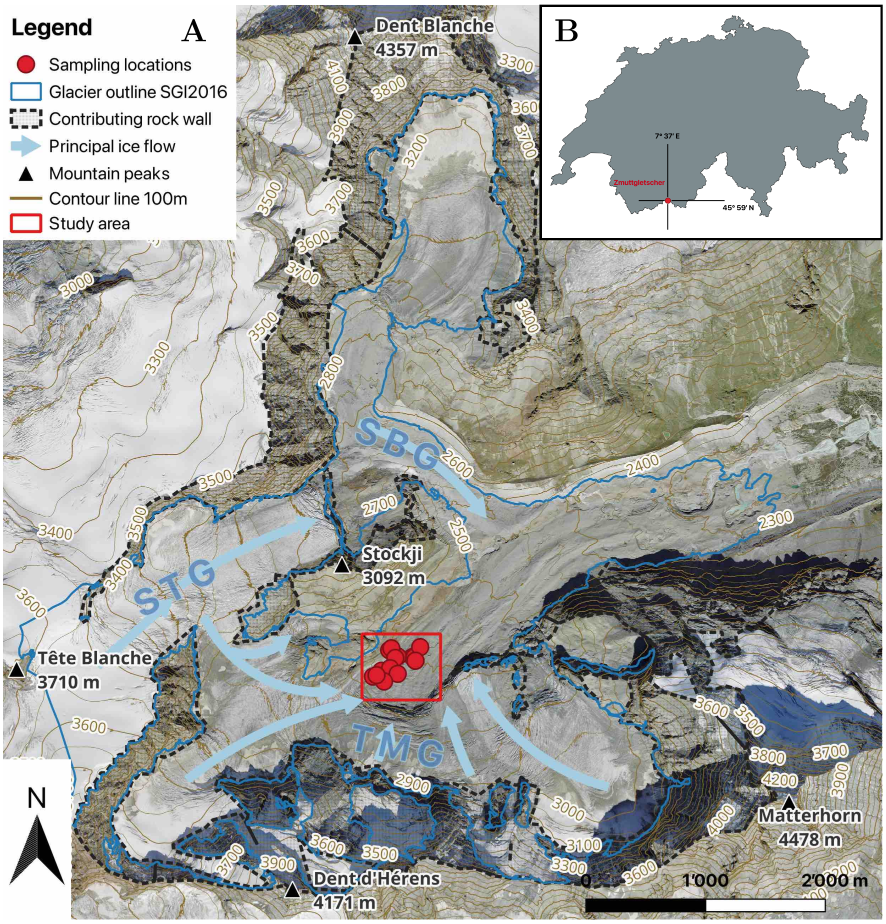

Figure 2.3: (A) Overview of the Zmuttgletscher (VS). The map illustrates the glacier extent (blue) according to the Swiss Glacier Inventory 2016 (SGI2016; Linsbauer et al., 2021) highlighting the principal ice flow trajectories (light blue arrows) of the three main tributaries: Schönbielgletscher (SBG), Stockjigletscher (STG), Tiefmattengletscher (TMG). The study site of the 2025 fieldwork campaign in the upper ablation area (red rectangle) encapsulates all the englacial debris concentration sampling locations (red dots). Contributing rock walls are delineated by dashed black lines. Background image is an orthophoto from 2023 (Swisstopo, 2023). (B) Map of the geographical location.

Stockjigletscher is a tributary feeding the Zmuttgletscher from the west (Figure 2.3). Here, the accumulation area reaches all the way to the ridges around Tête Blanche (3710 m a.s.l.). Due to the lack of prominent rock walls and thus only minimal debris supply, the Stockjigletscher does not transport significant amounts of debris to the ablation area. Its main branch connects to the Schönbielgletscher just north of Stockji (3092 m a.s.l.). The second branch connects to the Tiefmattengletscher via an icefall. There, the branch splits into two. The smaller of those branches (just south of Stockji) detached from the main Zmuttgletscher tongue around 2010.

Originating at ∼ 3400 m a.s.l. just below the south face of Dent Blanche, Schönbielgletscher is a tributary that feeds the Zmuttgletscher from the north (Figure 2.3). It receives its accumulation primarily through avalanching from the surrounding rock walls, which extend all the way up to Dent Blanche. This results in a high debris input, covering most of the relatively low-lying glacier by a continuous debris cover.

Since the end of the LIA, in the mid 19th century, Zmuttgletscher experienced predominantly negative mass balances that caused substantial glacier thinning and a retreat of ∼ 1.9 km in length (Mölg et al., 2019). During the same time, the debris cover changed significantly, increasing by 19 % to 32 % without evidence of large rockfalls (Mölg et al., 2019). Mölg et al. (2019) suggest that this strong increase can be explained by the combined effects of climatic changes (temperature increases), decreasing ice flow velocities, and short response time (due to the comparatively small glacier size) together with a large debris-free ablation area at the end of the LIA (up to the year ∼ 1990).

3. Methods

3.1 Field work on Zmuttgletscher

During the summer of 2025, a field work campaign was conducted on Zmuttgletscher (Figure 2.3) to gather new data to support this study. Over the course of two visits, measurements were collected regarding englacial debris concentration, debris thickness, ablation rates, and other glaciological metrics.

An initial three-day visit in early July (8–10 July) focused on the measurement of englacial debris concentrations and debris cover thickness. Additionally, several monitoring stations were established, including a weather station, ablation stakes and a melt-out experiment site equipped with a wildlife camera. During a follow-up visit 28-days later (6 August), the ablation stakes were remeasured, a second set of debris cover thickness measurements was obtained and both the weather station and the wildlife camera were retrieved.

The study site was located in the upper ablation area of the Zmuttgletscher at an elevation of ~ 2600 m a.s.l., an area that is predominantly fed by the Tiefmattengletscher tributary (Figure 2.3). The presence of supraglacial debris across most of the area, in contrast to the debris-free surfaces found further up-glacier, suggested that active melt-out of englacial debris was occurring in this area. Additionally, the area exhibited significant spatial variability in both supraglacial debris coverage and glacier surface elevation, consistent with the expected influence of distinct underlying flow units, as described in Section 3.2.1. Constrained by spatial restrictions imposed by local hazards (e.g. rockfall, icefall or crevasses), proximity to camp, and limited perspective available from the glacier surface, three distinct flow units were defined in-situ, each exhibiting distinctive debris covers. Consequently, the flow unit boundaries defined in the field were less precise and did not completely match those derived from the remote sensing analysis in Section 3.2.1.

The primary purpose of this field work campaign was to address the lack of data regarding the concentration and distribution of englacial debris, as stated in Section 2.2, as well as to investigate the relationship between supraglacial debris cover and englacial debris concentrations. Such in-situ observations are indispensable for validating numerical modelling approaches, like the one employed in this research. Therefore, the main focus was on the quantification of the englacial debris concentrations (Section 3.1.1).

A secondary objective of the campaign was the evaluation of two distinct measurement methodologies to assess their comparative viability for future research. In addition, debris cover thickness measurements were obtained to capture the spatial variability between individual flow units (Section 3.1.2), providing additional validation data for the numerical modelling. Although not a central focus of this thesis, the ablation measurements (Section 3.1.3) and a melt-out experiment (Section 3.1.4) provided valuable insights into the complex dynamics of a debris-covered glacier system.

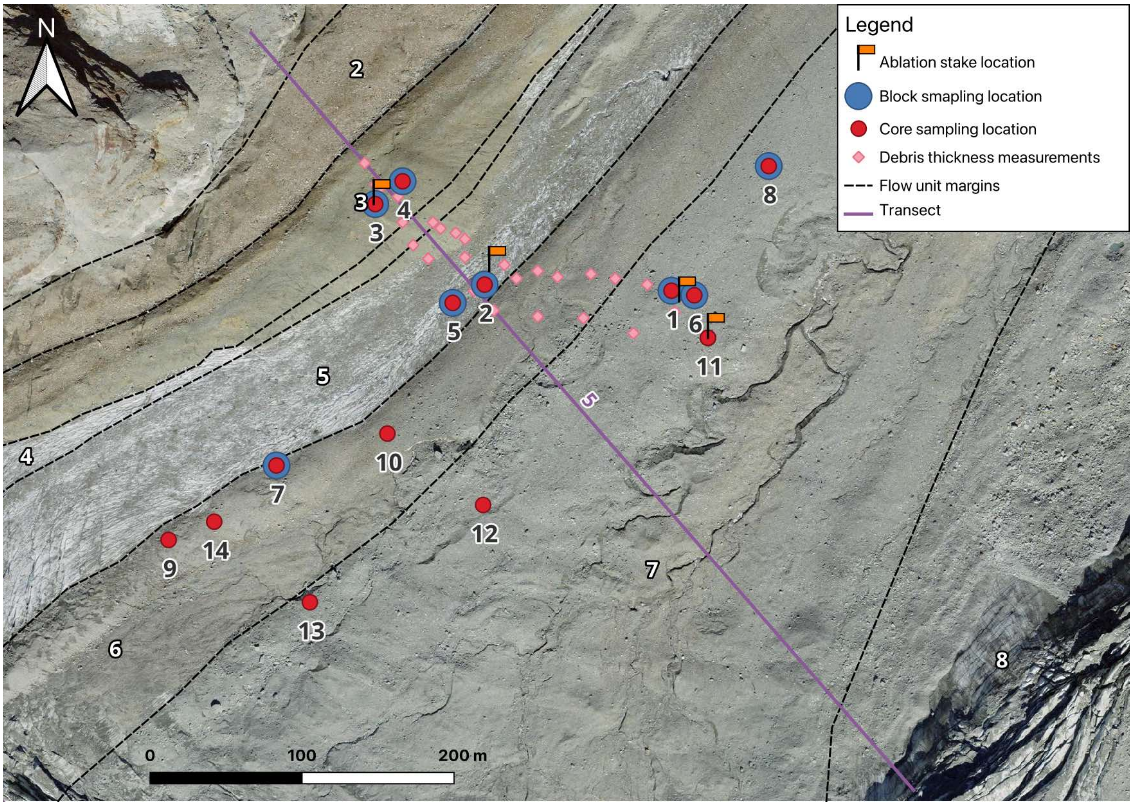

Figure 3.1: Close-up map of the study site in the upper ablation area of Zmuttgletscher. Illustrated are several measurement points, including ablation stake locations (orange flags), debris thickness measurement locations (pink diamonds), as well as Block Sampling (blue circles) and Core Sampling sites (red circles) numbered from 1 to 14. Transect line number five (violet, see Section 4.2.6) crosses the field work area from NW to SE and black dashed lines represent the margins of the respective flow units (white numbers). The Background image is an orthophoto from 2023 (Swisstopo, 2023).

3.1.1 Englacial Debris Concentrations

As discussed in Section 2.2, reports of englacial debris concentrations remain scarce. Previous studies have often relied on melt-out experiments to infer englacial debris concentrations by studying the surface emergence of englacial debris over time (e.g. Kirkbride and Deline, 2013). However, these experiments are typically labour-intensive and invasive as they require extensive surface areas to be cleared of all supraglacial debris. More recent approaches utilize boreholes coupled with optical televiewers to document the vertical distribution of englacial debris (Miles et al., 2021). Although this method provides high vertical resolution, it involves substantial logistical challenges and costs, often limiting the spatial coverage of such measurement campaigns.

To facilitate a comparison between flow units, six initial sampling locations (1–6) were established, with two sites in each defined flow unit (Figure 3.1). The sampling methodologies were applied in close proximity to each other to ensure a direct comparison (Figure 3.2). As time allowed, two additional comparison sites, one up-glacier (7) and one down-glacier (8), and six additional Core Sampling sites (9–14) were established to increase spatial resolution.

To quantify the englacial debris concentrations, two distinct sampling methods were applied: **Block Sampling**, is an invasive, labor-intensive approach designed to extract larger volumes of ice; **Core Sampling** is a more efficient and less invasive method utilizing smaller ice cores. The two methods were selected to evaluate their field applicability and to compare their outcomes, with the aim of formulating recommendations for future research.

The two sampling methods represent a modification of traditional large-scale melt-out experiments previously used to investigate englacial debris concentrations (Kirkbride and Deline, 2013). In contrast to these approaches, the methods applied in this study focus on smaller plots that must be cleared of debris. Additionally, the extraction of the samples from the glacier and the crushing of larger samples accelerate the melt rate, effectively reducing the experiment timescale.

Block Sampling (BS)

The Block Sampling method was designed to mitigate the influence of small-scale spatial variability in the debris distribution by extracting a substantial volume of ice. Given that englacial debris concentrations are generally very low (Table 2.1), the presence of individual large clasts or debris clusters can significantly influence the englacial debris concentration. The BS approach aims to enhance statistical robustness by increasing the sampled ice volume, thereby reducing the influence of stochastic outliers.

For this, a plot of roughly 80×80 cm was first cleared of all supraglacial debris and the weathering crust. A block measuring approximately 50×50 cm with a depth of 25 cm (limited by the length of the chainsaw blade) was cut into the cleaned glacier surface with the help of a chainsaw (Figure 3.2). Using clean ice picks, the ice sample was broken into more manageable pieces to be extracted from the glacier. The ice pieces were evenly but not systematically distributed into three labeled sampling buckets. Each bucket, containing roughly a third of the sampled ice, was weighed using a field scale before the ice was spread onto labeled plastic trays, left to melt under direct sunlight.

Figure 3.2: Comparison of cleared glacier area between the Block Sampling (left) and the Core Sampling (bottom right), highlighting the spatial differences of the respective methodologies. Top right image shows the Core Sampling extraction method (ice core drill) in action.

Core Sampling (CS)

The Core Sampling methodology was designed to reduce the labour requirements associated with each individual sample, facilitating a higher sample frequency,and thus an increase in the total number of samples that can be obtained. Consequently, this approach is intended to enhance the spatial resolution of the resulting data set.

For this, a small plot of roughly 10×10 cm was first cleared of all supraglacial debris and the weathering crust. With the help of an ice core drill with a diameter of 5 cm (Figure 3.2) an ice cylinder, approximately 25 cm long, was extracted from the glacier, with the depth being constrained by the length of the drill. These ice cores were then packed into labeled sampling bags and transported back to the camp, for weighing using a field scale. The cores were left to melt inside their sealed sampling bags under the sun to ensure that no debris was lost during the process.

Regardless of the collection method, a standardized procedure was used to process the meltwater and isolate the debris. In a first step, the meltwater from each sample was visually assessed to determine whether the amount of debris was substantial enough to exceed the measurement error margin constrained by the inconsistent filter weight. Samples containing insignificant debris or only suspension were excluded from further processing, and their debris weight was recorded as zero or not measurable.

The meltwater from samples containing sufficient debris was passed through coffee filters with a pore size of 10–20 μm to retain debris particles. Once filtration was complete, the labeled filters were packed into plastic sampling bags for transport. The final processing was conducted at the UZH Laboratory, where the filters were dried and measured to determine the mass of the englacial debris. Englacial debris concentrations are reported as vol.% assuming densities of 917 $\mathrm{kg/m^3}$ for ice and a debris density of 2000 $\mathrm{kg/m^3}$.

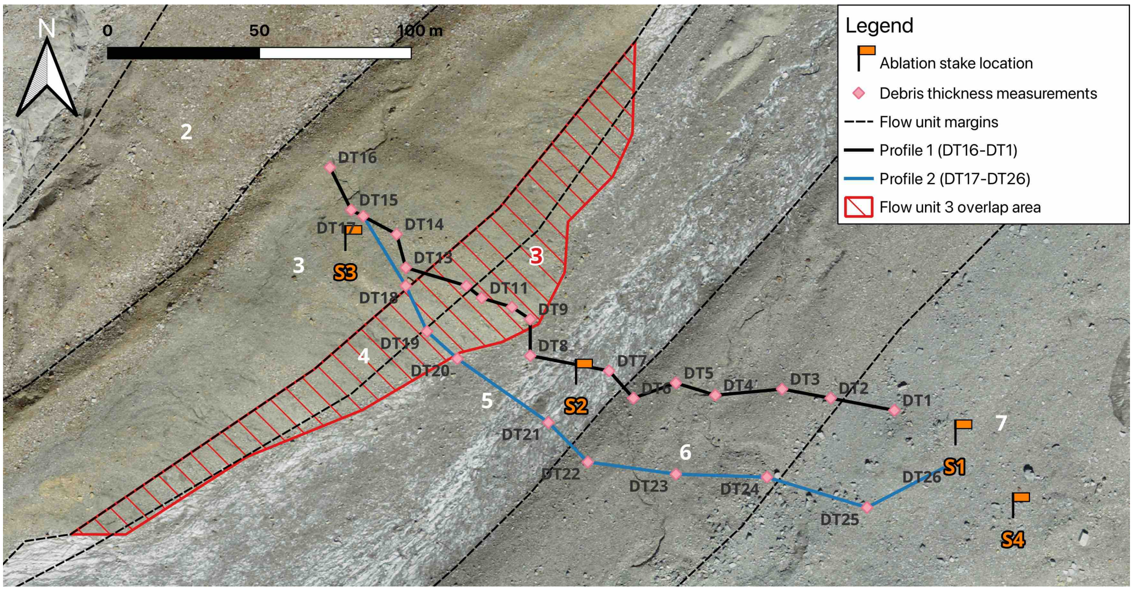

Figure 3.3: Close-up map of the study site in the upper ablation area of Zmuttgletscher, showing the two debris thickness profiles connecting individual measurement locations (pink diamonds): Profile 1 (DT16–DT1, black line) and profile 2 (DT17–DT26, blue line). Ablation stake locations (S1–S4) are indicated in orange and flow units 2–7 (white) are delineated by dashed black lines. The red hatched area marks the overlap zone of flow unit 3, where supraglacial debris from that unit buried parts of the underlying flow units 4 and 5. The Background image is an orthophoto from 2023 (Swisstopo, 2023).

3.1.2 Debris Cover Thickness

The thickness of the debris cover was measured to get a better understanding of the flow unit characteristics and how this relates to englacial debris concentration. The debris cover data provide an additional constraint for the validation of the numerical modelling outputs. The thickness was measured at each location where the debris concentration samples were collected. Additional measurements were obtained along two transects that spanned the flow units investigated during the field work to further capture the spatial distribution (Figure 3.1). To mitigate the bias introduced by small-scale debris cover variability, three individual measurements were obtained within a radius of roughly 50 cm at each sampling site, which were later averaged to represent the thickness of the local debris cover.

The measurement procedure involved carefully clearing a small patch of debris to expose the underlying ice surface while minimizing the disturbance to the surrounding debris structure. The thickness was determined by placing an ice pick horizontally across the cleared plot, resting on the surface on the adjacent undisturbed debris cover. The distance was then measured vertically from the underside of the ice pick to the clean lacier surface. Where debris cover was non-consistent (patchy), a surface coverage ratio was estimated for the site. This method ensured a consistent reference level for the debris surface and provided a reliable estimate of the total thickness of the debris layer at each point.

3.1.3 Ablation

To quantify surface melt rates across the study area, ablation was measured at four distinct locations (Figure 3.3) using labeled PVC ablation stakes. Each stake, composed of two hinged two-meter segments, was drilled to a depth of three to four meters into the glacier. The initial measurement was recorded during the first visit to the study site in July 2025, with the final readings taken during the follow up visit 28-days later, on 6 August.

One stake was installed within each of the flow units, identified in the field (Section 3.1.1), positioned in close proximity to the respective englacial debris concentration sampling sites, to capture the distinct ablation dynamics of the flow units. At each of these measurement sites, the supraglacial debris was temporarily removed to expose the surface for a precise reading of the stake height. After the measurement was conducted, the debris cover was carefully replaced as good as possible to match its original state to ensure that the thermal insulation remained representative of the surrounding area. The final stake was placed within the melt-out experiment plot to provide a "clean ice" reference and to track surface lowering and debris emergence over time (Section 3.1.4).

3.1.4 Melt-Out Experiment

To monitor the emergence of englacial debris and its transition to a debris cover over time, a 2.5×2.5 m melt-out experiment plot was established at sampling site 14 (Figure 3.1). The designated area was first cleared of all supraglacial debris and the weathering crust was removed using ice picks to expose the underlying bare ice surface. An ablation stake marked at 10 cm intervals was installed in the centre of the plot, to provide reference for surface lowering. A wildlife camera was mounted on a large boulder adjacent to the plot to capture the melt process and debris emergence in high temporal resolution (hourly interval or upon motion detection). This setup allowed for a higher temporal resolution in the ablation calculations over the 28-day study period. The data was retrieved during the follow-up field campaign on 6 August.

3.2 Glacial Feature Mapping

3.2.1 Flow Units

The mapping of glacier flow units is based on the premise that unique tributary catchment characteristics form distinct flow units down-glacier, where the supraglacial debris cover is a reflection of the respective origin (Section 2.1.2).

Using the geographic information system software QGIS (QGIS Development Team, 2026), flow units were delineated by integrating information from multiple high-resolution datasets. The primary data source for identifying flow unit boundaries was the latest SWISSIMAGE (Swisstopo, 2023) orthophoto, which allowed for the detection of surface features such as the debris emergence locations and variations in debris lithology, primarily identified through color differences in the debris cover. To verify these boundaries against the underlying glacier geometry, the SWISSALTI3D digital elevation model (Swisstopo, 2024b) was consulted. Furthermore, historical maps (e.g. Siegfried-, Dufour-, and Landeskarten) and multi-temporal orthoimages provided by Swisstopo (2026) were consulted to compare these results against long-term evolutionary trends of the glacier surface.

Flow units were identified based on three main criteria: (1) the location of debris emergence; (2) surface topography; and (3) distinct variations in the color of the debris cover. Flow unit mapping began in the upper ablation area of Zmuttgletscher, where the field work site is located. Although flow units are distinguishable in this area, boundaries become increasingly difficult to detect down-glacier due to the remobilization processes of supraglacial debris. For the purpose of this thesis, flow units were not mapped on the Schönbielgletscher and the main arm of the Stockjigletscher tributaries, as the research focus is on the upper ablation area of the Zmuttgletscher. However, these tributaries only (barely) connect to the lower ablation area of the Zmuttgletscher tongue, where flow unit detection becomes significantly more challenging due to surface debris dispersal causing mixing.

Following their identification the upper ablation area, the flow units were traced

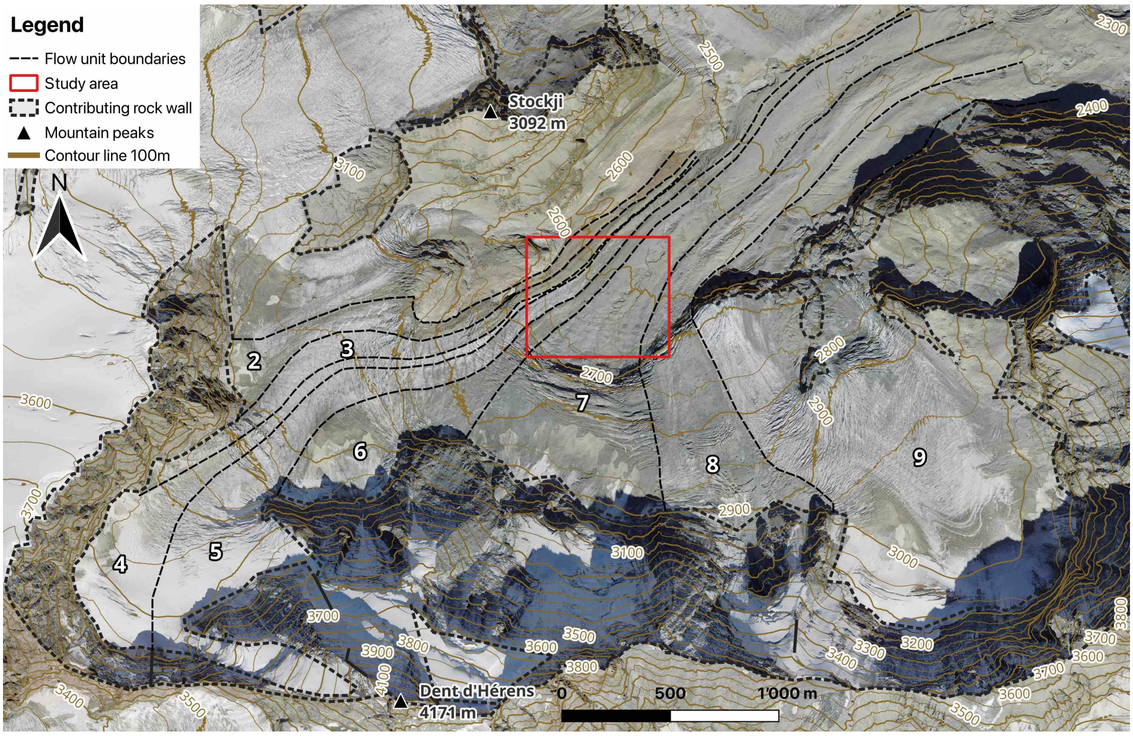

Figure 3.4: Close-up map of the study site (red box) in the upper ablation area of Zmuttgletscher, displaying the flow unit margins (dashed black lines) that delineate the flow units 1–9 (white) based on the criteria in Section 3.2.1. The Background image is an orthophoto from 2023 (Swisstopo, 2023).

up-glacier to their respective origins at the base of steep head walls in the accumulation area. This reconstruction was achieved by inferring ice flow paths based on topography, supraglacial debris patterns, and glacier dynamic features such as faults, crevasse patterns and icefalls retrieved from the above mentioned datasets. The resulting flow units are displayed in Figure 3.4.

Figure 4.1.2 displays the only area where the criteria were not strictly applied. In this region, large surface elevation differences between the mapped flow units 4 and 5, clearly distinguishable by their absent or patchy debris cover, and the fully debris-covered flow unit 3 led to the gravitational reworking of supraglacial debris. This expresses itself in a debris cover overlap (red hatched area in Figure 4.1.2) in this region. Since flow units 4 and 5 become clearly traceable again below the study area, this feature was interpreted as a local overlap and rather than a flow unit shift. The associated topographic difference is visible in the debris thickness profiles presented in the Results chapter (Figure 4.2).

3.2.2 Debris Source Areas

Following the delineation of the flow units, the respective debris source areas were identified by analyzing the morphology of the surrounding headwalls. Potential gravitational debris pathways were inferred by consulting SWISSIMAGE (Swisstopo, 2023), SWISSALTI3D (Swisstopo, 2024b), and historical maps and orthoimages (Swisstopo, 2026). This assessment was further supplemented by the spatial distribution of debris deposition cones previously mapped by Ganarin (2019). By tracing these paths from the head walls down to the glacier surface, the boundaries of the debris source areas were established (Figure 3.5). This provided the spatial link between sediment production and subsequent debris entrainment within each specific flow unit.

Table 3.1: Topographic characteristics of the 14 source areas defined in Section 3.5. Mean, minimum and maximum elevations (m a.s.l.) derived from the SWISSALTI3D elevation model (Swisstopo, 2024b), and surface extent (km^2) are reported for each source area.

	Elevation [m a.s.l.]			
Source Area ID	Mean	Min.	Max.	Area [km^2]
1	3261.36	3010.82	3502.96	0.11
2	3265.97	2992.29	3541.17	0.14
3	3377.12	3095.45	3629.81	0.13
4	3534.32	3253.80	3799.09	0.33
5	3610.93	3298.45	4147.26	0.29
6	3458.20	2824.63	4173.24	0.49
7	3306.75	2825.39	4095.48	0.89
8	3237.42	2881.26	3700.05	0.46
9	3381.51	2528.77	4467.24	1.69
10	2886.44	2367.43	3883.57	1.12
11	3028.10	2848.96	3103.87	0.17
12	2849.27	2562.01	3092.49	0.22
13	3259.37	2707.88	3712.24	1.39
14	3593.58	3058.82	4356.69	1.70

3.2.3 Glacier Extent

Little Ice Age (LIA)

The Little Ice Age (LIA, 1260–1850) refers to a period of sustained cooling during the most recent Holocene, causing repeated and extensive glacier advances across many mountain ranges (Nicolussi et al., 2022). Most glaciers reached their maximum during the most pronounced cooling phase at the end of the LIA, between the 16th and mid 19th centuries (Nicolussi et al., 2022). These advances deposited prominent terminal and lateral moraines that remain well-preserved in many glaciated landscapes today, providing a clear geomorphological record of past ice margins. The LIA moraines of Zmuttgletscher were identified by consulting the SWISSIMAGE (Swisstopo, 2023) as well as the 'Geologischer Atlas der Schweiz' (Swisstopo, 2024a). In this study, the LIA moraine positions are used as a spatial reference against which the glacier model is validated.

In this study, the LIA moraine positions (Figure 3.5) are used as a spatial reference against which the glacier model is validated. Agreement between the modelled ice margin at its maximum state and the mapped moraine record indicates that the model correctly reproduces the glacier's sensitivity to climate forcing and its dynamic response.

Today

The present-day extent of Zmuttgletscher has similarly been mapped to provide an additional spatial validation metric of the model (Figure 3.5). More importantly, however, it acts as a reference state for interpreting the model outputs. Since the climatic forcing applied in this study (more in Section 3.3.8) represents a simplified approximation of climatic trends, rather than the precise conditions of each historical year, a given model time step does not necessarily correspond directly to its calendar year. The present-day glacier extent is therefore used to identify the model time step(s) at which the simulated glacier geometry most closely resembles the current glacier state. Subsequently, the results of these time steps are compared against the present-day measurements from Zmuttgletscher.

3.3 Modelling Components

3.3.1 Instructed Glacier Model (IGM)

Ice flow is simulated using IGM (v3.0.0, Jouvet et al., 2022; Jouvet et al., 2024), a higher-order (three-dimensional), physics-informed, thermo-mechanically coupled glacier evolution model. In contrast to traditional models that rely on computationally expensive Full-Stokes solvers or Blatter Pattyn equations (e.g. OGGM (Maussion et al., 2019) and PyGEM (Rounce et al., 2020)), IGM utilizes a Convolutional Neural Network to emulate the ice velocity field (Jouvet and Cordonnier, 2023). This physics-informed deep learning approach enables efficient computation on Graphics Processing Units (GPUs), significantly reducing computation times (Jouvet et al., 2022). Additionally, the GPU-based model architecture facilitates efficient the parallelization of Lagrangian particle tracking, which is essential for the simulation and tracking of large numbers of particle trajectories (Leger et al., 2026).

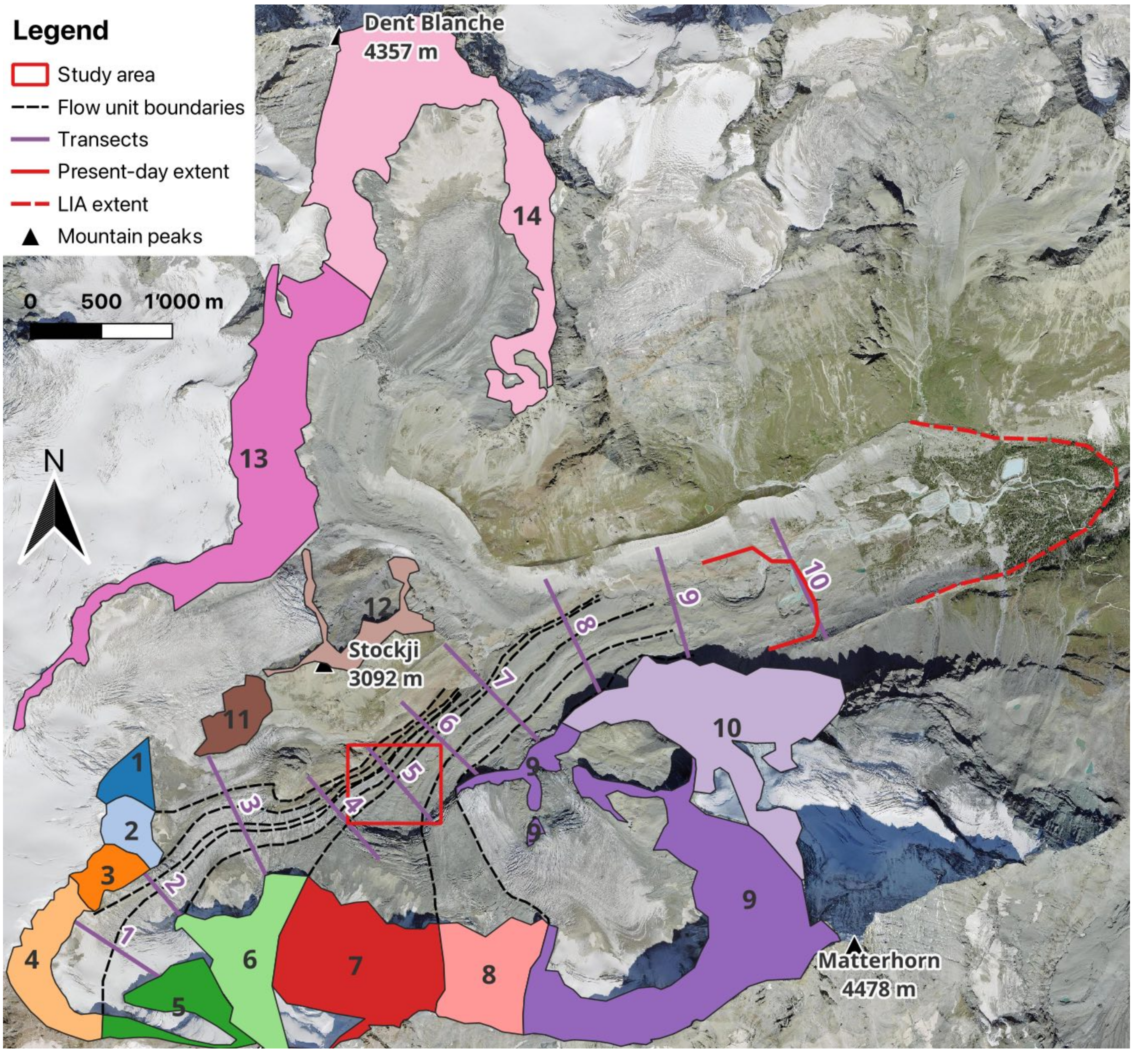

Figure 3.5: Overview of the mapped source areas (colored) and their respective flow unit boundaries (dashed black lines). The present-day (solid), Little Ice Age (LIA, dashed) extents and study area (box) are marked in red. Transects used to used to display the englacial debris distribution are displayed in violet. The Background image is an orthophoto from 2023 (Swisstopo, 2023).

The following sections serve as a short overview of the most important underlying physical equations that govern the glacier evolution within IGM (Jouvet et al., 2024). The evolution of the ice thickness $h(x, y, t)$ (3.1), is determined by the mass conservation equation, which relates the the change in elevation to ice dynamics and surface mass balance through the following equation:

$$\frac{\partial h}{\partial t} + \nabla \cdot (\bar{\mathbf{u}} h) = \text{SMB}, \tag{3.1}$$

where $\partial h/\partial t$ is the temporal change in ice thickness, $\nabla \cdot (\bar{\mathbf{u}} h)$ is the flux divergence and SMB represents the addition or removal of ice mass on the glacier surface.

The ice flow dynamic (3.2) is modelled using a physics-informed deep learning emulator (Jouvet et al., 2022), which is based on the computationally expensive Glen–Stokes equation (Glen's flow law):

$$D = A\tau^n, \tag{3.2}$$

where D is the strain rate, τ represents the deviatoric stress tensors, with A representing the temperature dependent rate factor and as n is Glen's flow law exponent, typically set to $n = 3$ for temperate ice.

The SMB (3.3) model of IGM is represented in a linear relationship between ELA and altitude:

$$\mathrm{SMB}(z) = \begin{cases} \min\big(\beta_{\mathrm{acc}}(z - z_{\mathrm{ELA}}),\, m_{\mathrm{acc}}\big), & z > z_{\mathrm{ELA}}, \\ \beta_{\mathrm{abl}}(z - z_{\mathrm{ELA}}), & \text{otherwise}, \end{cases} \tag{3.3}$$

where z is the altitude, z_{ELA} is the ELA, β_{abl} and β_{acc} are ablation and accumulation gradients, while m_{acc} defines the maximum allowed surface accumulation.

3.3.2 The debrisIGM Module

The version of IGM used in this thesis includes specialized modules currently under development by Hardmeier et al. (2025) within the Glaciology and Geomorphodynamics Group at the University of Zurich. These extensions were designed specifically to model the dynamics of debris-covered glaciers. This integrated framework, hereafter referred to as **debrisIGM module**, allows for a comprehensive simulation of the life cycle of glacial debris, from its seeding, over its entrainment, to its eventual impact on surface ablation.

The debrisIGM module provides a variety of seeding options to modulate the debris supply (Section 3.3.3). To simulate the movement of these debris particles, the debrisIGM module uses an adaptation of the standard IGM *'particles'* module. This module facilitates the Lagrangian transport of both englacial and supraglacial debris by tracking discrete particles as they move through the three-dimensional ice velocity field (Section 3.3.4; Leger et al., 2026). Crucially, the model accounts for the accumulation of these particles on the surface to calculate the evolution of supraglacial debris thickness and its feedbacks with the SMB (Section 3.3.6).

3.3.3 Particle Seeding Scheme

The debrisIGM uses a debris seeding scheme as a representation of debris supply from headwall erosion processes. At each time step, particles are generated or **seeded** for each grid cell which is part of the scheme. The debrisIGM module

(Hardmeier et al., 2025) offers five debris seeding configurations. The scheme employed in this thesis utilizes predefined particle seeding areas, defined as polygons in a shapefile (.shp), which are hereafter referred to as source areas, to be combined with a set of seeding conditions:

- Topographic masking: A minimum surface slope threshold is used to generate a binary mask to ensure debris is only seeded within sufficiently steep terrain.
- Ice thickness threshold: A specific ice thickness threshold is applied to restrict particle seeding to areas with minimal or zero ice cover. This threshold also accounts for minor numerical modelling artifacts where thin layers of ice might be erroneously simulated on steep slopes.
- Debris input rate: The debris supply is defined by a temporally variable input rate ($\mathrm{mm\,yr^{-1}}$), which determines the thickness used to calculate the debris supply volume per area. This in turn determines the specific volumes attributed to each generated particle seeded within the area.
- Volumetric scaling: Particle volumes are corrected to account for the disparities between the true surface area of steep slopes and the flat pixel area of the grid and the seeding interval. Therefore, particles originating on steep slopes exhibit larger volumes than those on flatter surfaces.
- Relocation scheme: A dedicated transport algorithm is applied to realistically redistribute the particles from their initial seeding locations to their resting point on the glacier surface by accounting for slope and gravitational pathways.
- Seeding delay: A seeding delay allows a debris free glacier build up at the beginning of the simulation.

The particles that started to generate during the spin-up period at the beginning of the simulation possess several key attributes to facilitate precise particle tracking (Table 3.3). Most importantly, each particle is assigned a unique ID, sub-grid-resolution coordinates (x, y, z), and a source area ID. This allows for the precise retracing of particles back to their origin in a user-defined source area, enabling a detailed analysis of which source areas contribute to which flow unit debris cover.

3.3.4 Particle Tracking Scheme

The debrisIGM module (Hardmeier et al., 2025) uses an adapted version of IGMs '*particles*' module to simulate the three-dimensional debris transport trajectories.

In this scheme, the particles are treated as passive Lagrangian tracers advected by the three-dimensional ice flow field produced by the IGM ice flow emulator. To ensure high spatial resolution, particle positions are resolved at sub-grid resolution. This allows the model to maintain precise particle trajectories.

Supraglacial particles are subject to lateral diffusion based on local slopes. Particles that reach the ice margin are subject to off-glacier deposition, where they accumulate to form moraines, altering the bed topography, and immobile particles aggregate to reduce computation time. The model allows for deposited particles to be remobilized by an advancing glacier.

3.3.5 Englacial Debris Concentration Calculations

The debrisIGM module calculates the englacial debris concentration at grid cell resolution for each time step. At every time step, the volumes of all particles within a given grid cell are summed and divided by the volume of the corresponding ice column:

$$C_{\text{debris}}[vol.\%] = \frac{\sum w}{A_{\text{grid}} \cdot h} \cdot 100 \tag{3.4}$$

where C_{debris} is the englacial debris concentration, $\sum w$ is the sum of all particle volumes within the grid cell, A_{grid} is the grid cell area ($50 \times 50\,m$), and h is the ice thickness at that cell.

To better represent englacial debris concentrations around the sampling locations, this study instead sums the volumes of all particles within a defined radius R of each sampling site. For each particle within this radius, the location specific ice thickness is retrieved, and a mean ice thickness $\bar{H}_{\text{ice}}$ is computed. The debris volume is then divided by the corresponding ice column volume:

$$C_{\text{debris}}[vol.\%] = \frac{\sum w}{\pi R^2 \cdot \bar{H}_{\text{ice}}} \cdot 100 \tag{3.5}$$

Both approaches allow for vertical resolution of the englacial debris concentration by filtering particles according to their relative height (r) within the ice column. This creates the possibility to study how the debris concentrations varies between the whole ice column (r$\in [0, 0.99]$) and certain ice column bands, like the uppermost part of the ice column (r$\in [0.8, 0.99]$ or r$\in [0.9, 0.99]$), which becomes essential for comparison with the in-situ measurements (Section 4.2.2). Section 4.2.6 similarly uses the relative height to take a closer look at the vertical distribution, but instead of applying a radius, it uses the grid cell resolution and applies the same logic.

3.3.6 Debris cover effects on SMB

Within the debrisIGM module (Hardmeier et al., 2025) particles are classified as supraglacial debris, once they emerge on the glacier surface, which is represented by a relative height within the ice column of $r = 1$. The debris cover thickness (D) of a pixel is determined by summing the individual volumes of all supraglacial particles. The cumulative volume is then distributed uniformly across the pixel's surface area with a correction factor accounting for the debris cover porosity. To simulate the impact of this debris layer, a simple Østrem curve approach (3.6) is used to modulate the SMB. This approach accounts for the non-linear relationship between debris thickness and underlying surface ablation (see Section 2.1.3. This debris-covered mass balance (SMB_{debris}) is calculated using the following equation:

$$SMB_{debris} = SMB \frac{D_0}{D_0 + D}, \tag{3.6}$$

where SMB is the debris-free ('clean-ice') mass balance, D_0 is the user defined characteristic debris thickness, and D is the local debris thickness. The D_0 parameter serves as a sensitivity threshold representing the specific thickness at which the ablation rate is reduced to exactly half of its debris free equivalent. This debrisIGM module establishes a feedback loop where the emergence and redistribution of englacial debris dynamically dictate the spatial patterns of surface melt, and with that the mass balance of the glacier.

Table 3.2: Selection of the used model parameters and constants

Parameter	Description	Value	Units
–	Grid resolution	50	m
z_{ELA}	Equilibrium Line Altitude	3000 – 3350	m a.s.l.
β_{abl}	Ablation gradient	0.009	$\mathrm{m\,m^{-1}\,yr^{-1}}$
β_{acc}	Accumulation gradient	0.005	$\mathrm{m\,m^{-1}\,yr^{-1}}$
m_{acc}	Maximum accumulation	2	m
–	Avalanche Interval	5	yr
–	Seeding delay	50	yr
–	Seeding interval	1	yr
–	Debris input rate	0.5	$\mathrm{mm\,yr^{-1}}$
–	Slope threshold	45	°
–	Ice thickness threshold	20	m
ϕ	Debris porosity	0.3	–
D_0	Characteristic debris thickness	0.065	m

3.3.7 Model Inputs and Outputs

This Section outlines the relevant input parameters used to set up the debrisIGM module and summarizes a small selection of output variables that are calculated and stored by the debrisIGM module.

The configuration of the input parameters of the model used in this thesis (Table 3.2), is based on previous model experiments conducted by (Hardmeier et al., 2025), which showed high fidelity in reproducing the evolution of Zmuttgletscher. Given the limited time available, this thesis focused on exploring the ELA evolution for an accurate reconstruction of Zmuttgletscher, an essential parameter for reproducing the long-term evolution of Zmuttgletscher, while keeping all other parameter values constant. This parameter was prioritized because of its fundamental influence on the glacier's mass balance (Section 3.3.6). Section 3.3.8 provides a more detailed description of the ELA evolution selected for this study.

Table 3.3 shows a selection of values calculated and stored by the model. Most of them are spatially and temporally resolved, facilitating post-processing of the glacier evolution and data visualization over time and space.

Table 3.3: Selection of model output variables. Temporally resolved particle variables (below the line) are stored in separate CSV files.

Variable	Description	Units
h	Ice thickness	m
SMB	Surface mass balance	$\mathrm{m\,yr^{-1}}$
D	Debris cover thickness	m
–	Englacial debris concentration	Vol. ratio
–	Vertically resolved englacial debris concentration	Vol. ratio
–	Debris flux	$\mathrm{m^3\,m^{-1}\,yr^{-1}}$
–	Depth-averaged velocity magnitude of ice	$\mathrm{m\,yr^{-1}}$
–	Avalanche balance	$\mathrm{m\,yr^{-1}}$
ID	Particle ID	–
x, y, z	Particle position (UTM)	m, m, m a.s.l.
r	Relative height within the ice column	0:bed, 1:surface
t	Particle seeding timestamp	yr
$englt$	Englacial transport duration	yr
w	Assigned debris volume	$\mathrm{m^3}$
$srcid$	Source area ID	–

3.3.8 ELA Evolution - Climatic Forcing

In this study a simplified representation of past climatic conditions was used to reconstruct the Zmuttgletscher evolution while reducing complexity. The debris

IGM was initialised with an ice-free bedrock topography and no debris input. The surface mass balance was then forced with a constant ELA of 3150 m a.s.l. for 600 years, allowing the modelled glacier to reach a steady state (spin-up phase). Debris input was introduced after a delay of 50 years, when the the model had built up a small debris-free ice mass. The ELA for this spin-up phase was not designed to produce a representative glacier for that time period, but rather to establish a simplified initial glacier extent that could then be forced by the more recent climatic history.

After the initial 600 years spin up phase (at model time step 1600), the ELA was instantaneously reduced to 3000 m a.s.l. and kept constant at this height for the 250-years duration of the pronounced cooling phase at the end of the LIA (Nicolussi et al., 2022). This study specific LIA ELA was defined through an explorative approach, taking the LIA ELA of 2930 m a.s.l. defined for Zmuttgletscher by (Henz et al., 2025) as a starting point. Numerous model runs were conducted, to explore different ELAs while keeping the other inputs constant, until the LIA ELA adopted here fixed based on promising model results (more in Section 4.2.1).

Following the pronounced LIA cooling phase, the ELA was increased by 350 (1.75 m per year) from 3000 m at model time step 1850 to 3350 m a.s.l. by time step 2050, based on reported SMB evolutions from glaciers in the surrounding area (Huss et al., 2025a; GLAMOS, 2024).

4. Results

This chapter presents the results of the in-situ measurements from Zmuttgletscher (Section 4.1) and the subsequent modelling using the debrisIGM module (Section 4.2). The field campaign yielded englacial debris concentrations (Section 4.1.1), debris cover thickness measurements (Section 4.1.2), and ablation rates (Section 4.1.3), as well as insights from the melt-out experiment (Section 4.1.4). The modelling results cover (i) the reconstruction of Zmuttgletscher and the definition of the present-day reference times step (Section 4.2.1); (ii) the evolution (Section 4.2.2) and spatial distribution (Section 4.2.3) of the modelled englacial debris concentrations, together with the modelled debris thickness distributions (Section 4.2.4) are compared to the in-situ measurements; (iii) the supraglacial (Section 4.2.5) and englacial (Section 4.2.6) debris particle distributions are compared to the mapped flow units; and (iv) the englacial transport times of particles are presented according to their source area (Section 4.2.7).

4.1 In-situ measurements on Zmuttgletscher

4.1.1 Englacial Debris Concentrations

The results of the englacial debris concentration sampling are summarized in Table 4.1, while Figure 4.1 consolidates these measurements together with the debris cover thickness and ablation rate per flow unit. Overall, englacial debris concentrations were very low throughout the study area, ranging from zero to 0.0414 vol.%. Despite these consistently low values, the concentrations varied significantly between the different flow units. The differences between the sampling methods are evident, with the BS method continuously reporting englacial debris concentrations, while the CS method often reported a non measurable amount of debris (zero vol.%).

Flow unit 3 exhibited the highest englacial debris concentrations recorded, while also showing the greatest spread in measured values (Figure 4.1). Site 3 in particular yielded the maximum values of the study for both methods, with concentrations of 0.0414 vol.% for the BS method and 0.0382 vol.% for the CS method. At site 4, the concentrations were significantly lower (0.0160 vol.% for BS), but still exceeded those of all remaining sites, while no measurable amount of debris was detected using the CS method. The debris cover thickness was observed to be 9.7 cm at site 3 and 7.2 cm at site 4, which agrees well with the mean debris cover thickness reported for flow unit 3 (approximately 7.5 cm ;Figure 4.1).

Flow unit 5 showed the lowest englacial debris concentrations of all units (< 0.0005 vol.%). Although the BS method captured some englacial debris, 0.018 g (site 2) and 0.346 g (site 5) respectively, no measurable amount of debris was found in either of the CS samples. Both sites were characterised by a non-continuous debris cover, covering approximately 60 % of the glacier surface, while not resulting in a measurable thickness.

Flow unit 6 displayed low englacial debris concentrations, with only two sites yielding measurable values: 0.0036 vol.% at site 7 (BS) and 0.0032 vol.% at site 14 (CS). The remaining CS sites reported non-measurable amounts of debris. The thickness of the debris cover was measured at a single site in the flow unit and recorded 3.3 cm (site 7), one of the lower values for that flow unit, as the mean debris cover thickness reported for flow unit 6 is approximately 5 cm (Figure 4.1).

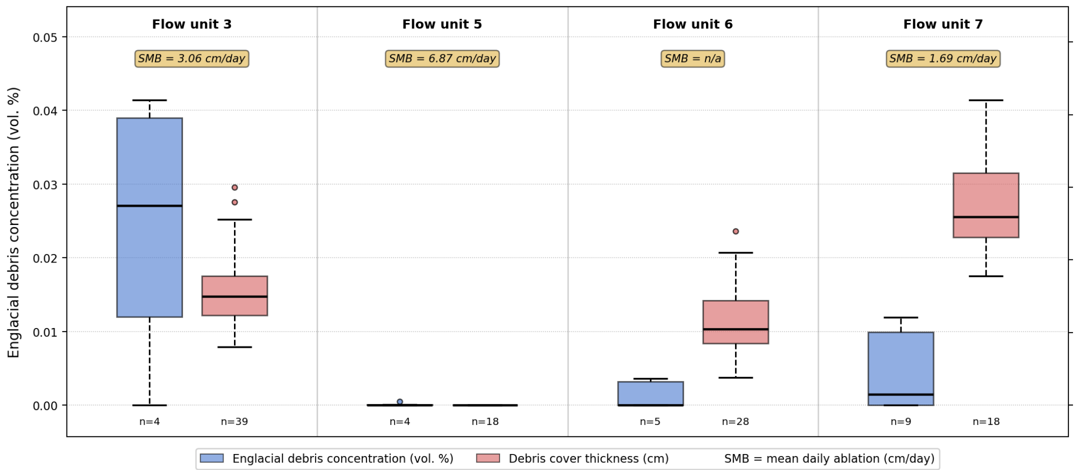

Figure 4.1: Englacial debris concentrations (vol.%, blue, left axis) and debris cover thickness (cm, red, right axis) for flow units 3, 5, 6 and 7, that includes all individual debris thickness measurements found in Table B.1. Boxes represent the interquartile range (IQR); the horizontal line indicates the mean. Whiskers extend to 1.5 times the IQR, and circles denote outliers. Sample sizes (n) are shown below each box plot. Mean daily ablation rates (SMB, cm/day), derived from stake measurements are annotated for each flow unit; no ablation data is available for flow unit 6 (n/a).

With a mean debris cover thickness of approximately 13 cm, flow unit 7 recorded the maximum measured values of all flow units (Figure 4.1). The highest concentrations of this flow unit were recorded at site 1 (0.0119 vol.% (BS) and 0.0118 vol.% (CS)). In contrast, site 8, located slightly further down the glacier (Figure 3.1), showed a nearly negligible concentration (0.0005 vol.% for BS and zero vol.% for CS), while exhibiting a debris cover thickness of 11.4 cm. Site 12, with a maximum debris cover thickness of 27.7 cm, yielded no measurable debris with the CS method (BS not performed).

Table 4.1: Recorded englacial debris concentration displaying the results according to the sampling methodology.

Flow Unit	Site	Avg. Debris Thick. [cm]	Block Sampling (BS)			Core Sampling (CS)		
			Sample [kg]	Debris [g]	Conc. [vol.%]	Sample [kg]	Debris [g]	Conc. [vol.%]
3	3	9.7	28.22	25.448	0.0414	0.84	0.7	0.0382
	4	7.2	34.04	11.852	0.0160	0.85	n.m.	0
5	2	patchy	31.21	0.018	0.0000	0.84	n.m.	0
	5	patchy	31.89	0.346	0.0005	0.83	n.m.	0
6	7	3.3	32.55	2.559	0.0036	0.80	n.m.	0
	9	–	–	–	–	0.89	n.m.	0
	10	–	–	–	–	1.06	n.m.	0
	14	–	–	–	–	0.78	0.055	0.0032
7	1	16.3	31.05	8.051	0.0119	0.79	0.204	0.0118
	6	15.7	30.09	1.006	0.0015	0.77	0.167	0.0099
	8	11.4	27.19	0.273	0.0005	0.66	n.m.	0
	11	–	–	–	–	2.49	0.274	0.0050
	12	27.7	–	–	–	0.65	n.m.	0
	13	11.7	–	–	–	0.82	n.m.	0

Note: *Volume calculations were based on an ice density of 917 kg/m^3 and a debris density of 2000 kg/m^3. "Patchy" indicates a non-continuous debris cover (approximately 60 % surface area coverage), while – indicates that no measurements were recorded at that site. 'n.m.' indicates samples where the debris amount was visually assessed as non-measurable.*

Across all flow units, the BS method, which processed significantly more ice per sample (∼ 30 kg), consistently detected debris, even in cases where the CS method (∼ 0.8 kg per sample) did not record a measurable amount of debris. The BS concentrations equalled or exceeded the CS values at all sites, except for site 6, where the CS method returned a higher concentration than the BS (0.0099 vol.% compared to 0.0015 vol.%). In locations with higher debris concentrations, such as site 1 and 3, both methods produced comparable results. The exception to this is site 4 (0.0160 vol.% for BS and zero vol.% for CS).

4.1.2 Debris Cover Measurements

The debris cover for sampling sites 1–8 has already been presented in Table 4.1 and Figure 4.1. A full table of all debris cover thickness measurements can be found in the Appendix B.1. Figure 4.2 shows the debris thickness profiles measured along two transects that traverse the five distinct flow units of the study area (Figure 3.3) on top of the glacier topography.

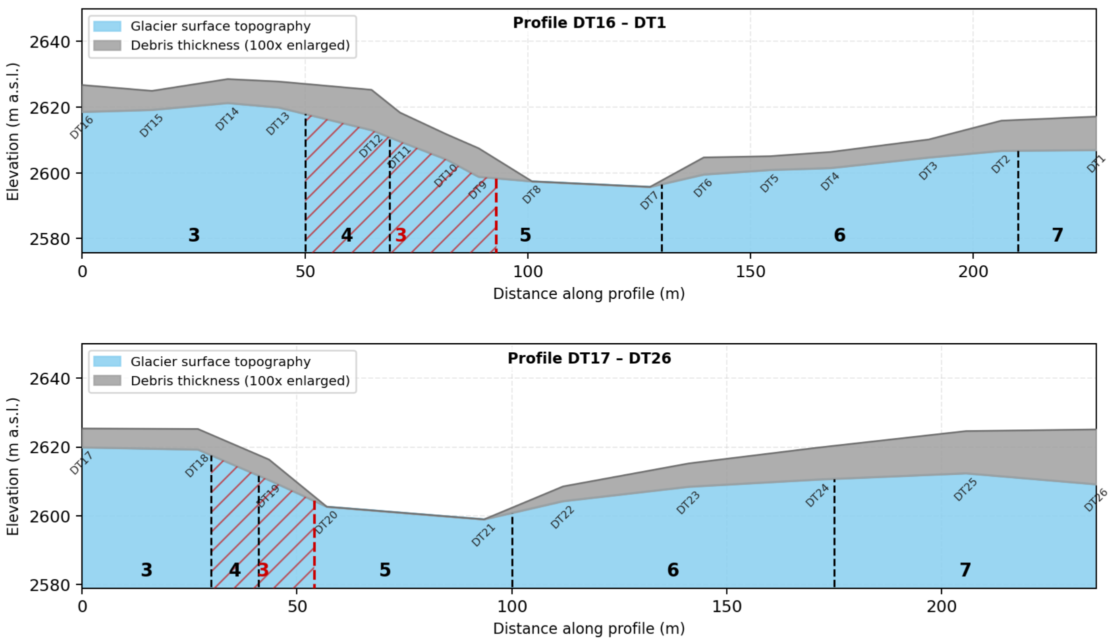

Figure 4.2: Debris cover thickness profiles along two cross glacier transects through the study area (upper profile: DT16–DT1; lower profile: DT17–DT26). The blue area shows the glacier surface topography (m a.s.l.) and the grey area the debris cover thickness (cm, scaled by a factor of 100 for visualisation). Individual measurements are labelled along each profile. Black dashed vertical lines mark the flow unit boundaries (3–7) as defined in Section 3.2.1, with the red dashed vertical line indicating the flow unit 3 overlap shown in Figure 3.3. Full measurement data in Appendix B.1.

The debris cover thickness varies considerably between and within individual flow units, across both profiles. While flow unit 7 consistently recorded the highest values, with a maximum of 27.7 cm, flow unit 5 exhibited a patchy debris cover, where approximately 60 % of the ice surface was covered by debris. This absence of a continuous debris cover of flow unit 5 coincides with the topographic low of the glacier surface. From there the topography rises towards flow units 4 and 5 on either side of the profile, and continues on a higher level towards the margins (flow unit 3 on the left, respectively, 7 on the right).

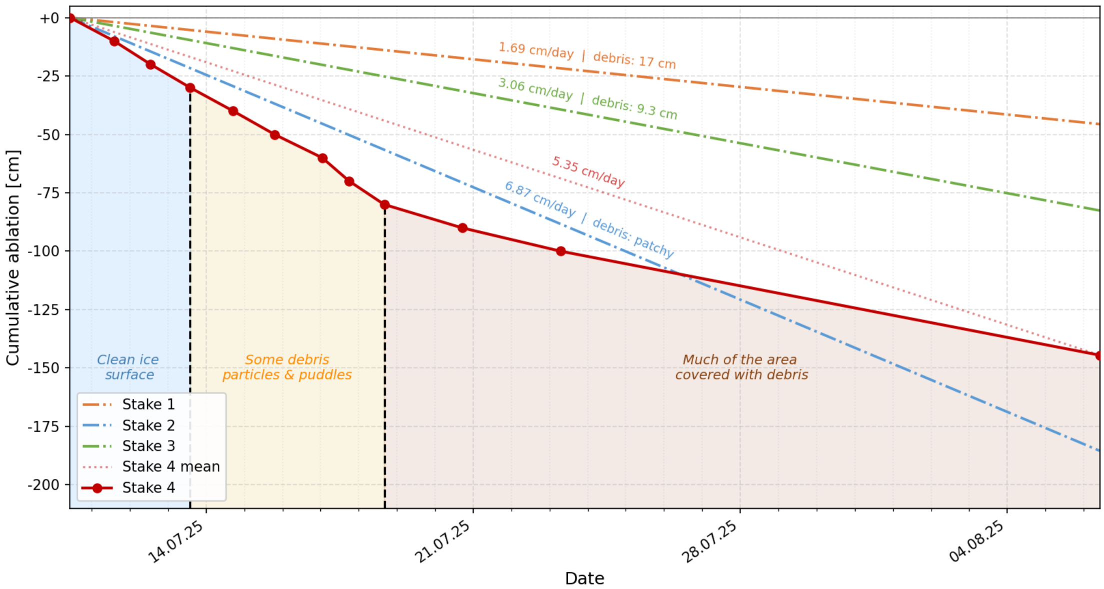

Figure 4.3: Ablation rates measured at four stakes between 10 July and 6 August. Dash-dotted and dotted lines represent the mean ablation rates for stakes 1-3, and the mean rate of stake 4, respectively. The solid red line shows the temporally resolved ablation at stake 4, derived from the wildlife camera imagery. The background shading indicates three successive surface condition phases at the melt-out plot: clean-ice (blue), surface impurities like debris particles and puddles (yellow), and partial to extensive debris coverage (red). Vertical dashed lines (black) mark the approximate transition dates between surface condition phases.

4.1.3 Ablation Measurements

The mean daily ablation rates of the three stakes placed in flow units 3 (stake 3) ,5 (stake 2) and 7 (stake 1) are shown in Figure 4.3. Ablation rates differ significantly between stakes, with the highest value recorded at stake 2 (6.87 cm/day), which exhibits a patchy surface area coverage (approximately 60 %). Stake 3, with a debris cover thickness of 9.3 cm, exhibits a lower melt rate of 3.06 cm/day, while the lowest melt rate is recorded at stake 1 (1.69 cm/day; 17 cm debris thickness).

Ablation rates at stake 4 followed a non-linear trajectory, extracted from images captured by the wildlife camera monitoring the melt-out experiment plot (Section 3.1.4). Stake 4 recorded the highest ablation rates of all stakes over the initial debris free, clean-ice phase and and the following phase, marked by the appearance and vanishing of debris particles and puddles. Once much of the surrounding area was covered with debris, after 19 July, the ablation rate at stake 4 slowed considerably, with a cumulative total ablation of 144.5 cm or a mean rate of 5.35 cm/day, respectively, recorded by early August.

Figure 4.4: Selected images of the melt-out plot showing the initial clean-ice state (top left, 7 July), cratered glacier surface (top right, 13 July), surface drainage channel (bottom left, 15 July) and the closing in of the marginal supraglacial debris (bottom right, 23 July).

4.1.4 Melt-out Experiment

A time-lapse video created using the wildlife camera imagery (available at Meier, 2026d), captured the progressive ablation of the ice surface and the re-establishment of a debris cover over the cleared plot throughout the 28-day observation period (Figure 4.4). In the initial phase (until $\sim$ 18 July), individual englacial debris particles emerged at the clean-ice surface, each locally enhancing melt in their immediate vicinity causing them to melt "into" the glacier surface, producing a cratered micro-topography across the plot. Shallow puddles and minor melt-water drainage channels appeared and disappeared intermittently on the surface, additionally shaping the glacier surface.

Strong ablation during the early observation period (until $\sim$ 18 July) caused rapid surface lowering of the clean-ice surface, which progressively steepened the slope between the cleared plot and the surrounding debris-covered glacier surface. This caused the supraglacial debris from the plot margins to slowly creep towards the ablation stake at the center of the plot. Over the course of the study period, the majority of the originally cleared area had been re-buried by the creeping debris from the margins.

Toward the end of the observation period (from 21 July onward), the large boulder serving as mounting for the wildlife camera shifted, causing a displacement of the camera's field of view. This hinders accurate ablation readings and observation of the remaining glacier surface around the central stake for the final portion of the observation period.

4.2 Modelling Results

This Section gives an overview of the results of the debrisIGM module experiment run, applying the specified climatic forcing along with the additional input parameters defined in Section 3.3.7.

4.2.1 Reproduction of Zmuttgletscher - Past and Present

During the initial spin-up period (model time steps 1000–1600) with the ELA held steady at 3150 m a.s.l., the glacier reached a steady state, where the Schönbiel- and Tiefmattengletscher tributaries had not yet merged to form the main Zmuttgletscher tongue. In response to the sudden ELA reduction of 150 m (to 3000 m a.s.l.) at time step 1600, representing the onset of the pronounced cooling phase of the LIA, the modelled glacier started to advance rapidly. The maximum glacier extent was reached approximately 40 time steps after the end of the LIA cooling phase at time step 1890. From 1850 onward, the ELA started to increase by 1.75 m per year up to 3350 m a.s.l. at time step 2050, as a response to the anthropogenic warming. From time step 1890 onward, the glacier starts a pronounced downwasting phase ($\sim$ 1850–1950), followed by a dramatic retreat until the end of the model run at time step 2050. A video of the ice thickness evolution, used to illustrate the glacier extent discussed in this section, is available at Meier (2026a).

Figure 4.5 displays the modelled ice thickness at three selected time steps (1880, 1890, and 1900), capturing the period of maximum glacier extent. At these time steps, the modelled glacier tongue closely matches the mapped LIA moraine positions of the Zmuttgletscher defined in Section 3.2.3. This suggests that the debrisIGM module, given the input parameters specified in Table 3.2, reliably reproduces the maximum glacier advance during the LIA cooling period, supporting the use of the model results for further analysis.

As shown in Figure 4.5 as well as the supplementary Figure A.1, the tongue remained near its maximum extent for roughly 100 time steps, between 1850 and 1950. Such a prolonged period of stability at maximum extent would have provided the conditions necessary for the build-up of the prominent lateral and terminal moraines observable today, lending further confidence to the model outputs. During this same period, the glacier experienced pronounced downwasting across the whole ablation area, accompanied by the retreat of smaller tributaries and a corresponding reduction in total ice-covered area.

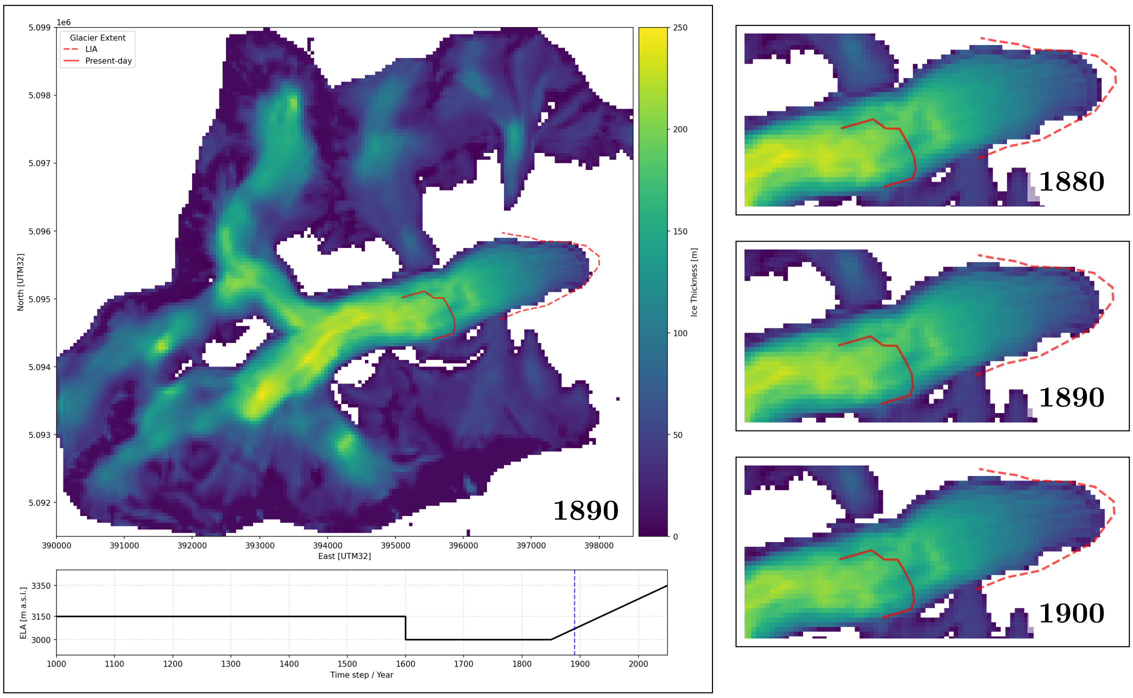

Figure 4.5: Modelled ice thickness (color scale) at time step 1890 illustrating the glacier extent at its simulated maximum (left). The lower panel shows the prescribed Equilibrium Line Altitude (ELA) forcing, with the dashed blue vertical line marking 1890. The three panels on the right provide close-ups of the glacier tongue at time steps 1880 (top), 1890 (middle) and 1900 (bottom), which closely reproduce the Little Ice Age (LIA) maximum (dashed red line); the present-day extent is shown for reference (solid red line).

Following the downwasting phase (1850–1950), the glacier began to retreat rapidly under the applied warming scenario, which raises the ELA by 1.75 m per year (Section 3.3.8). While the model accurately reproduced the LIA glacier extent, the applied warming caused the modelled glacier to decline much more rapidly than the real Zmuttgletscher. By time step 2010 the entire main tongue of the modelled glacier had disappeared, leaving only the tributaries. This resulted in a significant mismatch between modelled time steps and real years, motivated the need for the definition of reference time steps that can be used to compare the in-situ measurements to the most accurate reproduction of the present-day extent.

Figure 4.6 illustrates the three model time steps that most closely represent the present-day glacier extent. Of these, time step 1980 (Figure 4.6, middle) best captures the current glacier state, accurately reproducing the extent of the tongue, while exhibiting fragmented but still connected residual ice in front of the tongue. Time step 1970 (Figure 4.6, top right) clearly overshoots the present-day extent, with the glacier tongue positioned roughly midway between the LIA maximum and today's position. Time step 1990 (Figure 4.6, bottom right), on the other hand, falls slightly short of the present-day extent, while still showing a small amount of residual ice. Given the 10-year model snapshot resolution, the best present-day equivalent likely falls somewhere between these time steps. All three time step outputs are therefore carried forward for comparison with the in-situ measurements from the field campaign (Section 4.1).

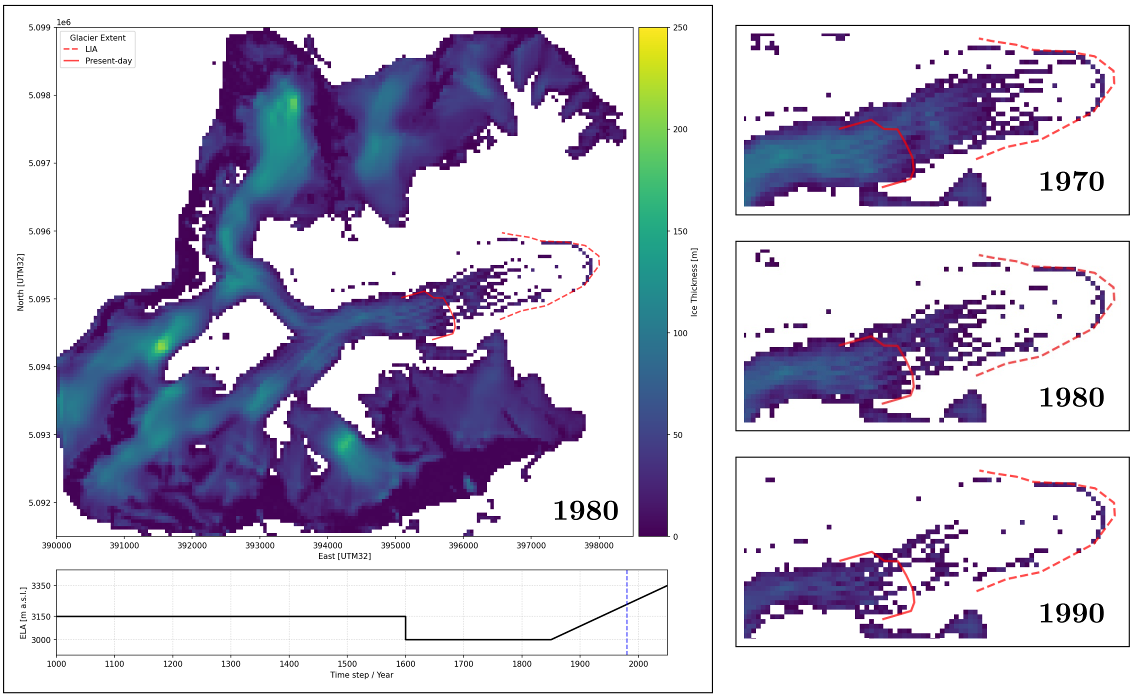

Figure 4.6: Modelled ice thickness (color scale) at time step 1980 (left), the snapshot that best represents the present-day extent (solid red line). The lower panel shows the prescribed Equilibrium Line Altitude (ELA) forcing, with the dashed blue vertical line marking 1980. The three panels on the right provide close-ups of the glacier tongue at time steps 1970 (top), 1980 (middle) and 1990 (bottom). The Little Ice Age (LIA) maximum (dashed red line) is shown for reference (solid red line).

4.2.2 Englacial Debris Concentration Evolution

Figure 4.7 shows the evolution of englacial debris concentrations throughout the simulation, at all sites (1–8) where both the BS and CS sampling methods were applied. The englacial debris concentration calculations described in Section 3.3.5, concentrations were computed within a 25 m radius across three relative height bands: the full ice column ($r \in [0, 0.99]$), the top 20 % ($r \in [0.8, 0.99]$), and the uppermost 10 % ($r \in [0.9, 0.99]$).

The concentration of modelled englacial debris varied considerably between all sites and over time (Figure 4.7). Across all sites, concentrations generally remained low (< 0.06 vol.%) throughout most of the simulation period, with values in a range similar to the in-situ measurements (Section 4.1.1). At all sites, the full ice column (blue) produced the highest and most variable concentrations, while the two surface bands generally yielded very low values (< 0.01). This indicates a strong vertical distribution of the englacial debris, concentrating in the lower ($r < 0.8$) ice column. A table containing the exact modelled englacial debris concentration values for the reference time steps 1970, 1980, and 1990 per sampling site is attached in Appendix B.2.

The ice thickness curve, which is a reflection of the climatic forcing, divides the plots into three phases: relatively constant ice thickness (time steps 1500–1600) marking the end of the spin-up phase, followed by a rapid increase and sustained high ice thickness (1600–1850), representing the LIA cooling phase, and finally a rapid decline in thickness (1850–2050) driven by the applied warming and the resulting glacier retreat. The plots do not include more of the spin up phase as it not physically meaningful.

Sites belonging to flow unit 3 (sites 3 and 4) show an increase of the englacial debris concentrations at the beginning of the LIA cooling phase, throughout which they remain comparatively high and variable. With the onset of the warming phase, coinciding with the ice thickness reduction and the debris cover increases, the concentrations first show pronounced increases (especially at site 3), before rapidly declining towards zero. At the reference time steps, the modelled concentrations of all bands are zero (Table B.2), an thus far below most in-situ measurements (BS: 0.0160 and 0.0414 vol.%,; CS: 0.0382 vol.%), with only site 4 (CS) agreeing at zero vol.%.

The full ice column concentrations (blue) of sites 2 and 5 (flow unit 5) show a similar increase at the beginning of the LIA reaching levels of up to 0.030 vol.%, before declining to zero, at the reference time steps. The upper bands, however stick close to the x-axis (zero vol.%) with occasional elevated peaks (< 0.010 vol.%). At

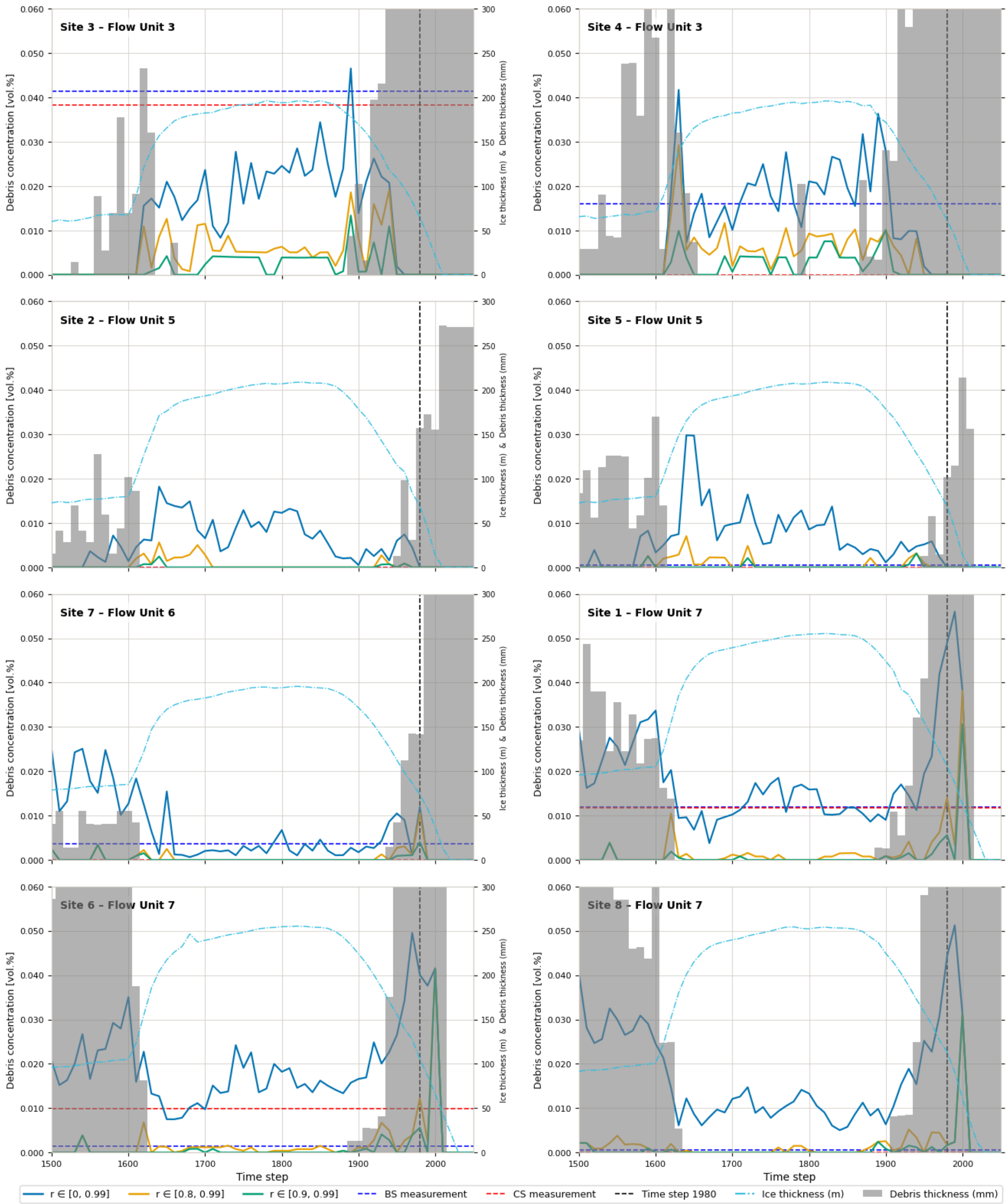

Figure 4.7: Modelled englacial debris concentration (vol.%) over time (1500–2050) for all sites where both sampling methods where applied (sites 1–8). Colored lines show the debris concentration within radii of 10 m (blue), 25 m (orange) and 50 m (green) around each site. The horizontal dashed lines indicate the measured debris concentrations applying the Block Sampling (BS, blue) and Core Sampling (CS, red) methodology. The vertical black dashed line marks the time step 1980, the cyan dash-dot line and grey bars on the right axis show the modelled ice thickness (m) and debris thickness (cm), respectively.

reference time step 1970, the full ice column concentrations (0.002 vol.% at site 5 and 0.005 vol.% at site 2) reported similar values as the in-situ measurement at site 5 (0.005 vol.% (BS)). All other concentrations are zero (Table B.2).

The single site in flow unit 6 (site 7) generally displays concentrations below the BS in-situ measurement of 0.0036 vol.%, with the full ice column values occasionally exceeding them. After the end of the LIA cooling phase ($\sim$ 1920) concentrations across all bands start to increase before peaking (0.012 vol.% (full ice column), 0.011 vol.% (top 20 %) and 0.004 vol.% (top 10 %)) at reference time step 1980, before diminishing to zero right after (Table B.2).

Flow unit 7 (sites 1, 6, and 8) shows the highest full ice column concentrations across all sites, reaching up to 0.055 vol.% (site 1). In contrast, the upper bands generally show very low values ($<$ 0.010 vol.%) throughout the LIA cooling phase, before starting to peak at multiple time steps during the warming phase. At the reference time steps, concentrations of site 1 exhibit a peak with 0.056 vol.% for the full ice column, 0.014 vol.% for the top 20 % and 0.006 vol.% for the uppermost band (Table B.2). With 0.0118 vol.% (BS) and 0.0119 vol.% (CS), the in-situ values compare well to the concentrations shown for the $r \in [0.8, 0.99]$ band. Site 6 shows similar modelled concentrations (0.050 vol.% (full ice column), 0.012 vol.% ($r \in [0.8, 0.99]$) and 0.006 vol.% f$r \in [0.9, 0.99]$; Table B.2), while in-situ measurements are a bit lower at 0.0099 (CS) and 0.0015 vol.% (BS). At site 8, where in-situ measurements showed no more than 0.0005 vol.%, modelled values of the upper bands showed similar values (0–0.004 vol.%), while the full ice column peaked at 0.051 vol.% (Table B.2).

Debris cover is absent across all sites throughout the LIA cooling phase (1600–1850), with an exception for site 4, which briefly showed a debris cover ($\sim$1780). At most sites, debris covers start to rise during the warming phase after the LIA around time step 1900 depending on the site. Significant debris cover increases typically coincide with preceeding englacial debris concentration increases, followed by major declines.

4.2.3 Englacial Debris Concentration Distribution

Figures 4.8, A.2 and A.3 present the spatial distribution of modelled englacial debris concentrations for the reference time steps. Each figure shows both the model-calculated debris concentration integrated over the full ice column and concentrations computed using the approach described in Section 3.3.5 for three relative height bands (r$\in [0, 0.99]$, $[0.8, 0.99]$, $[0.9, 0.99]$), providing a vertically resolved view of the distribution across the glacier.

Taking a closer look at time step 1970 (Figure 4.8), the modelled concentrations vary considerably across the study area and over time, ranging from zero (white) to more than 10^{-1} vol.% (yellow). Spatial heterogeneity is pronounced, with neighbouring cells often differing by an order of magnitude. Nevertheless, several clear patterns emerge.

Considering the full ice column (both the model output (top left) and r∈ $[0, 0.99]$ (top right)), a band of elevated concentrations follows the boundary between flow units 6 and 7. To the north, concentrations decrease markedly within flow units 4 and 5, before either vanishing or rising again towards flow units 3 and 2. to the south, concentrations decline towards the boundary of flow unit 8, before they increase once again.

The $r \in [0.8, 0.99]$ band broadly reproduces the spatial pattern of the full-column concentrations, though values across flow units 4 and 5 largely drop to zero while those in flow units 2, 3, 6, 7, and 8 increase. The upper band ($r \in [0.9, 0.99]$) shows a markedly different picture, with values almost exclusively exceed 10^{-2} vol.%, many close to or above 10^{-1} vol.%. Flow units 2–5 contain few non-zero cells, and those that do appear are generally higher in units 2 and 3 than in 4 and 5.

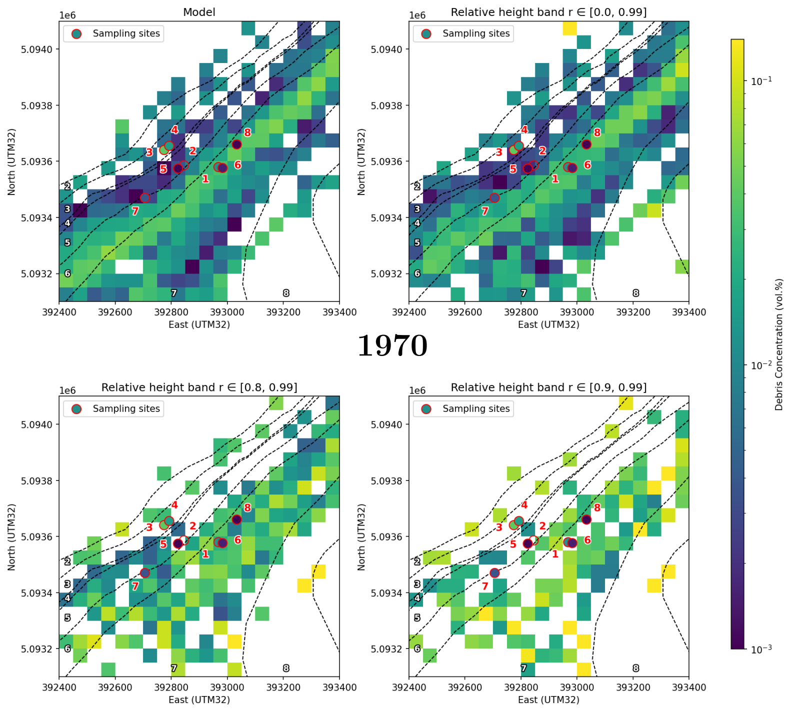

Figure 4.8: Modelled debris concentration (vol.%) of time step 1970, shown for the full ice columns (model output, top left) and three relative height bands (r∈ $[0, 0.99], [0.8, 0.99], [0.9, 0.99]$. Dashed lines indicate the flow unit (white numbers) boundaries. Colored circles show the measured debris concentrations at sampling sites (red numbers). The color scale is logarithmic.

As noted in Section 4.2.2, the measured debris concentrations (colored circles with red outline; BS sampling method) fall within a similar range to the modelled concentrations. Sampling sites 1, 2, 5, and 7 show broad agreement with the modelled values across all panels. Measurements of sites 3 and 4 exceed the values of their surrounding cells in the full-column plots (top row), whereas sites 6 and 8 show the opposite pattern, with measured values markedly lower than those of the surrounding cells. The fragmented distribution of the upper bands, with many zero-valued cells, helps to explain the erratic behaviour of the evolution curves in Section 4.2.2. Because the grid cell calculation produces sharp boundaries, values can change abruptly between neighbouring cells or across time, depending on where the debris particles are located. Agreement with the underlying grid cell is therefore not always given, although surrounding cells may exhibit similar values.

Time step 1980 (Figure A.2 shows broadly similar agreement between the in-situ measurements and the modelled values. Compared to 1970, fewer cells carry concentrations exceeding zero (white), while the spatial pattern remains comparable, with elevated values along the border between flow unit 6 and 7, and lower values on either side.

By time step 1990, most cells show modelled concentrations of zero (white), with only a narrow band along the flow unit 6–7 boundary and the up-glacier area (towards the axis origin) retaining elevated values. Measurements of sites 1, 2, and 5 generally agree with the surrounding modelled concentrations, whereas sites 6 and 8 agree only with the upper band values. Across all panels, the modelled values around sites 3 and 4 remain at zero.

Across all three reference time steps, the modelled englacial debris concentrations display consistent large scale spatial patterns, despite pronounced cell-to-cell heterogeneity. Elevated concentrations persistently emerge around the boundary between flow unit 6 and 7. The upper height bands show much more fragmented patterns, where neighbouring cells often differ by orders of magnitude. The concentration of non zero values within flow units 6 and 7 indicates that in these flow units the debris is accumulated near the glacier surface.

4.2.4 Debris Thickness Patterns

Figure 4.9 displays the modelled debris cover thickness at reference time steps 1970, 1980, and 1990. The spatial patterns are consistent across all time steps, with low values in flow unit 4 and 5, and increasing towards both the north (flow units 3 and 2) and south (flow units 6 and 7).

Although most in-situ measurements (diamonds) report higher debris thicknesses than the model, they show broad agreement ($\sim 5\,\text{cm}$) with modelled spatial pattern. The main exception are the measurements located in flow unit 5, which exhibit markedly higher values compared to the modelled values in the background.

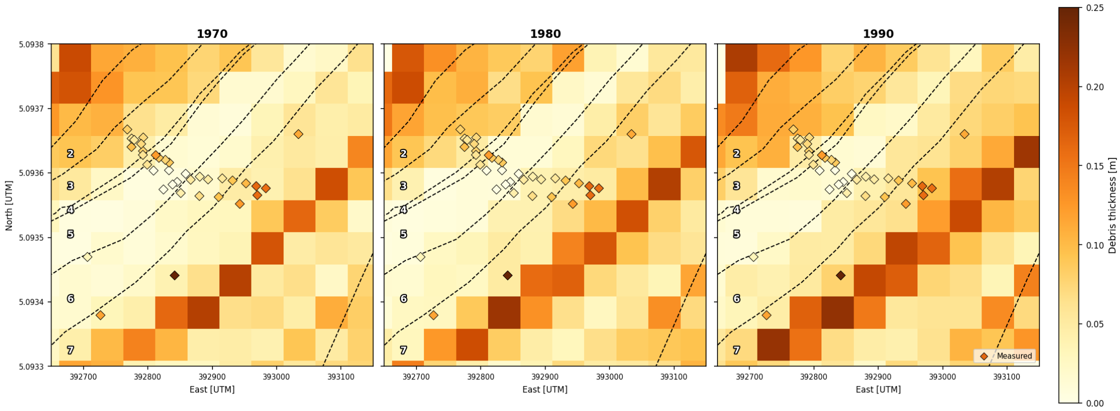

Figure 4.9: Modelled debris cover thickness (m) of time steps 1970, 1980 and 1990. Dashed lines indicate the flow unit (black numbers) boundaries. Colored diamonds show the measured debris thickness.

This discrepancy may be explained by the debris cover overlap of flow unit 3, encountered during the field work, as shown in Figures 4.2 and 3.3. Although measured debris thicknesses are consistently higher than the modelled values at the corresponding grid cell neighbouring cells often show comparable values.

The modelled evolution of the debris thickness over time for sites 1–8, has already been discussed in Section 4.2.2 and can can be seen in Figure 4.7.

The spatial patterns of debris cover thickness are comparable to those of the englacial debris concentrations described in Section 4.2.6. Flow units with low englacial debris concentrations (4 and 5) generally coincide with thinner debris covers, whereas those with higher concentrations (6, and 7) show correspondingly thicker debris covers. At flow units 3 and 4, where only isolated elevated concentrations were found among zero-valued cells, nonetheless show pronounced debris cover thickness ($> 10\,\text{cm}$).

4.2.5 Supraglacial Debris Patterns

Building on the local measurement comparisons presented above, this Section examines the broader spatial evolution of the modelled supraglacial debris. Particles are tracked according to the source areas defined in Section 3.2.2, under the premise that the distinct catchment characteristics of each source area should produce an identifiable flow unit in the ablation area (Section 3.2.1). To this end, every particle is colored by its source area throughout the simulation. A video of the full simulation, showing all surface particles ($r = 1$) colored by source area ID, is available at Meier (2026b). One overview snapshot (Figure 4.10) and four close-ups of representative time steps (Figure 4.11) are reproduced here to illustrate the temporal evolution.

In the following, flow units derived from the modelled and colored particles are referred to as **source units** to distinguish them clearly from the mapped flow units. Additionally, an important distinction must be drawn between debris cover (thickness) and the particle distributions shown below. The presence and density of colored particles on the surface does not translate directly into debris cover thickness, since this also depends on the volume assigned to each particle. The absence of particles however, can reliably be interpreted as the absence of supraglacial debris.

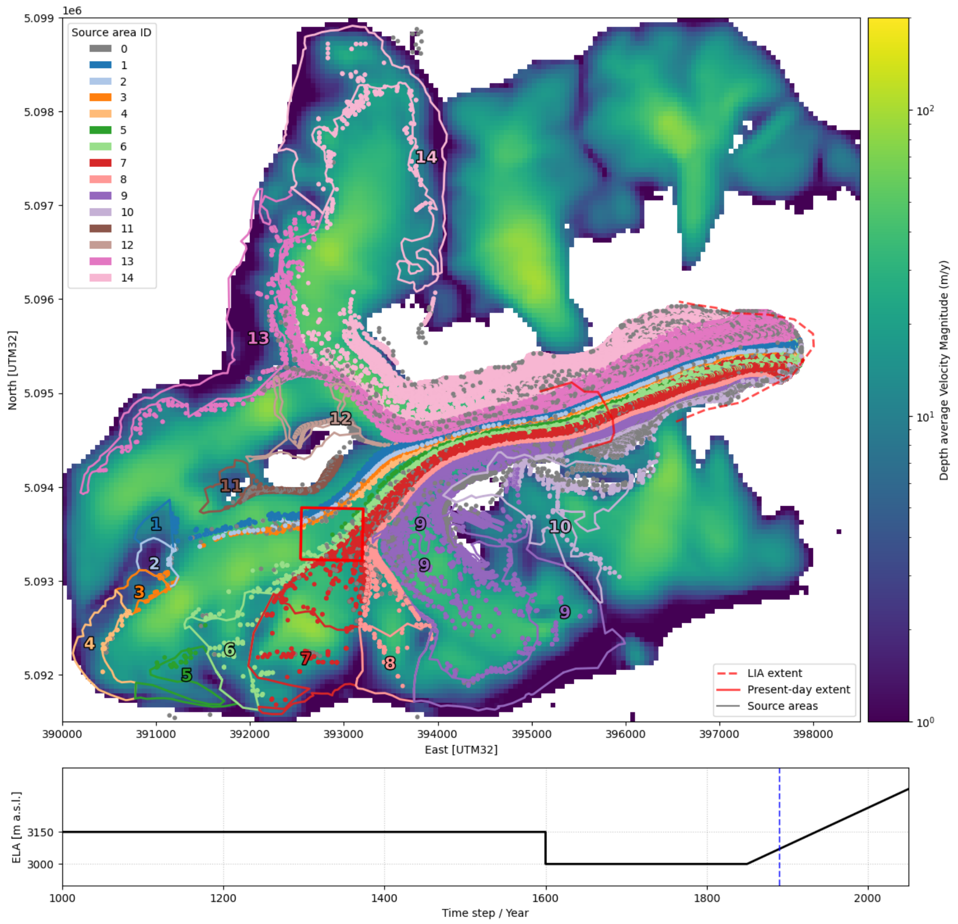

Figure 4.10: Modelled depth averaged velocity magnitude (m/y) at time step 1890 overlaid by all supraglacial ($r = 1$) debris particles colored according to their source area (polygons 1–14, 0 (grey): deposited particles). The present-day (solid) and Little Ice Age (LIA, dashed) glacier extent as well as the study area (box) are added as reference in red. The lower panel shows the prescribed Equilibrium Line Altitude (ELA) forcing, with the dashed blue vertical line marking the year 1890.

Figure 4.10 shows the modelled supraglacial debris distribution at time step 1890, when the glacier reached its maximum simulated extent. All source units originating from the Tiefmattengletscher tributary (1–9) converge at roughly the height of the study area to form organised, parallel bands that extend from their headwall sources through the study area down to the tongue. At this stage, some overlap with neighbouring units and remobilized particles (grey) is visible, yet individual source area units remain clearly identifiable. Source unit 10 (light violet) enters the main glacier tongue at a later stage, but integrates cleanly into the organised parallel bands. Source units 11 and 12 (light and dark brown), originating on the slopes of the Stockji peak (Figure 3.5) and flanked by the Stockjigletscher tributary from the north and south, yield few surface particles, with neither trace extending to the front of the tongue. By contrast, the northern branch of the Stockjigletscher together with the Schönbielgletscher tributary carry a large numbers of supraglacial particles from sources 13 (dark pink) and 14 (light pink) to the northern margin of the main tongue. Deposited onto both tributaries, the source 13 particles converge with the ice flow, to form a supraglacial debris band resembling the structure of a medial moraine. Its position coincides with a medial moraine mapped on both the Siegfried and Dufour maps (Swisstopo, 2026).

While much of the glacier carries some debris particles, several areas show none. The region west of the study area up to source areas 4 and 5, shows an absence of particles from those sources, which only re-emerge further down-glacier. A similar pattern is shown for Schönbielgletscher, where a large area between the deposited particles at the bottom of the steep headwalls and their re-emergence at the location of confluence with Stockjigletscher remains particle free. The Stockjigletscher itself shows only few marginal particles, with the centers of both branches showing a complete absence of supraglacial particles.

The evolution of the supraglacial debris distribution around the study area, in comparison to the mapped flow units, is examined in more detail in Figure 4.11. At the end of the LIA cooling phase (Figure 4.11, top left), source units 1, 2, and 3 form continuous traces across the study area that do not match the mapped flow units up-glacier (west), but broadly align with them further down glacier (east). Particles from source areas 4 and 5 first appear down-glacier of the study area, leaving a large part of the study area free of any supraglacial debris. Source units 6 and 7 form organized units, clearly traceable along the glacier, that strongly disagree with the mapped flow units, which are located further to the north. Source units 8 and 9 show better agreement with their respective mapped flow units, broadly matching them in position. Source unit 8, however, is markedly narrower than its mapped counterpart. Although some supraglacial particles are visible, Figure 4.7 did not show a debris cover at that time step.

By time step 1930 (Figure 4.11, top right), the study area shows a pronounced increase in the number of supraglacial particles, while the glacier tongue remains close to its maximum extent (Figure A.1). This increase is caused by the downwasting effect mentioned in Section 4.2.1, where enhanced surface melt in this segment of the glacier exposes large numbers of englacial particles. Source units 1, 2, and 3 have all expanded in width and shifted a slightly northward, into the area formerly occupied by the particle-free retreating branch of the Stockjigletscher, resulting in a significant mismatch with their mapped flow units. Source unit 4 has expanded markedly, forming a debris unit considerably wider than the mapped flow unit 4, while particles of source area 5 start to appear within the study area. Source units 6–9 show a substantial increase in the number of particles, with little other change. Figure 4.7 did not show a debris cover for flow units 5 and 6, while all other sites exhibited a debris cover of some form.

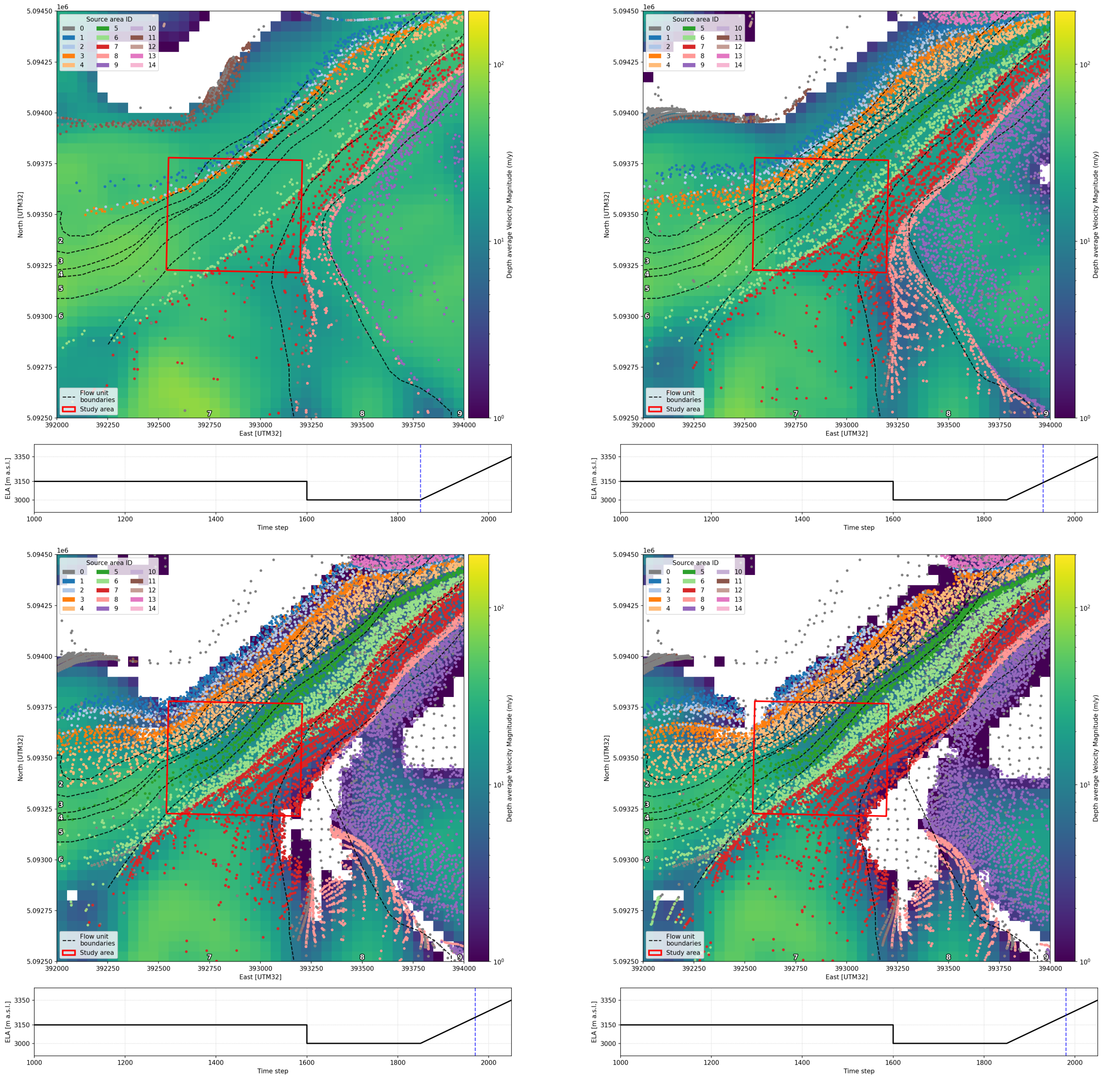

Figure 4.11: Evolution of the modelled supraglacial debris particles around the study area (red) at four representative time steps. Debris particles ($r = 1$) are colored by source area, flow units are delineated with dashed black lines and labeled with white numbers. The depth averaged velocity magnitude (m/y) is shown in the back. The lower panels show the prescribed Equilibrium Line Altitude (ELA) forcing, with the dashed blue vertical line marking the displayed year.

Time step 1970 (Figure 4.11, bottom left) shows another substantial increase in particles compared to the previous time steps. Source units 1–3, still positioned to the north of their respective flow units, now reach the glacier margin and begin to form deposited particles (grey). Source units 4 and 5 cover considerably more area than their mapped flow units and partially overlap within the study area. Source units 6 and 7 placed to far south of their respective flow units, show a pronounced overlap within the study area, with particles also appearing together in their source areas themselves (just above the lower legend). Source units 8 and 9 are affected by the ongoing glacier retreat, that slowly detaches them from the main tongue.

The Present-day reference time step 1980 (Figure 4.11, bottom right) shows particle distribution similar to that of time step 1970, while showing an important difference. The glacier arm that supplies the particles of sources 1, 2, and parts of 3 (top left corner of the study site) has detached from the main tongue, causing these source units to terminate further down-glacier and to be deposited off-glacier. This disconnection resembles the observed present-day flow unit termini observed at the same location east of the Stockji, just before the confluence with the Schönbielgletscher, visible in Figure 3.4.

4.2.6 Englacial Debris Patterns

Similarly to the Section above, this Section examines the broader spatial evolution of the vertical distribution of the modelled supraglacial debris particles across ten profiles positioned along the glacier from top (1) to bottom (10) (Figure 3.5). Particles are colored by their source area and displayed according to their relative height (r) within the ice column, where a particle with $r = 0$ sits at the glacier bed and $r = 1$ is a supraglacial particle. A video showing the evolution at all transects over the full simulation is available at Meier (2026c).

As already shown in Section 4.2.5 the spatial distribution is mainly driven by the ELA forcing, producing variable patterns over time. The vertical resolution across the transects, still shows some clear spatial patterns (Figure 4.12).

Transects placed further up-glacier (1 and 2) generally show particles at greater depths reflecting the entrainment of supraglacially deposited debris into the ice column in the accumulation area. Intermediary transects (3–6, depending on the time step) show the particles distributed across much of the ice column, generally positioned slightly higher than in the accumulation area, with some supraglacial particles emerging at the surface. Lower transects (7–10) show a similar distribution across the entire ice column while showing a substantial amount surface particles ($r = 1$). All transects generally show organized, clearly distinguishable source units (hulls around the individual particles per source ID), except for source units 5–7

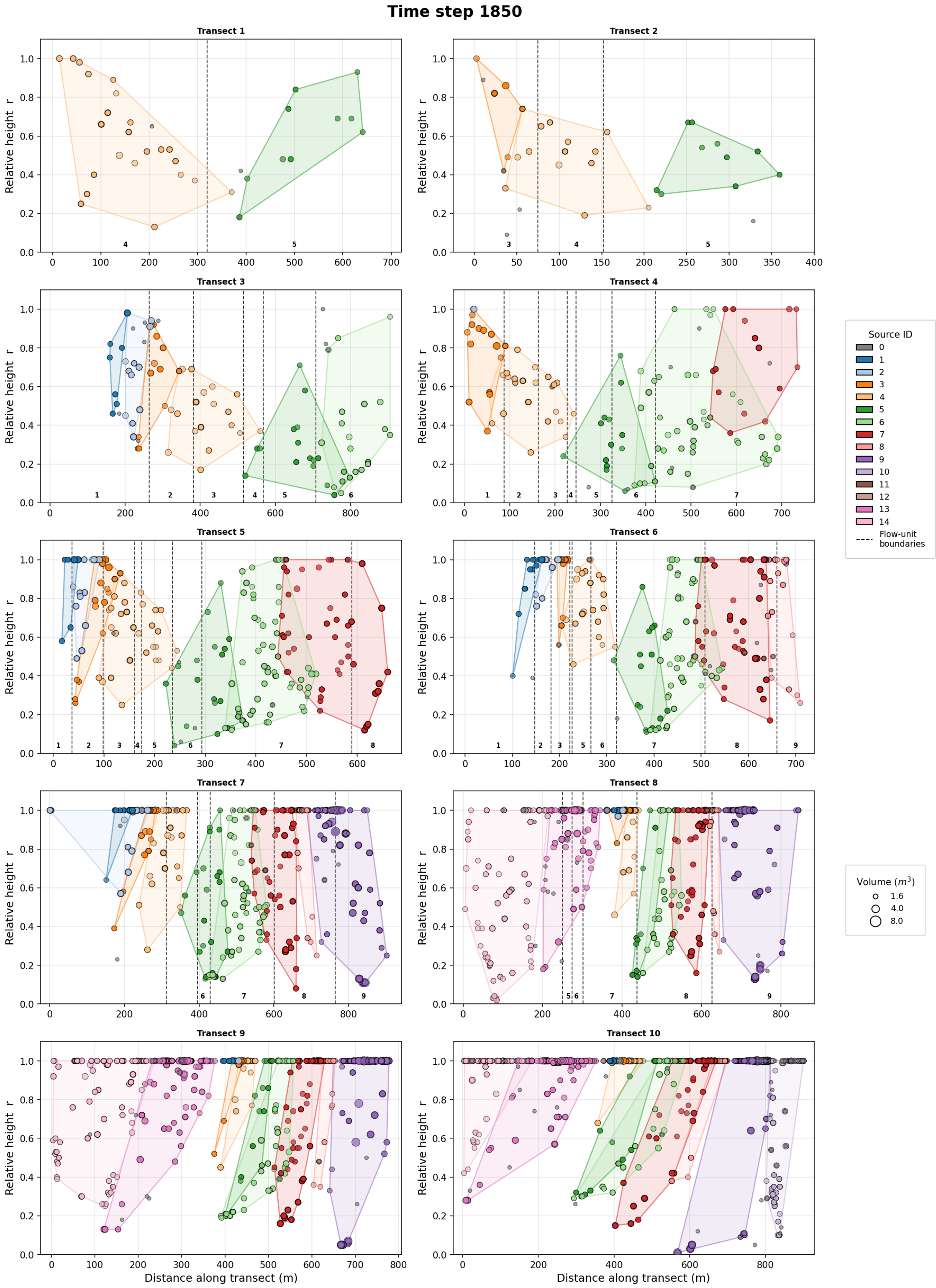

Figure 4.12: Vertical debris distribution across ten cross glacier transects at time step 1850, displaying the relative height (r) of particles within 25 m of the transect, colored by source area (1–14) and scaled by volume (m^3). Grey particles (ID=) represent aggregated debris displayed at fixed 1 m^3 volume to improve visibility. Vertical dashed lines indicate the mapped flow units (numbered at the x-axis).

which overlap across all the transects where they appear. Broad agreement with the mapped flow units occurs across all transects, though individual transects and time steps may differ significantly.

The vertical distribution shows a strong dependence on the ELA evolution. The ELA decrease during the LIA cooling phase (1600–1850) causes particles across all transects to be transported at deeper levels within the ice columns and shifts substantial supraglacial aggregations further down-glacier. The subsequent warming phase, triggers substantial down wasting, elevating particles within the ice column and creating substantial supraglacial particle aggregations far up-glacier.

Throughout the simulation particles show highly variable distribution states while maintaining relatively well organized debris units. Agreement with the mapped flow units, varies strongly between transects and with time.

The results of transect 5, spanning across the study area (Figure 3.5), are presented in more detail below.

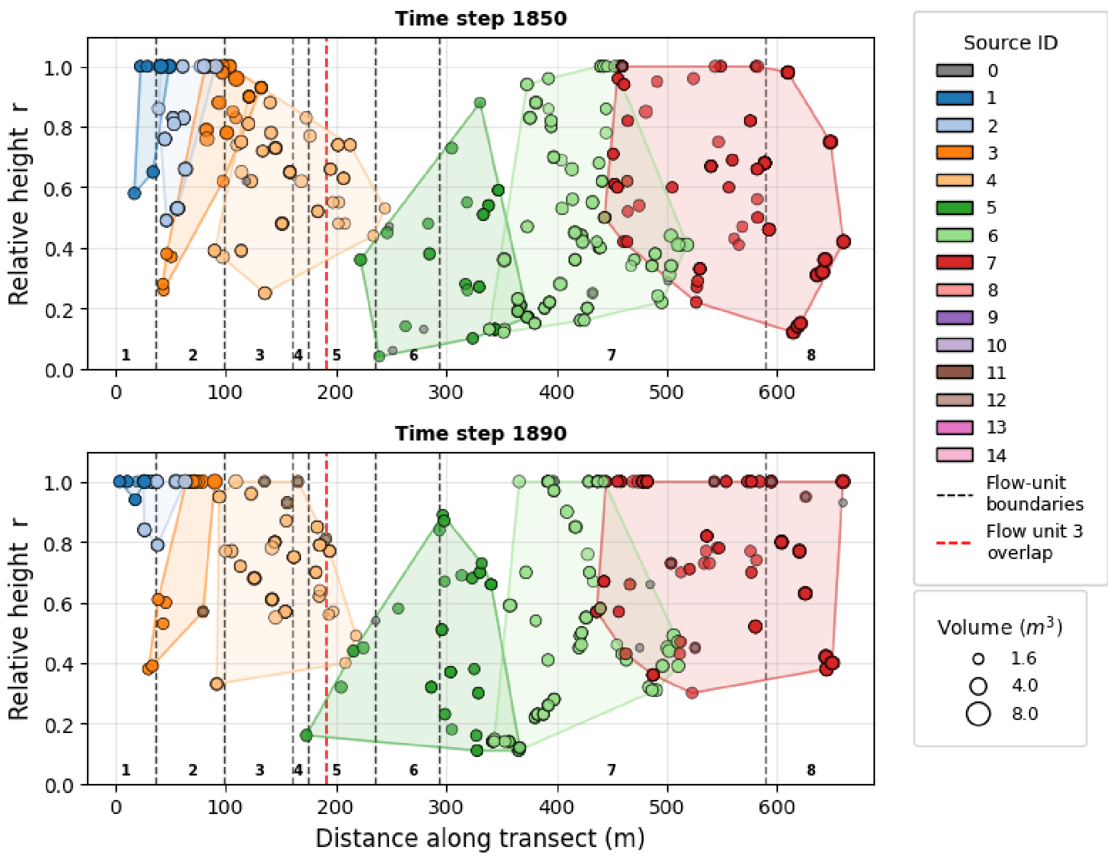

Figure 4.13: Vertical debris distribution across transect 5 at time steps 1850 (top) and 1890 (bottom), displaying the relative height (r) of particles within 25 m of the transect, colored by source area (1–14) and scaled by volume (m^3). Grey particles (ID 0) represent aggregated debris displayed at fixed 1 m^3 volume to improve visibility. Vertical dashed lines indicate the mapped flow units (numbered at the x-axis).

At time step 1850 (Figure 4.13, top), marking the end of the LIA cooling phase, particles are distributed throughout the entire ice column, with most particles positioned below the surface. The particles from source units 1 and 2 at the northern transect end (left) predominantly occupy the upper ice column ($r \geq 0.6$), with some at the surface. Source unit 3 similarly shows upper ice column positioning, except for some deeply entrained particles ($r \approx 0.3$). Above source units 4 and 5, the ice surface remains particle-free, while beneath they span nearly the entire ice column ($r \in [0.1, 0.9]$). Source units 6 and 7 show similar vertical spread with some surface particles. Source unit 6 clearly overlaps with both neighbouring source units (5 and 7) particularly in deeper ice layers ($r \in [0.1, 0.5]$).

Agreement with the mapped flow units is moderate: source units 1–3 align reasonably well with their respective flow units, while source units 4–7 extend up to 200 m (up to 4× of their mapped flow unit width) beyond their mapped boundaries. The dashed red line, indicating the flow unit 3 shows no improved agreement.

By time step 1890 (Figure 4.13, bottom), 40 time steps after the onset of warming, when the glacier reached its maximum extent, particles are positioned higher up within the ice column. Surface particles become more prominent across all source units except unit 5, which shows no surface particles. The overlap between source units 5, 6 and 7 persists, along with the continued mismatch with the mapped flow units, including the flow unit 3 overlap.

At time step 1930 (Figure 4.14, top), upward migration within the ice column, driven by significant downwasting, places a majority of particles in the upper ice column ($r \geq 0.5$). Particles from all source units now appear at the glacier surface, while maintaining a particle-free stretch between source units 4 and 5. The overlap between source units 5, 6, and 7 remains unchanged. Alignment with the mapped flow units improves slightly for source unit 7, which shifts northward (left), while the remaining units exhibit a similar fit as before.

By 1980 (Figure 4.14, bottom), the reference time step for the present-day extent, almost no englacial particles remain. Only source units 5 and 6 retain a notable englacial signatures far down in the ice column ($r \approx 0.3$).

The surface particle distribution shows a relatively organized glacier surface, with overlaps between units 5–7 persisting. Overall alignment with the mapped flow units has improved, though many source units still extend far beyond their mapped boundaries. Source unit 4 shows a significantly wider surface span than the mapped flow unit, displacing source unit 3 too far north (left). Similarly, source unit 5 displays a wide surface span, reaching over the mapped flow unit 6, placing source unit 6 completely within the boundaries of flow unit 7. Source unit 7 continues to extend towards the north, more closely representing its mapped flow unit.

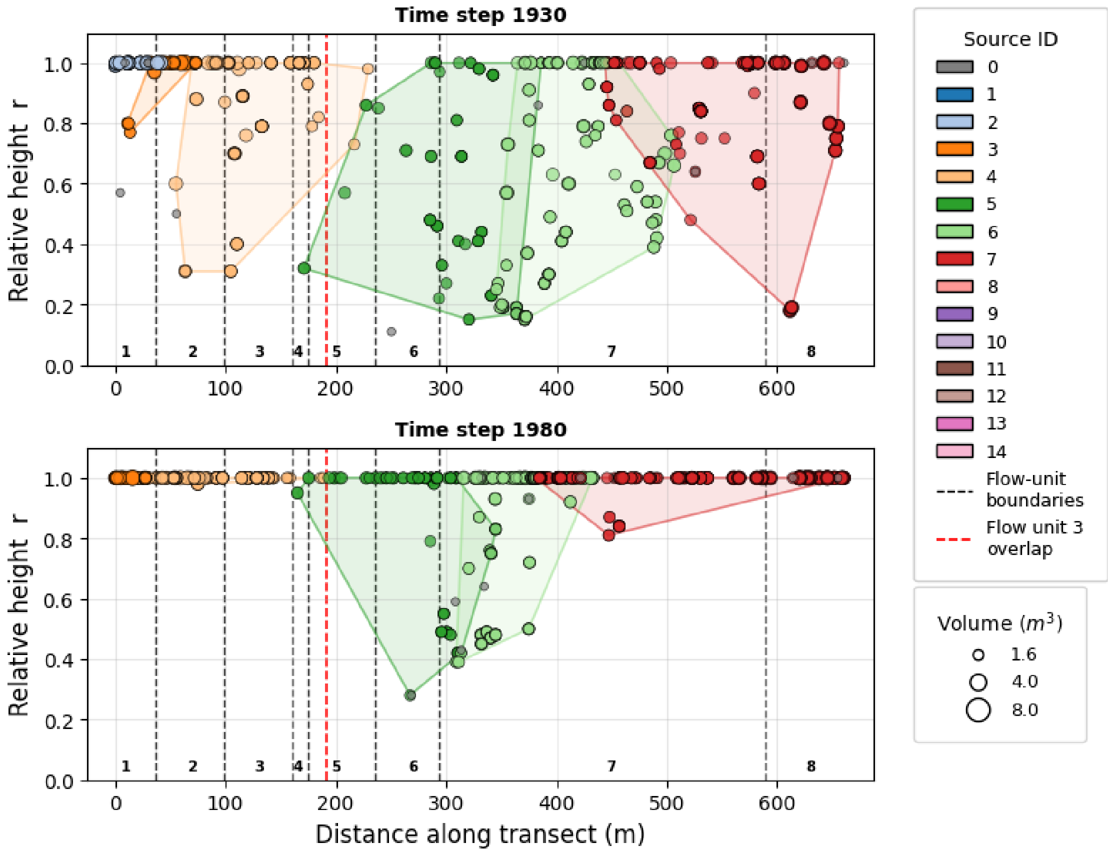

Figure 4.14: Vertical debris distribution across transect 5 at time steps 1930 (top) and 1980 (bottom), displaying the relative height (r) of particles within 25 m of the transect, colored by source area (1–14) and scaled by volume (m^3). Grey particles (ID 0) represent aggregated debris displayed at fixed 1 m^3 volume to improve visibility. Vertical dashed lines indicate the mapped flow units (numbered at the x-axis).

4.2.7 Englacial Transport Time

Figure 4.15 shows the englacial transport times of all surface particles ($r = 1$) at the time step of the maximum modelled glacier extent (1890). The distribution varies strongly within and between the 14 source areas, with the majority of particles spending less than ~ 200 time steps entrained within the ice. Mean englacial times range from roughly 30 time steps (source area 11) to approximately 125 time steps (source areas 5 and 6), with the remaining mean values falling between roughly 40 and 100 time steps. Similarly, the interquartile ranges, an indicator of the internal distribution, vary strongly between the source areas. Source area 11 produced a narrow distribution only spanning a few decades, while areas 5 and 6 yield broader distributions with IQRs spanning up to 200 time steps. Many source areas display a long trail of outliers, with individual particles reaching englacial transport times of up to 650 time steps.

The englacial time and the mean elevation of a source area (grey bars in Figure 4.15) correlate very well. Source areas 4–6 and 14 have the highest mean elevations and also produce the longest mean englacial times, while the source units 10–12 exhibit the lowest mean elevations and the shortest mean englacial times. Similarly, englacial times show a more narrow distribution for low mean elevation source areas (1,8 and 10–12) and a broader distribution for high mean elevation sources (3–5, 7, 8, 13, and 14). This suggests that the englacial transport time is strongly linked to the characteristics of the source area, namely the elevation.

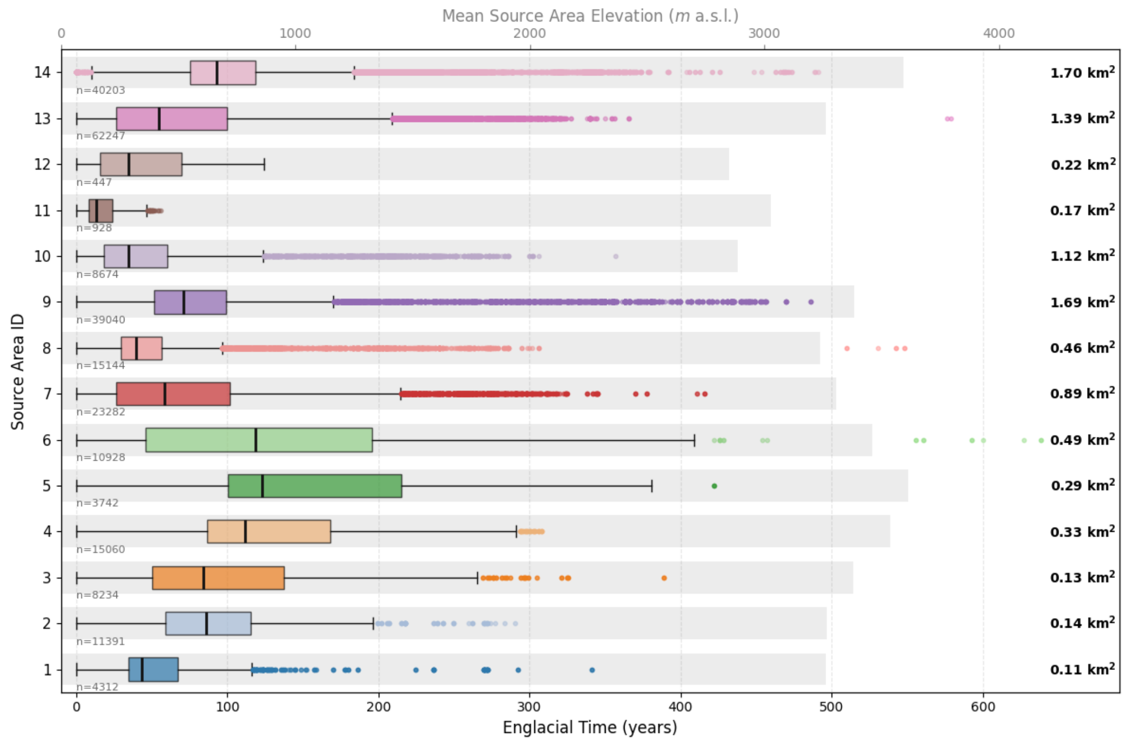

Figure 4.15: Distribution of englacial transport times (time steps) for all particles at the glacier surface ($r = 1$) at the time step of the maximum modelled glacier extent (1890), grouped by their area of origin (1–14), Boxplots show the interquartile range (IQR) with means indicated by vertical lines, whiskers extend to 1.5 × IQR, and individual outliers are plotted beyond. Light grey horizontal bars (top axis) indicate the mean elevation of source area (m a.s.l.) and the labels on the right report the source area surface extent (km^2).

5. Discussion

5.1 In-Situ Measurements

Englacial debris concentrations measured on Zmuttgletscher ($0 - 0.0414$ vol.%, Table 4.1) fall at the lower end of previously reported values at glaciers elsewhere (Table 2.1). Miles et al. (2021) reported debris concentrations of 0.1 vol.% on the Khumbu Glacier, more than double the maximum observed on Zmuttgletscher, a disparity likely driven by Khumbu's larger headwalls and more abundant debris supply. Furthermore, it is important to note that their measurements began at a depth of 2 m, whereas this study focused on surface ice. However, they agree well with concentrations from other temperate high-mountain glaciers in comparable settings, such as 0.0406 vol.% on the Djankuat Glacier, Caucasus, Russia (Bozhinskiy et al., 1986), and $0.003 - 0.005$ vol.% (dispersed debris) on the Glacier d'Estelette, Italy (Kirkbride and Deline, 2013).

The in-situ data reveal a coherent coupling between englacial debris concentration, supraglacial debris cover, and surface ablation. These covarying characteristics allowed for a clear distinction between four adjacent flow units in the study area, supporting the hypothesis that distinct source and accumulation area characteristics produce flow units that remain identifiable down-glacier (e.g. Hambrey et al., 2008; Kirkbride and Deline, 2013; Jennings et al., 2014).

A notable exception to this pattern is flow unit 3, which records the highest englacial debris concentrations of the study but not the thickset debris cover, which was reported for flow unit 7. A likely explanation is the gravitational redistribution of supraglacial debris from the flow unit 3 onto the adjacent, topographically lower flow units 4 and 5, observed in the field and , mapped as the overlap zone in Figures 3.3 and 4.2. This lateral transfer could reduce the debris cover thickness of flow unit 3 while leaving its englacial concentration unaffected, decoupling the two quantities locally.

Consistent with previous work (e.g. Östrem, 1959; Mattson et al., 1993), ablation rates decreased markedly with increasing debris cover thickness. This differential melt produced pronounced topographic contrasts between flow units. Flow unit 5, with its patchy debris cover, lowers considerably faster (6.87 cm/day) than the debris-covered neighbouring flow units (3.06 and 1.69 cm/day), forming a local topographic low along its trace. This links back to the earlier observation of supraglacial debris redistribution from flow unit 3. The melt-out experiment provides additional support for this relationship. Stake 4, placed within the cleared plot, recorded high ablation rates during the initial clean-ice phase, before the gradual re-establishment of a debris cover with debris from the plot margins, reduced melt to rates comparable to the other debris-covered stakes.

5.2 Methodological Comparison: BS vs CS

Both sampling methodologies proved feasible for determining englacial debris concentrations, yielding 8 Block Sampling (BS) and 14 Core Sampling (CS) samples over the three-day field campaign (effectively two working days). The reduced labour requirements of both methods, compared to traditional melt-out experiments (e.g. Kirkbride and Deline, 2013), enabled substantially greater spatial coverage and allowed systematic sampling across multiple flow units within a single campaign. The small scale melt-out experiment conducted alongside the BS and CS sampling campaign served as a reminder of the labour demands of the traditional approach, where extensive areas must be cleared of supraglacial debris and monitored over days to weeks (e.g. Kirkbride and Deline, 2013).

The two methods produced broadly comparable concentrations, where englacial debris was abundant but diverged systematically at low concentrations. At sites 1 and 3, where concentrations were elevated, the BS and CS values agreed closely (e.g. 0.0414 vs 0.382 vol.% at site 3). At lower concentration sites, however, BS almost consistently detected measurable debris where CS did not (Table 4.1). The most striking example is site 4, where BS returned 0.0160 vol.% while CS recorded no measurable amount of debris. This discrepancy reflects a fundamental detection-limit problem: with a sample mass of approximately 0.8 kg, CS retains too little debris at low concentrations to exceed the uncertainty introduced by filter weight variability. Zero values from CS therefore cannot be interpreted as true absence; they represent a detection threshold below which the method cannot reliably quantify debris. In this study, this bias was further reinforced, by reporting some debris sample weights as non-measurable based on visual assessment in the field.

The two methods differ substantially in their practical requirements. BS integrates over roughly 30 kg of ice per sample, increasing the statistical robustness by averaging small-scale spatial variability inherent to sparse englacial debris (Kirkbride and Deline, 2013). This volume comes at a cost: BS requires heavier equipment (chainsaw, shovels, pickaxes, and melting treys), substantially longer extraction and processing times (including the melting of large ice volume and handling of meltwater filtration), and restrictions to sampling areas within reasonable carry distance of a melting site. CS, on the contrary, uses only an ice core drill, an ice pick, and sampling bags, producing $\sim$ 0.8 kg samples that can be transported and melted in sealed sampling bags. This enables broader spatial coverage and sampling in terrain that would be impractical for BS.

These complementary strengths suggest distinct applications for the two methods. BS is better suited for obtaining robust quantitative estimates of englacial debris concentration at a limited number of representative sites, particularly where concentrations are expected to be low and statistical robustness is essential. CS is more appropriate for broader spatial surveys aimed at characterising the presence or absence of debris, or at identifying high-concentration zones, worth targeting with subsequent BS. The detection limit issue restricts CS to semi-quantitative interpretations in its current form. An improved filtration workflow would allow CS to quantify lower concentrations and would substantially expand its utility. Overall, both methods proved feasible and complementary, with a hybrid strategy likely to yield the most efficient sampling design for future research campaigns.

5.3 Evaluation of the debrisIGM Performance

5.3.1 Model Validation

It was shown that under applied ELA forcing, the debrisIGM reproduces the maximum LIA glacier extent accurately, with the modelled ice margin closely matching the mapped LIA terminal moraine positions, a common benchmark for glacier-model validation given the well-preserved moraine record (e.g. Rowan et al., 2015; Leger et al., 2025). Additional evidence of the reliability of the model stems from the coincidence of the thinning of the upper ablation area and the delayed retreat of the debris-covered tongue, a typical behaviour for debris-covered glaciers during the first few decades of warming (e.g. Ferguson and Vieli, 2021). Together, these aspects of the reconstruction lend confidence to the model's representation of the debris-covered glacier's dynamic response to climatic forcing.

The subsequent warming phase, prescribed as a 350 m ELA increase over 200 years, produces a rapid decline in which the main Zmuttgletscher tongue has largely disappeared by model time step 2010. Because the climatic forcing used here is an idealised approximation of the glacier's recent history rather than a calendar-resolved reconstruction, model time steps do not map directly onto real-world years. To align model output with observations, time steps 1970–1990, at which the modelled geometry most closely matches the present-day glacier, are used as reference states for comparison with the in-situ measurements.

Overall, the reconstruction is adequate for the interpretation of broad spatial and temporal patterns, while representation of fine-scale processes and patterns remains limited by the idealised forcing and by the specific parameter choices discussed in more detail below (Section 5.4.2). This trade-off was necessary given the scope of this project and means that this is one possible glacier evolution reconstruction of Zmuttgletscher, rather than a comprehensive sensitivity study of the debrisIGM (Hardmeier et al., 2025).

5.3.2 In-Situ Measurements vs debrisIGM Module

This study found strong overall agreement regarding the magnitude, range, and spatial patterns between in-situ measurements and the modelling results for the present-day reference time steps (1970, 1980, and 1990).

For the englacial debris concentrations, agreement is best in flow unit 7, where the modelled concentrations in the upper ice column band ($r \in [0.8, 0.99]$) at site 1 (0.014 vol.%) and site 6 (0.012 vol.%) align closely with the in-situ values (0.0118–0.0119 vol.% and 0.0015–0.0099 vol.%, respectively). Agreement is worse in flow unit 3, where the model predicts near-zero concentrations at the reference time steps while in-situ measurements returned the highest values of the campaign (0.0414 vol.% at site 3). The presence of high debris concentrations in flow unit 3, occurring approximately 40 to 90 years before the reference period, suggests that while the model exhibits a temporal offset, it may still accurately represent the underlying physical processes.

The spatial comparison of the englacial debris concentrations with their surrounding (Section 4.2.3) showed limited site-specific agreement, but meaningfully reproduced the spatial flow-unit pattern, with elevated englacial debris concentrations in flow units 6 and 7, low values across flow units 4 and 5, and increasing values again toward flow units 2 and 3. At the site level, measurements at sites 1, 2, 5, and 7 fall within the range of their immediate modelled neighbourhood, while measurements at sites 3 and 4 exceed their home-cell values and those at sites 6 and 8 fall below them. This likely results due to the finite number of particles represented in the model, the presence or absence of individual particles can abruptly shift a cell-mean concentration by an order of magnitude.

The spatial distribution maps (Figures 4.8, A.2, and A.3) highlight this sensitivity, producing sharp contrasts between adjacent cells. Restricting the analysis to the upper height bands amplifies this effect: if one or more particles are located close to the surface, the concentration rises drastically, whereas if all particles fall just outside the height band, it drops to zero. This creates a fragmented distribution in which the smaller-scale in-situ values often do not match their home cell, and a measurement falling within such a cell may diverge substantially from the home-cell value, potentially creating the false impression of a significant mismatch. It is therefore important to consider the surrounding cells when comparing with in-situ measurements. The radius-based calculation introduced in Section 3.3.5 partially addresses this grid-cell mismatch by integrating particles within a spatial buffer around each sampling site, though it remains subject to the same particle presence-or-absence sensitivity.

5.3.3 Flow Unit vs Source Unit

As discussed above, the modelled englacial debris concentrations and debris-cover thicknesses produce patterns that broadly reproduce the mapped flow units. The source area analysis extends this finding, building on the premise that individual sub-accumulation areas feed into distinct flow units down-glacier (Hambrey et al., 2008; Kirkbride and Deline, 2013; Jennings et al., 2014).

Particles coloured by source area form coherent, clearly distinguishable units that are preserved throughout transport, from their origins at the headwalls to their emergence on the glacier surface in the ablation area. This coherence holds in both the horizontal distribution across the glacier (Figures 4.10 and 4.11) and the vertical distribution within the ice column (Figure 4.12), where individual source units occupy distinct depth ranges that reflect their entrainment history.

The main exceptions to this organized pattern are the overlaps between source units 5–7. The origin of these overlaps is clearly visible in the supraglacial debris evolution video (Meier, 2026b) and in the bottom left corners of the 1970 and 1980 time steps of Figure 4.11 (around the lower legends). Throughout the simulation, particles from source area 6 appear within source area 7. This most likely results from a source area mapping error, where a part of the source area was misinterpreted. In this case, part of source area 6 is not deposited at the base of its own headwall but is instead fed into source area 7, from where it gets deposited onto the glacier. The same issue arises for the overlap between source units 5 and 6.

Considering the study area overall, a spatial mismatch between individual source units and their respective flow units can be observed, although the overall pattern represents the flow units well. Source units 4 and 5, in particular, occupy much more area than the mapped flow units 4 and 5, while the remaining source units generally appear narrower compared to their flow units.

One explanation for this mismatch is the choice of the avalanche Interval parameter. The 5-year avalanche interval used here (Section 3.3.7) leads to intermittent rather than continuous (yearly) mass input to the glacier, for source units that depend largely on avalanche-fed accumulation (source units 6–10). This seems to disproportionately affect source units 8 and 9 on the eastern Tiefmattengletscher tributary, which disconnect from the main tongue earlier than observed in reality (Section 5.3.1). This sensitivity is consistent with the findings that avalanche-fed glaciers and tributaries respond more strongly to warming than their high-accumulation counterparts (Kneib et al., 2025). This underscores the importance of accurately representing avalanche input in such systems. Source units 4 and 5, by contrast, draw from high-elevation accumulation areas with continuous mass input and therefore may be favoured to occupy more glacier area than they would under a more balanced input regime. A higher avalanche interval would likely strengthen the lateral and eastern source units and, in doing so, shift the northern source units (1–5) northward, improving their alignment with the mapped flow units.

5.3.4 Englacial Transport Time

The modelled englacial transport times reveal a strong correlation between the source area mean elevation and the duration of englacial transport. Source areas 4–6 and 14, with the highest mean elevations (< 3500m a.s.l.), produce the longest mean englacial transport times (~ 100 years), while low-elevation source areas 10-12 yield mean englacial times of only ~ 30 years. This agrees with the findings of Anderson and Anderson (2016), which state that debris deposited at high elevations, up-glacier in the accumulation area, is advected to greater depths, where it follows long transport paths through much of the glacier, before re-emerging in the ablation area. In contrast, low elevation source areas deposit debris close to or within the ablation area, where it spends little time entrained within the ice before melting out.

The model therefore suggests that the debris cover emerging in the present-day ablation zone of Zmuttgletscher is a mixture of particles with residence times spanning tens to several hundred years. The broad range of individual englacial times, reflecting the different particle transport paths depending on debris specific input location and entrainment depth further emphasizes this. This finding highlights the complexity of attempts to invert present-day debris cover for past erosion rates, which is an often relied-on estimate for the modelling of debris-covered glaciers (Heimsath and McGlynn, 2008; Banerjee and Wani, 2018; McCarthy et al., 2022).

5.4 Limitations

This Section presents some of the limitations of the field work, conducted on Zmuttgletscher and the of the modelling approach using the debrisIGM module.

5.4.1 Field Measurements

The field campaign provides a useful but spatially and temporally limited dataset, as sampling locations were constrained by safety considerations and proximity to camp, and the data, except for ablation measurements, represent a single point in time. The limited number of samples, constrains the robustness of the data, especially in the light of the sparse and irregular nature of the debris distribution.

The Core Sampling detection limit issue discussed in Section 5.2 implies that CS-reported zero values, especially in low concentration areas cannot be interpreted as true debris absence. This particularly affected the characterisation of flow unit 6, where most sampling was performed with CS. A more complete picture of concentrations in these units would require either more BS sampling or an improved CS workflow using more precise filter and weighing techniques.

In addition, in-situ measurements are affected by a similar stochasticity effect, like the one explained for the model grid cells, caused by the finite amount of particles (Section 5.3.2). Small-volume samples of a sparse and irregularly distributed debris field can produce substantial variability at fine spatial scales. This is evident both between co-located samples, as at site 4 (0.0160 (BS) vs 0 vol.% (CS)) and between nearby sites within a single flow unit, for example, sites 1 and 6 in flow unit 7 recorded 0.0119 and 0.0015 vol.% respectively, both using the BS method.

5.4.2 Modelling

The modelling framework is subject to several limitations. The experimental design, including the climatic forcing defined in Section 3.3.8, is intentionally simplified. While this setup is appropriate for investigating the model's general behaviour and capabilities, it limits the significance that can be attributed to specific small-scale outputs.

This study did not investigate the effects of variable debris input rates, an important characteristic of debris-covered glacier systems. Higher debris inputs would result in more debris being transported through the glacier system, likely affecting debris concentration and, in turn, glacier evolution (e.g. Anderson and Anderson, 2016; Ferguson and Vieli, 2021).

The 50 m grid resolution limits the ability of the model to capture small-scale differences and processes such as the debris-overlap zone between flow units 3, 4, and 5 (red hatched area in Figure 3.3). As most flow units, especially after the convergence in the study area, are less than 100 m wide, this limits the model's ability to reproduce fine-scale contrasts between adjacent flow units, particularly at their margins. The sampling-radius approach (Section 3.3.5), which aggregates particles within R meters of each site, partially addresses this by avoiding reliance on a single grid cell, but is similarly affected by the stochasticity of the individual particles. A higher-resolution simulation would allow these features to be resolved more sharply, at the cost of substantially increased computational demand.

A higher grid resolution would also address a further model limitation, since the number of seeded particles scales directly with the number of grid cells. The debrisIGM module's seeding scheme (Section 3.3.3) is applied to each individual cell within the seeding area mask and generates one particle per cell per time step, provided the seeding conditions are met. A higher grid resolution would therefore increase the total number of seeded particles and assign smaller debris volumes per particle, which could produce a more even and realistic distribution between cells and reduce the fragmented pattern discussed above.

5.5 Outlook

Building on the findings and limitations of this study, several directions for future research emerge.

On the field side, a hybrid BS–CS strategy, with a small number of BS anchor sites calibrating a denser network of CS sites shows a promising approach for future field studies on englacial debris concentrations. Realising this will require a more refined CS filtering approach.

On the modelling side, a larger-scale sensitivity study of the debrisIGM module is needed to demonstrate its capabilities in more detail. Building on this, future work could incorporate historically more accurate ELA time series (e.g., Lüthi, 2014) to better constrain the climatic forcing and more realistically model the glacier evolution, which would in turn enable more informed future projections.

The present study assumed a steady and spatially uniform debris input. Since debris input strongly affects glacier dynamics, future efforts should explore more realistic forcing, for example, a simple spatially and temporally variable debris input framework or stochastic seeding scheme (e.g., Leger et al., 2026).

Finally, the debrisIGM could be used to study the vertical distribution of debris within the ice column, especially, when combined with in-situ measurements, like the ones retrieved by Miles et al. (2021) through continuous borehole measurements. In this context, the sensitivity study of Hardmeier et al. (2025) will provide an important foundation for future work on debris-covered glacier systems using debrisIGM.

6. Conclusion

This thesis reported the first englacial debris concentrations for a Swiss glacier. In-situ measurements from Zmuttgletscher, collected with new sampling methodologies have been compared with modelling results of the debrisIGM module, under development by (Hardmeier et al., 2025). The following three research questions where answered in the process:

Research Question 1 – Englacial Debris Concentration: What are the englacial debris concentrations across the upper ablation zone of a debris-covered glacier, and how do these concentrations differ between flow units?

Measured englacial debris concentrations on Zmuttgletscher ranged from 0 to 0.0414 vol%, consistent with other temperate Alpine glaciers but well below values reported for high relief Himalayan settings. Concentrations varied systematically between flow units and covaried with supraglacial debris cover thickness and ablation rate, supporting the hypothesis that distinct catchment characteristics produce identifiable flow units in the ablation area.

Research question 2 - Methodological approach: What are the strengths, limitations, and uncertainties of the applied field measurement methodology and the incorporation of its results as a validation for numerical modelling of debris-covered glaciers?

Both Block Sampling (BS) and Core Sampling (CS) proved feasible alternatives to traditional melt-out experiments, enabling substantially greater spatial coverage within a single campaign. BS offered statistical robustness through larger sample volumes, while CS enabled higher sampling frequency at the cost of a detection-limit issue at low concentrations. A hybrid BS–CS strategy, using BS anchor sites to calibrate a denser CS network, is recommended for future campaigns.

Research question 3 - Modelling a Debris-Covered Glacier: To what extent does the Instructed Glacier Model (IGM) capture the spatial variability of the englacial debris concentration and debris cover patterns in comparison to real-world observations?

The debrisIGM module (Hardmeier et al., 2025) successfully reproduced the Little Ice Age maximum extent and, at the reference time steps representing the present-day geometry, produced englacial debris concentrations within the same order of magnitude as the field measurements. Modelled spatial patterns broadly matched the mapped flow units, with elevated concentrations coinciding with pronounced debris cover. Tracking particles by source area revealed coherent debris units preserved from headwall to ablation zone and a strong correlation between source area mean elevation and the englacial transport time. A dedicated sensitivity study is needed to further demonstrate the capabilities of the debrisIGM module for modelling debris-covered glaciers.

Bibliography

Anderson, L. S., Armstrong, W. H., Anderson, R. S., and Buri, P. 2021. "Debris cover and the thinning of Kennicott Glacier, Alaska: in situ measurements, automated ice cliff delineation and distributed melt estimates". *The Cryosphere* 15.1, pp. 265–282. doi: 10.5194/tc-15-265-2021.

Anderson, L. S. and Anderson, R. S. 2016. "Modeling debris-covered glaciers: response to steady debris deposition". *The Cryosphere* 10.3, pp. 1105–1124. doi: 10.5194/tc-10-1105-2016.

Anderson, L. S. and Anderson, R. S. 2018. "Debris thickness patterns on debris-covered glaciers". *Geomorphology* 311, pp. 1–12. doi: 10.1016/j.geomorph.2018.03.014.

Anderson, R. S. 2000. "A model of ablation-dominated medial moraines and the generation of debris-mantled glacier snouts". *Journal of Glaciology* 46.154, pp. 459–469. doi: 10.3189/172756500781833025.

Banerjee, A. and Shankar, R. 2013. "On the response of Himalayan glaciers to climate change". *Journal of Glaciology* 59.215, pp. 480–490. doi: 10.3189/2013JoG12J130.

Banerjee, A. and Wani, B. A. 2018. "Exponentially decreasing erosion rates protect the high-elevation crests of the Himalaya". *Earth and Planetary Science Letters* 497, pp. 22–28. doi: 10.1016/j.epsl.2018.06.001.

Bauder, A., Huss, M., and Linsbauer, A. 2024. *The Swiss Glaciers 2021/22 and 2022/23*. English. Tech. rep. GLAMOS - Glacier Monitoring Switzerland. doi: 0.18752/glrep˙143-144.

Benn, D. I., Bolch, T., Hands, K., Gulley, J., Luckman, A., Nicholson, L. I., Quincey, D., Thompson, S., Toumi, R., and Wiseman, S. 2012. "Response of debris-covered glaciers in the Mount Everest region to recent warming, and implications for outburst flood hazards". *Earth-Science Reviews* 114.1, pp. 156–174. doi: 10.1016/j.earscirev.2012.03.008.

Benn, D. I. and Owen, L. A. 2002. "Himalayan glacial sedimentary environments: a framework for reconstructing and dating the former extent of glaciers in high mountains". *Quaternary International* 97-98, pp. 3–25. doi: 10.1016/S1040-6182(02)00048-4.

Bernard, M., Steer, P., Gallagher, K., and Lundbek Egholm, D. 2020. "Modelling the effects of ice transport and sediment sources on the form of detrital thermochronological age probability distributions from glacial settings". *Earth Surface Dynamics* 8.4, pp. 931–953. doi: 10.5194/esurf-8-931-2020.

Bozhinskiy, A. N., Krass, M. S., and Popovnin, V. V. 1986. “Role of Debris Cover in the Thermal Physics of Glaciers”. *Journal of Glaciology* 32.111, pp. 255–266. doi: 10.3189/S0022143000015598.

Compagno, L., Huss, M., Miles, E. S., McCarthy, M. J., Zekollari, H., Dehecq, A., Pellicciotti, F., and Farinotti, D. 2022a. “Modelling supraglacial debris-cover evolution from the single-glacier to the regional scale: an application to High Mountain Asia”. *The Cryosphere* 16.5, pp. 1697–1718. doi: 10.5194/tc-16-1697-2022.

Compagno, L., Huss, M., Zekollari, H., Miles, E. S., and Farinotti, D. 2022b. “Future growth and decline of high mountain Asia’s ice-dammed lakes and associated risk”. *Communications Earth & Environment* 3.1, p. 191. doi: 10.1038/s43247-022-00520-8.

Deline, P. 2005. “Change in surface debris cover on Mont Blanc massif glaciers after the‘Little Ice Age’ termination”. *The Holocene* 15.2, pp. 302–309. doi: 10.1191/0959683605hl809rr.

Dowdeswell, J. A. 1986. “The Distribution and Character of Sediments in a Tidewater Glacier, Southern Baffin Island, N.W.T., Canada”. *Arctic and Alpine Research* 18.1, pp. 45–56. doi: 10.1080/00040851.1986.12004062.

Dussaillant, I., Hugonnet, R., Huss, M., Berthier, E., Bannwart, J., Paul, F., and Zemp, M. 2025. “Annual mass change of the world’s glaciers from 1976 to 2024 by temporal downscaling of satellite data with in situ observations”. *Earth System Science Data* 17.5, pp. 1977–2006. doi: 10.5194/essd-17-1977-2025.

Edwards, T. L., Nowicki, S., Marzeion, B., Hock, R., Goelzer, H., Seroussi, H., Jourdain, N. C., Slater, D. A., Turner, F. E., Smith, C. J., McKenna, C. M., Simon, E., Abe-Ouchi, A., Gregory, J. M., Larour, E., Lipscomb, W. H., Payne, A. J., Shepherd, A., Agosta, C., Alexander, P., Albrecht, T., Anderson, B., Asay-Davis, X., Aschwanden, A., Barthel, A., Bliss, A., Calov, R., Chambers, C., Champollion, N., Choi, Y., Cullather, R., Cuzzone, J., Dumas, C., Felikson, D., Fettweis, X., Fujita, K., Galton-Fenzi, B. K., Gladstone, R., Golledge, N. R., Greve, R., Hattermann, T., Hoffman, M. J., Humbert, A., Huss, M., Huybrechts, P., Immerzeel, W., Kleiner, T., Kraaijenbrink, P., Le clec’h, S., Lee, V., Leguy, G. R., Little, C. M., Lowry, D. P., Malles, J.-H., Martin, D. F., Maussion, F., Morlighem, M., O’Neill, J. F., Nias, I., Pattyn, F., Pelle, T., Price, S. F., Quiquet, A., Radić, V., Reese, R., Rounce, D. R., Rückamp, M., Sakai, A., Shafer, C., Schlegel, N.-J., Shannon, S., Smith, R. S., Straneo, F., Sun, S., Tarasov, L., Trusel, L. D., Van Breedam, J., Wal, R. van de, Broeke, M. van den, Winkelmann, R., Zekollari, H., Zhao, C., Zhang, T., and Zwinger, T. 2021. “Projected land ice contributions to twenty-first-century sea level rise". *Nature* 593.7857, pp. 74–82. doi: 10.1038/s41586-021-03302-y.

Egholm, D. L., Knudsen, M. F., Clark, C. D., and Lesemann, J. E. 2011. "Modeling the flow of glaciers in steep terrains: The integrated second-order shallow ice approximation (iSOSIA)". *Journal of Geophysical Research: Earth Surface* 116.F2. doi: 10.1029/2010JF001900.

Evatt, G. W., Abrahams, I. D., Heil, M., Mayer, C., Kingslake, J., Mitchell, S. L., Fowler, A. C., and Clark, C. D. 2015. "Glacial melt under a porous debris layer". *Journal of Glaciology* 61.229, pp. 825–836. doi: 10.3189/2015JoG14J235.

Ferguson, J. C. and Vieli, A. 2021. "Modelling steady states and the transient response of debris-covered glaciers". *The Cryosphere* 15.7, pp. 3377–3399. doi: 10.5194/tc-15-3377-2021.

Ferguson, J. C. 2022. "Modelling the dynamics and evolution of debris-covered glaciers". PhD thesis. University of Zurich. doi: 10.5167/UZH-228173.

Fleischer, F., Otto, J.-C., Junker, R. R., and Hölbling, D. 2021. "Evolution of debris cover on glaciers of the Eastern Alps, Austria, between 1996 and 2015". *Earth Surface Processes and Landforms* 46.9, pp. 1673–1691. doi: 10.1002/esp.5065.

Ganarin, R. 2019. "Where does it come from, where does it go? An Integral Assessment of the Supraglacial Debris Cover of Zmuttgletscher, Swiss Alps". PhD thesis. University of Zurich.

Gibson, M. J., Glasser, N. F., Quincey, D. J., Mayer, C., Rowan, A. V., and Irvine-Fynn, T. D. L. 2017. "Temporal variations in supraglacial debris distribution on Baltoro Glacier, Karakoram between 2001 and 2012". *Geomorphology* 295, pp. 572–585. doi: 10.1016/j.geomorph.2017.08.012.

GLAMOS 2024. *The Swiss Glaciers 1880–2022/23*. Issue: 1–142 Series: Glaciological Reports. doi: 10.18752/glrep˙series.

Glen, J. W. 1955. "The creep of polycrystalline ice". *Proceedings of the Royal Society of London. A. Mathematical and Physical Sciences* 228.1175, pp. 519–538. doi: 10.1098/rspa.1955.0066.

Gruber, S., Fleiner, R., Guegan, E., Panday, P., Schmid, M.-O., Stumm, D., Wester, P., Zhang, Y., and Zhao, L. 2017. "Review article: Inferring permafrost and permafrost thaw in the mountains of the Hindu Kush Himalaya region". *The Cryosphere* 11.1, pp. 81–99. doi: 10.5194/tc-11-81-2017.

Gudmundsson, G. H. 1999. "A three-dimensional numerical model of the confluence area of Unteraargletscher, Bernese Alps, Switzerland". *Journal of Glaciology* 45.150, pp. 219–230. doi: 10.3189/002214399793377086.

Hambrey, M. J., Quincey, D. J., Glasser, N. F., Reynolds, J. M., Richardson, S. J., and Clemmens, S. 2008. "Sedimentological, geomorphological and dynamic context of debris-mantled glaciers, Mount Everest (Sagarmatha) region, Nepal". *Quaternary Science Reviews* 27.25, pp. 2361–2389. doi: 10.1016/j.quascirev.2008.08.010.

Hardmeier, F., Ferguson, J. C., and Vieli, A. 2026. "Modelling debris-covered glacier dynamics: transient response to changes and feedbacks in debris and climate forcing". *EGUsphere* 2026, pp. 1–43. doi: 10.5194/egusphere-2025-5997.

Hardmeier, F., Muñoz-Hermosilla, J. M., Miles, E., Jouvet, G., and Vieli, A. 2025. "Exploiting Lagrangian particle tracking in the Instructed Glacier Model (IGM) to model coupled debris-covered glacier dynamics". *EGU General Assembly 2025*. Vienna, Austria. doi: 10.5194/egusphere-egu25-6707.

Heimsath, A. M. and McGlynn, R. 2008. "Quantifying periglacial erosion in the Nepal high Himalaya". *Geomorphology* 97.1, pp. 5–23. doi: 10.1016/j.geomorph.2007.02.046.

Henz, A., Reinthaler, J., Nussbaumer, S. U., Leger, T. P. M., Kamleitner, S., Jouvet, G., and Vieli, A. 2025. "Alps-wide high-resolution 3D modelling reconstruction of glacier geometry and climatic conditions for the Little Ice Age". *The Cryosphere* 19.11, pp. 5913–5937. doi: 10.5194/tc-19-5913-2025.

Herreid, S. and Pellicciotti, F. 2020. "The state of rock debris covering Earth's glaciers". *Nature Geoscience* 13.9, pp. 621–627. doi: 10.1038/s41561-020-0615-0.

Howe, C. and Boyer, D. 2024. "The Okjökull Memorial and Geohuman Relations". *Social Anthropology/Anthropologie Sociale* 32.1, pp. 30–45. doi: 10.3167/saas.2024.320104.

Howe, C. and Boyer, D. 2025. "Social impacts of glacier loss". *Science* 388.6750, pp. 914–915. doi: 10.1126/science.ady1688.

Huss, M., Bauder, A., Linsbauer, A., and Barandun, M. 2025a. *Annual mass balance of Swiss glaciers in 2024/2025*. en. Tech. rep. GLAMOS - Glacier Monitoring Switzerland. (Visited on 11/11/2025).

Huss, M., Fischer, M., Linsbauer, A., and Bauder, A. 2025b. "Continuous monitoring of a glacier's extinction". *Annals of Glaciology* 66, e27. doi: 10.1017/aog.2025.10024.

Huss, M. and Hock, R. 2018. "Global-scale hydrological response to future glacier mass loss". *Nature Climate Change* 8.2, pp. 135–140. doi: 10.1038/s41558-017-0049-x.

IPCC 2023. *Climate Change 2023: Synthesis Report*. en. Tech. rep. IPCC, Geneva, Switzerland: Contribution of Working Groups I, II, III to the Sixth Assessment Report of the Intergovernmental Panel on Climate Change [Core Writing Team, H. Lee, and J. Romero (eds.)]

Jennings, S. J., Hambrey, M. J., and Glasser, N. F. 2014. "Ice flow-unit influence on glacier structure, debris entrainment and transport". *Earth Surface Processes and Landforms* 39.10, pp. 1279–1292. doi: 10.1002/esp.3521.

Jouvet, G., Cook, S., Cordonnier, G., Finley, B., Henz, A., Hermann, O., Maussion, F., Mey, J., Scherler, D., and Welty, E. 2024. *Concepts and capabilities of the Instructed Glacier Model (IGM v2.2.1)*. doi: 10.31223/X5T99C. (Visited on 06/11/2025).

Jouvet, G. and Cordonnier, G. 2023. "Ice-flow model emulator based on physics-informed deep learning". en. *Journal of Glaciology* 69.278, pp. 1941–1955. doi: 10.1017/jog.2023.73.

Jouvet, G., Cordonnier, G., Kim, B., Lüthi, M., Vieli, A., and Aschwanden, A. 2022. "Deep learning speeds up ice flow modelling by several orders of magnitude". *Journal of Glaciology* 68.270, pp. 651–664. doi: 10.1017/jog.2021.120.

Kirkbride, M. P. 2011. "Debris-Covered Glaciers". *Encyclopedia of Snow, Ice and Glaciers*. Ed. by V. P. Singh, P. Singh, and U. K. Haritashya. Dordrecht: Springer Netherlands, pp. 180–182. doi: 10.1007/978-90-481-2642-2˙622.

Kirkbride, M. P. and Deline, P. 2013. "The formation of supraglacial debris covers by primary dispersal from transverse englacial debris bands". *Earth Surface Processes and Landforms* 38.15, pp. 1779–1792. doi: 10.1002/esp.3416.

Kneib, M., Fyffe, C. L., Miles, E. S., Lindemann, S., Shaw, T. E., Buri, P., McCarthy, M., Ouvry, B., Vieli, A., Sato, Y., Kraaijenbrink, P. D. A., Zhao, C., Molnar, P., and Pellicciotti, F. 2023. "Controls on Ice Cliff Distribution and Characteristics on Debris-Covered Glaciers". *Geophysical Research Letters* 50.6, e2022GL102444. doi: 10.1029/2022GL102444.

Kneib, M., Maussion, F., Brun, F., Carcanade, G., Farinotti, D., Huss, M., Tiel, M. van, Jouberton, A., Schmitt, P., Schuster, L., Dehecq, A., and Champollion, N. 2025. "Topographically-controlled contribution of avalanches to glacier mass balance in the 21st century". *Nature Communications* 16.1, p. 10122. doi: 10.1038/s41467-025-65608-z.

Leger, T. P. M., Jouvet, G., Kamleitner, S., Finley, B. D., Bernard, M., Allegri, B., Herman, F., Vieli, A., Henz, A., and Nussbaumer, S. U. 2026. "First Alps-wide reconstruction of LGM glacial sediment transport enabled by GPU-accelerated particle tracking". *EGUsphere* 2026, pp. 1–49. doi: 10.5194/egusphere-2026-503.

Leger, T. P. M., Jouvet, G., Kamleitner, S., Mey, J., Herman, F., Finley, B. D., Ivy-Ochs, S., Vieli, A., Henz, A., and Nussbaumer, S. U. 2025. "A data-consistent model of the last glaciation in the Alps achieved with physics-driven AI". *Nature Communications* 16.1, p. 848. doi: 10.1038/s41467-025-56168-3.

Linsbauer, A., Huss, M., Hodel, E., Bauder, A., Fischer, M., Weidmann, Y., Bärtschi, H., and Schmassmann, E. 2021. "The New Swiss Glacier Inventory SGI2016: From a Topographical to a Glaciological Dataset". en. *Frontiers in Earth Science* 9. doi: 10.3389/feart.2021.704189.

Lüthi, M. P. 2014. "Little Ice Age climate reconstruction from ensemble reanalysis of Alpine glacier fluctuations". *The Cryosphere* 8.2, pp. 639–650. doi: 10.5194/tc-8-639-2014.

Margirier, A., Brondex, J., Rowan, A. V., Schmidt, C., Pedersen, V. K., Lehmann, B., Anderson, L. S., Veness, R., Watson, C. S., Swift, D., and King, G. E. 2025. "Tracking Sediment Transport Through Miage Glacier, Italy, Using a Lagrangian Approach With Luminescence Rock Surface Burial Dating of Englacial Clasts". *Journal of Geophysical Research: Earth Surface* 130.3, e2024JF007773. doi: 10.1029/2024JF007773.

Mattson, L. E., Gardner, J. S., and Young, G. J. 1993. "Ablation on Debris Covered Glaciers: an Example from the Rakhiot Glacier, Punjab, Himalaya". *Snow and Glacier Hydrology*. Vol. 218. IAHS Publication, pp. 289–296.

Maussion, F., Butenko, A., Champollion, N., Dusch, M., Eis, J., Fourteau, K., Gregor, P., Jarosch, A. H., Landmann, J., Oesterle, F., Recinos, B., Rothenpieler, T., Vlug, A., Wild, C. T., and Marzeion, B. 2019. "The Open Global Glacier Model (OGGM) v1.1". *Geoscientific Model Development* 12.3, pp. 909–931. doi: 10.5194/gmd-12-909-2019.

Mayer, C. and Licciulli, C. 2021. "The Concept of Steady State, Cyclicity and Debris Unloading of Debris-Covered Glaciers". *Frontiers in Earth Science* Volume 9 - 2021. doi: 10.3389/feart.2021.710276.

McCarthy, M., Miles, E., Kneib, M., Buri, P., Fugger, S., and Pellicciotti, F. 2022. "Supraglacial debris thickness and supply rate in High-Mountain Asia". *Communications Earth & Environment* 3.1, p. 269. doi: 10.1038/s43247-022-00588-2.

Meier, L. 2026a. *Ice thickness evolution of Zmuttgletscher using the debrisIGM module*. [Video]. URL: `https://uzh.mediaspace.cast.switch.ch/media/Ice+thickness+evolution+of+Zmuttgletscher+using+the+debrisIGM+module/0_fliybzcf`.

Meier, L. 2026b. *Supraglacial debris evolution on Zmuttgletscher using the debrisIGM module*. [Video]. URL: `https://uzh.mediaspace.cast.switch.ch/media/Supraglacial+debris+evolution+on+Zmuttgletscher+using+the+debrisIGM+module/0_9c807rhe`.

Meier, L. 2026c. *Vertical debris distribution of ten profiles across Zmuttgletscher using the debrisIGM module*. [Video]. URL: `https://uzh.mediaspace.cast.`

switch.ch/media/Vertical+debris+distribution+of+ten+profiles+ +across+Zmuttgletscher+using+the+debrisIGM+module/0_sl2fb2gr.

Meier, L. 2026d. *Zmuttgletscher Melt-Out Experiment 2025*. [Video]. URL: https://uzh.mediaspace.cast.switch.ch/media/Zmuttgletscher+Melt-Out+Experiment+2025/0_64fjfut8.

Miles, K. E., Hubbard, B., Miles, E. S., Quincey, D. J., Rowan, A. V., Kirkbride, M., and Hornsey, J. 2021. "Continuous borehole optical televiewing reveals variable englacial debris concentrations at Khumbu Glacier, Nepal". *Communications Earth & Environment* 2.1, p. 12. doi: 10.1038/s43247-020-00070-x.

Mölg, N., Bolch, T., Walter, A., and Vieli, A. 2019. "Unravelling the evolution of Zmuttgletscher and its debris cover since the end of the Little Ice Age". *The Cryosphere* 13.7, pp. 1889–1909. doi: 10.5194/tc-13-1889-2019.

Mölg, N., Ferguson, J., Bolch, T., and Vieli, A. 2020. "On the influence of debris cover on glacier morphology: How high-relief structures evolve from smooth surfaces". *Geomorphology* 357, p. 107092. doi: 10.1016/j.geomorph.2020.107092.

Nicholson, L. and Benn, D. I. 2006. "Calculating ice melt beneath a debris layer using meteorological data". English. *Journal of Glaciology* 52, pp. 463–470. doi: 10.3189/172756506781828584.

Nicolussi, K., Roy, M. L., Schlüchter, C., Stoffel, M., and Wacker, L. 2022. "The glacier advance at the onset of the Little Ice Age in the Alps: New evidence from Mont Miné and Morteratsch glaciers". *The Holocene* 32.7, pp. 624–638. doi: 10.1177/09596836221088247.

Östrem, G. 1959. "Ice Melting under a Thin Layer of Moraine, and the Existence of Ice Cores in Moraine Ridges". *Geografiska Annaler* 41.4, pp. 228–230. doi: 10.1080/20014422.1959.11907953.

Pellicciotti, F., Stephan, C., Miles, E., Herreid, S., Immerzeel, W. W., and Bolch, T. 2015. "Mass-balance changes of the debris-covered glaciers in the Langtang Himal, Nepal, from 1974 to 1999". *Journal of Glaciology* 61.226. Edition: 2017/07/10, pp. 373–386. doi: 10.3189/2015JoG13J237.

QGIS Development Team 2026. *QGIS Geographic Information System*. QGIS Association. URL: https://www.qgis.org.

Racoviteanu, A. E., Nicholson, L., Glasser, N. F., Miles, E., Harrison, S., and Reynolds, J. M. 2022. "Debris-covered glacier systems and associated glacial lake outburst flood hazards: challenges and prospects". *Journal of the Geological Society* 179.3, jgs2021–084. doi: 10.1144/jgs2021-084.

Rounce, D. R., Hock, R., and Shean, D. E. 2020. "Glacier Mass Change in High Mountain Asia Through 2100 Using the Open-Source Python Glacier Evolution Model (PyGEM)". *Frontiers in Earth Science* Volume 7 - 2019. doi: 10.3389/feart.2019.00331.

Rowan, A. V., Egholm, D. L., Quincey, D. J., and Glasser, N. F. 2015. "Modelling the feedbacks between mass balance, ice flow and debris transport to predict the response to climate change of debris-covered glaciers in the Himalaya". *Earth and Planetary Science Letters* 430, pp. 427–438. doi: 10.1016/j.epsl.2015.09.004.

Scherler, D. and Egholm, D. L. 2020. "Production and Transport of Supraglacial Debris: Insights From Cosmogenic 10Be and Numerical Modeling, Chhota Shigri Glacier, Indian Himalaya". *Journal of Geophysical Research: Earth Surface* 125.10, e2020JF005586. doi: 10.1029/2020JF005586.

Scherler, D., Bookhagen, B., and Strecker, M. R. 2011. "Hillslope-glacier coupling: The interplay of topography and glacial dynamics in High Asia". *Journal of Geophysical Research: Earth Surface* 116.F2. doi: 10.1029/2010JF001751.

Scherler, D., Wulf, H., and Gorelick, N. 2018. "Global Assessment of Supraglacial Debris-Cover Extents". *Geophysical Research Letters* 45.21, pp. 11, 798–11, 805. doi: 10.1029/2018GL080158.

Slangen, A. B., Palmer, M. D., Camargo, C. M., Church, J. A., Edwards, T. L., Hermans, T. H., Hewitt, H. T., Garner, G. G., Gregory, J. M., Kopp, R. E., et al. 2023. "The evolution of 21st century sea-level projections from IPCC AR5 to AR6 and beyond". *Cambridge Prisms: Coastal Futures* 1, e7. doi: 10.1017/cft.2022.8.

Swisstopo 2023. *SWISSIMAGE*. Das digitale Farborthofotomosaik der Schweiz. URL: `https://www.swisstopo.admin.ch/de/orthobilder-swissimage-10-cm`.

Swisstopo 2024a. *Geologischer Atlas der Schweiz*. URL: `https://www.swisstopo.admin.ch/de/geologischer-atlas-der-schweiz-1-25000-pixel`.

Swisstopo 2024b. *SWISSALTI3D*. Das hochpräzise digitale Höhenmodell der Schweiz. URL: `https://www.swisstopo.admin.ch/de/hoehenmodell-swissalti3d`.

Swisstopo 2026. *Zeitreisen*. Zeitreisen mit Karten und Luftbildern. URL: `https://www.swisstopo.admin.ch/de/zeitreise-kartenwerke`.

Van Tricht, L., Zekollari, H., Huss, M., Rounce, D. R., Schuster, L., Aguayo, R., Schmitt, P., Maussion, F., Tober, B., and Farinotti, D. 2026. "Peak glacier extinction in the mid-twenty-first century". *Nature Climate Change* 16.2, pp. 143–147. doi: 10.1038/s41558-025-02513-9.

Verhaegen, Y., Huybrechts, P., Rybak, O., and Popovnin, V. V. 2020. "Modelling the evolution of Djankuat Glacier, North Caucasus, from 1752 until 2100CE". *The Cryosphere* 14.11, pp. 4039–4061. doi: 10.5194/tc-14-4039-2020.

Wirbel, A., Jarosch, A. H., and Nicholson, L. 2018. “Modelling debris transport within glaciers by advection in a full-Stokes ice flow model”. *The Cryosphere* 12.1, pp. 189–204. doi: 10.5194/tc-12-189-2018.

Woerkom, T. van, Steiner, J. F., Kraaijenbrink, P. D. A., Miles, E. S., and Immerzeel, W. W. 2019. “Sediment supply from lateral moraines to a debris-covered glacier in the Himalaya”. *Earth Surface Dynamics* 7.2, pp. 411–427. doi: 10.5194/esurf-7-411-2019.

Zanoni, M. G., Stella, E., and Bellin, A. 2023. “Long-term hydrological behavior of an Alpine glacier”. *Journal of Hydrology* 626, p. 130316. doi: 10.1016/j.jhydrol.2023.130316.

Zekollari, H., Huss, M., and Farinotti, D. 2019. “Modelling the future evolution of glaciers in the European Alps under the EURO-CORDEX RCM ensemble”. *The Cryosphere* 13.4, pp. 1125–1146. doi: 10.5194/tc-13-1125-2019.

Zekollari, H., Huss, M., Schuster, L., Maussion, F., Rounce, D. R., Aguayo, R., Champollion, N., Compagno, L., Hugonnet, R., Marzeion, B., Mojtabavi, S., and Farinotti, D. 2024. “Twenty-first century global glacier evolution under CMIP6 scenarios and the role of glacier-specific observations”. *The Cryosphere* 18.11, pp. 5045–5066. doi: 10.5194/tc-18-5045-2024.

Zemp, M., Huss, M., Eckert, N., Thibert, E., Paul, F., Nussbaumer, S. U., and Gärtner-Roer, I. 2020. “Brief communication: Ad hoc estimation of glacier contributions to sea-level rise from the latest glaciological observations”. *The Cryosphere* 14.3, pp. 1043–1050. doi: 10.5194/tc-14-1043-2020.

Appendix A - Additional Figures

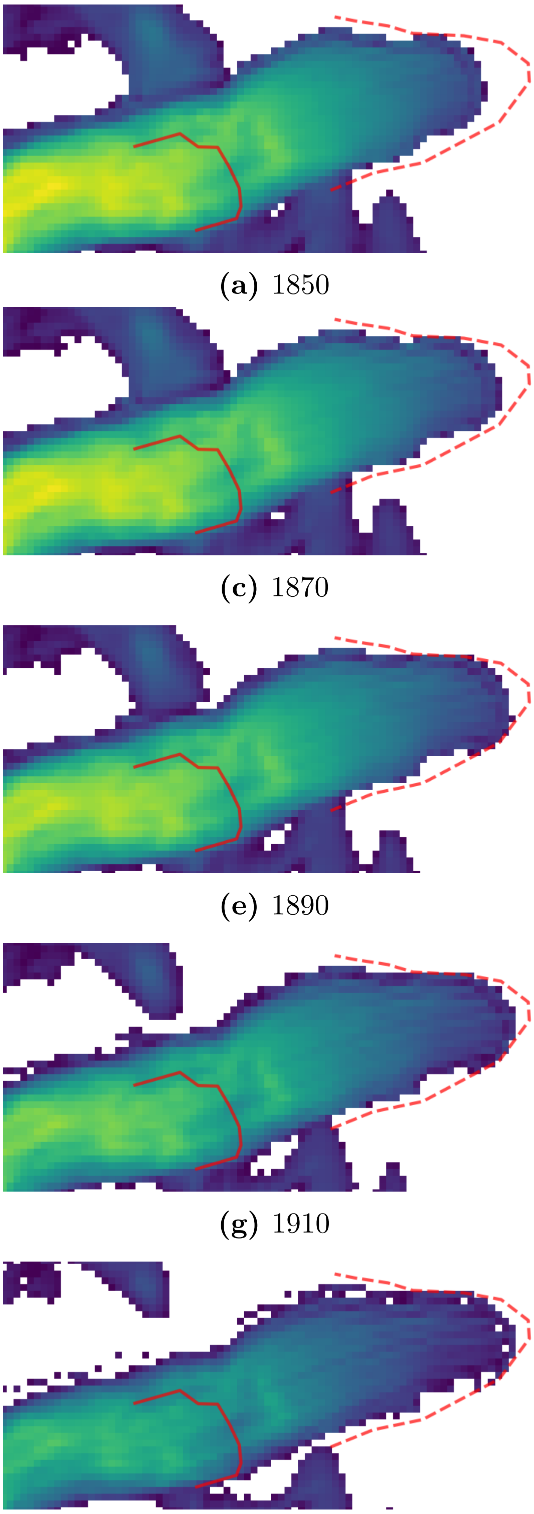

(a) 1850

(b) 1860

(c) 1870

(d) 1880

(e) 1890

(f) 1900

(g) 1910

(h) 1920

(i) 1930

(j) 1940

Figure A.1: Modelled ice thickness, illustrating the glacier extent from 1850 to 1940. The solid red line marks the present-day glacier boundary; the dashed red line indicates the location of the Little Ice Age terminal moraines.

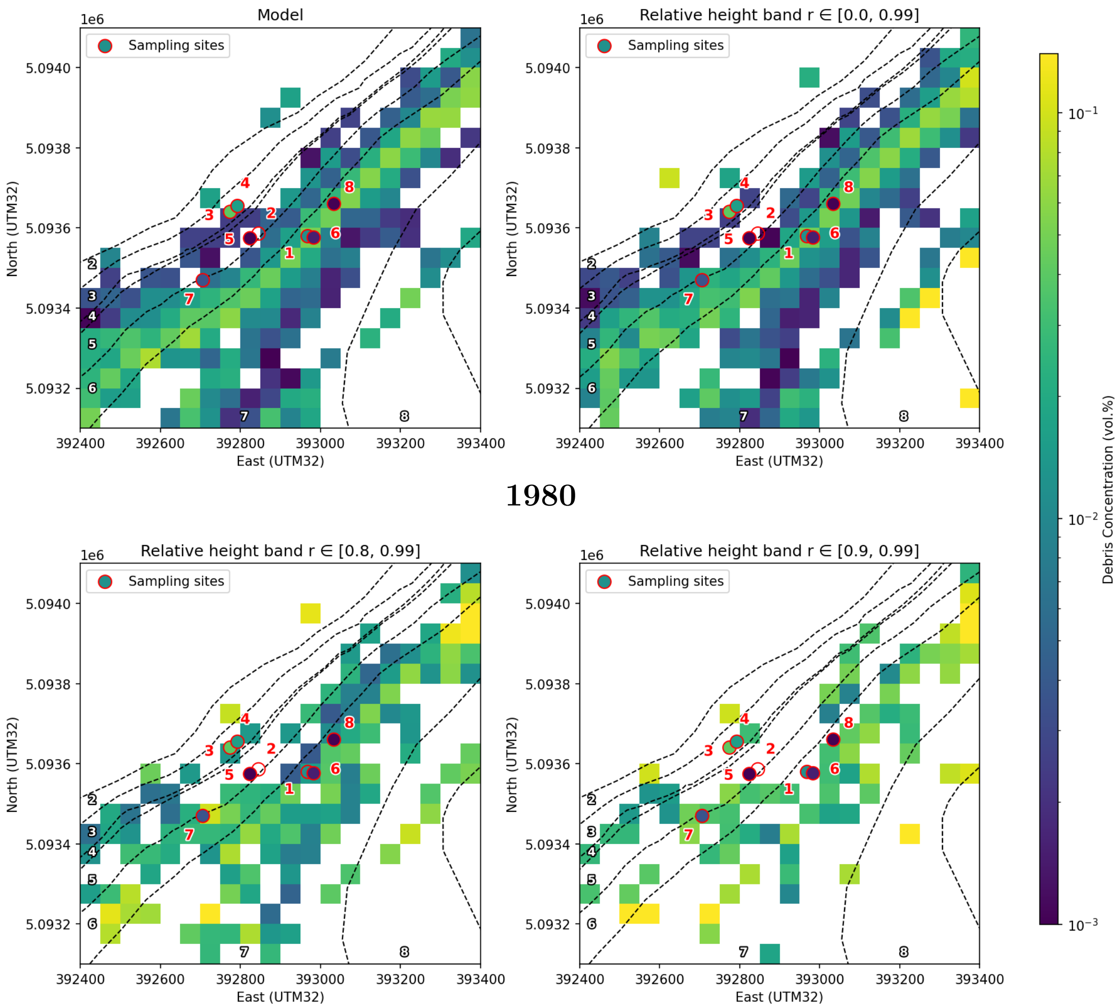

Figure A.2: Modelled debris concentration (vol.%) of time step 1980, shown for the full ice columns (model output, top left) and three relative height bands (r∈ $[0, 0.99]$, $[0.8, 0.99]$, $[0.9, 0.99]$. Dashed lines indicate the flow unit (white numbers) boundaries. Colored circles show the measured debris concentrations at sampling sites (red numbers). The color scale is logarithmic.

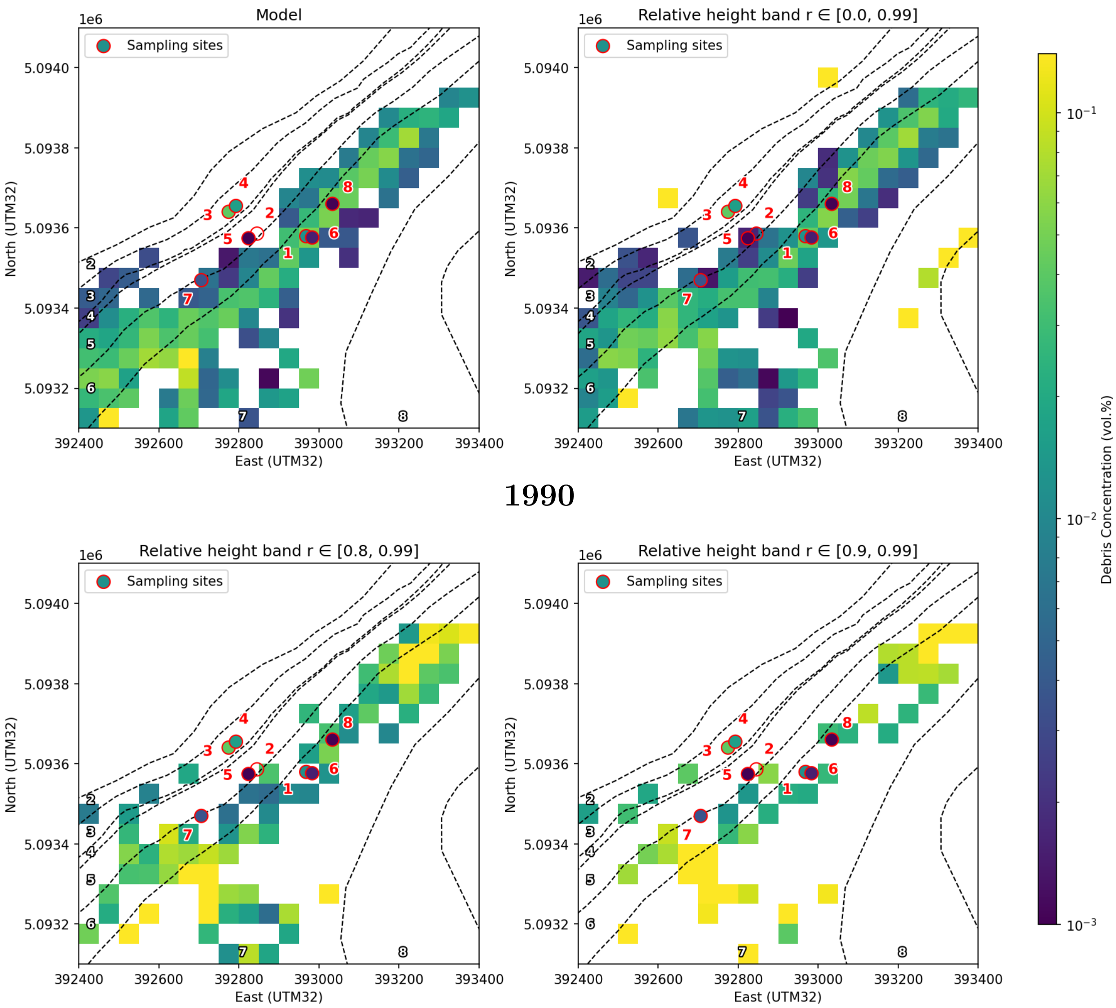

Figure A.3: Modelled debris concentration (vol.%) of time step 1990, shown for the full ice columns (model output, top left) and three relative height bands (r∈ $[0, 0.99], [0.8, 0.99], [0.9, 0.99]$. Dashed lines indicate the flow unit (white numbers) boundaries. Colored circles show the measured debris concentrations at sampling sites (red numbers). The color scale is logarithmic.

Appendix B - Additional Tables

Table B.1: Debris cover thickness by site and flow unit with coordinates in CH1903+/LV95, including individual measurements (1,2,3 and 4) as well as an average for each site.

		Coordinates LV95		Debris Cover Thickness [cm]				
Site	**Flow unit**	**East**	**North**	**1**	**2**	**3**	**4**	**avg.**
3	3	2613707	1092947	9.0	11.0	9.0		9.7
4	3	2613725	1092962	7.5	5.3	8.8		7.2
DT9	3	2613766	1092924	6.4	6.9	12.8		8.7
DT10	3	2613760	1092928	6.0	8.0	9.0		7.7
DT11	3	2613750	1092931	7.1	8.3	11.0		8.8
DT12	3	2613745	1092935	14.0	15.0	8.0		12.3
DT13	3	2613725	1092941	7.4	8.1	8.3		7.9
DT14	3	2613722	1092952	7.5	7.5	7.0		7.3
DT15	3	2613707	1092960	5.0	6.1	6.3		5.8
DT16	3	2613700	1092974	7.0	8.0	9.5		8.2
DT17	3	2613711	1092958	4.0	6.0	6.5		5.5
DT18	3	2613725	1092935	5.5	6.0	6.5		6.0
DT19	3	2613732	1092920	4.5	4.5	9.0		6.0
2	5	2613779	1092894	0.0	0.0	0.0		patchy
5	5	2613758	1092882	0.0	0.0	0.0		patchy
DT7	5	2613792	1092907	0.0	0.0	0.0		patchy
DT8	5	2613766	1092912	0.0	0.0	0.0		patchy
DT20	5	2613742	1092911	0.0	0.0	0.0		0.0
DT21	5	2613772	1092890	0.0	0.0	0.0		patchy
7	6	2613642	1092775	4.3	1.9	3.6		3.3
9	6	2613571	1092726					
10	6	2613715	1092796					
14	6	2613601	1092738					
DT2	6	2613865	1092898	10.5	10.1	8.5	7.8	9.2
DT3	6	2613849	1092901	7.0	4.0	5.5		5.5
DT4	6	2613827	1092899	4.1	4.7	5.8		4.9
DT5	6	2613814	1092903	6.0	4.0	2.5		4.2
DT6	6	2613800	1092898	4.6	5.0	6.1		5.2
DT22	6	2613785	1092877	4.5	5.0	3.5		4.3
DT23	6	2613814	1092873	4.5	7.0	9.0		6.8
DT24	6	2613844	1092872	7.0	9.0	12.0		9.3
1	7	2613902	1092890	17.0	16.0	16.0		16.3
6	7	2613917	1092887	16.8	13.5	16.9		15.7
8	7	2613966	1092972	12.9	11.3	9.9		11.4
11	7	2613926	1092859					
12	7	2613778	1092749					27.7
13	7	2613664	1092685					11.7
DT1	7	2613886	1092894	11.8	9.8	8.9		10.2
DT25	7	2613877	1092862	12.0	12.0	13.0		12.3
DT26	7	2613904	1092876	15.5	11.5	21.0		16.0

Note: "Patchy" indicates a non-continuous debris cover (approximately 60% surface area coverage).

Table B.2: Modelled englacial debris concentration (vol.%) at smapling sites 1–8 for reference time steps 1970, 1980, and 1990, shown for three relative height bands within a 25 m search radius: the full ice column ($r \in [0, 0.99]$), the top 20 % ($r \in [0.8, 0.99]$), and the uppermost 10 % ($r \in [0.9, 0.99]$). Values > 0 shown in bold.

			Debris concentration (vol.%)		
Flow Unit	**Site**	**Time step**	$\mathbf{r \in [0, 0.99]}$	$\mathbf{r \in [0.8, 0.99]}$	$\mathbf{r \in [0.9, 0.99]}$
3	3	1970	0.000	0.000	0.000
		1980	0.000	0.000	0.000
		1990	0.000	0.000	0.000
	4	1970	0.000	0.000	0.000
		1980	0.000	0.000	0.000
		1990	0.000	0.000	0.000
5	2	1970	**0.005**	0.000	0.000
		1980	0.000	0.000	0.000
		1990	0.000	0.000	0.000
	5	1970	**0.002**	0.000	0.000
		1980	0.000	0.000	0.000
		1990	0.000	0.000	0.000
6	7	1970	**0.001**	**0.001**	**0.001**
		1980	**0.012**	**0.011**	**0.004**
		1990	0.000	0.000	0.000
7	1	1970	**0.042**	**0.006**	**0.004**
		1980	**0.049**	**0.014**	**0.006**
		1990	**0.056**	**0.003**	0.000
	6	1970	**0.050**	**0.004**	**0.004**
		1980	**0.040**	**0.012**	**0.006**
		1990	**0.038**	**0.002**	0.000
	8	1970	**0.031**	**0.004**	0.000
		1980	**0.044**	**0.002**	**0.002**
		1990	**0.051**	**0.002**	**0.002**

Appendix C - Personal declaration

I hereby declare that the submitted thesis is the result of my own, independent work. All external sources are explicitly acknowledged in the thesis.

I further acknowledged the use of Claude for assistance in coding for data processing and visualization. Additionally, Claude and Writefull were used to to assist with the refinement of own formulations, grammar and syntax.

Zürich, 24.04.2026

Leano Meier